UCRL-52534

DROPLET PHASE CHARACTERISTICS IN LIQUID-DOMINATED STEAM-WATER NOZZLE FLOW

Terry Willis Alger
(Ph.D. Thesis)

August 9, 1978

Work performed under the auspices of the U.S. Department of Energy by the UCLLL under contract number W-7405-ENG-48

LAWRENCE
LIVERMORE
LABORATORY
University of California / Livermore

LAWRENCE LIVERMORE LABORATORY
University of California Livermore, California 94550

UCRL-52534

DROPLET PHASE CHARACTERISTICS IN LIQUID-DOMINATED STEAM-WATER NOZZLE FLOW

Terry Willis Alger
(Ph.D. Thesis)

MS. date: August 9, 1978

Droplet Phase Characteristics in Liquid-Dominated Steam-Water Nozzle Flow

By

TERRY WILLIS ALGER
B.S. (University of Utah) 1971
M.S. (University of Utah) 1972

DISSERTATION

Submitted in partial satisfaction of the requirements for the degree of

DOCTOR OF PHILOSOPHY

in

Engineering

in the

GRADUATE DIVISION

of the

UNIVERSITY OF CALIFORNIA

DAVIS

Approved:

Warren H. Dietz

Clyde D. Cowan

Morgan G. Hoffman

Committee in Charge

Deposited in the University Library.....
Date *Librarian*

ABSTRACT

An experimental study was undertaken to determine the droplet size distribution, the droplet spatial distribution and the mean droplet velocity in low-quality, steam-water flow from a rectangular cross-section, converging-diverging nozzle. A unique forward light scattering technique was developed for droplet size distribution measurements. Droplet spatial variations were investigated using light transmission measurements, and droplet velocities were measured with a laser-Doppler velocimeter (LDV) system incorporating a confocal Fabry-Perot interferometer. Nozzle throat radius of curvature and height were varied to investigate their effects on droplet size.

Droplet size distribution measurements yielded a nominal Sauter mean droplet diameter of 1.7 μm and a nominal mass-mean droplet diameter of 2.4 μm. Neither the throat radius of curvature nor the throat height were found to have a significant effect upon the nozzle exit droplet size. The light transmission and LDV measurement results confirmed both the droplet size measurements and demonstrated high spatial uniformity of the droplet phase within the nozzle jet flow. One-dimensional numerical calculations indicated that both the dynamic breakup (thermal equilibrium based on a critical Weber number of 6.0) and the boiling breakup (thermal nonequilibrium based on average droplet temperature) models predicted droplet diameters on the order of 7.5 μm which are approximately equal to the maximum stable droplet diameters within the nozzle jet flow.

TABLE OF CONTENTS

ACKNOWLEDGEMENTS

I take this opportunity to extend my sincere appreciation to the many people that have helped to make this work possible. I extend my gratitude to L. K. Isaacson who, during my undergraduate studies and as my M. S. thesis advisor at the University of Utah, instilled in me a desire to achieve this goal. I thank H. Brandt, who gave me the help and guidance necessary to overcome the system problems (both at LLL and U. C. Davis) and to get the process started towards the completion of this work. Special thanks are extended to my thesis advisors: W. H. Giedt, M. A. Hoffman and C. T. Crowe. Their help, guidance and support has definitely been invaluable in accomplishing this work.

My appreciation is extended to my past and present supervisors at LLL: E. R. McClure, S. J. Ekstrom, J. G. Rittmann, W. S. Neef, T. Perlman, A. L. Austin and A. W. Lundberg. Their direction and support was not in vain. Special thanks are extended to A. L. Austin and A. W. Lundberg for their leadership of the geothermal energy conversion effort and for their personal assistance towards the completion of this work. C. C. Gardiner designed the two-phase nozzle test apparatus. His design creativity and insight helped to overcome many technical difficulties and possible time delays. The many fruitful discussions and helpful suggestions of W. J. Comfort were of great assistance. H. Weiss provided a great amount of technical support and consultation over the many months of experimentation. R. T. Hasbrouck, N. L. Rector and W. F. Gee gave assistance in designing and

understanding the instrumentation and recording equipment. The efforts of G. H. Lathrop, L. L. Jackson, C. W. Hall and D. W. Hansen concerning the operation and maintenance of the experimental system were greatly appreciated. Many thanks are extended to D. L. Podesta for his perserverance in the assembly - test - disassembly - modify - reassembly iteration process that was necessary to determine the final experimental arrangement for the droplet characteristics measurements. A. A. Andersen competently coordinated the purchase and fabrication of the test equipment. W.. W. Wilcox gave a great amount of help concerning the different optical arrangements and the shadowgraph work. J. B. Sonderman provided assistance in helping me to understand and overcome the receiving lens design problems. D. Milam provided the initial guidance pertaining to the film calibration procedure, and L. D. Thorson provided support for understanding and modifying the calibrated film data analysis computer program. The film development and digitization work performed by the Technical Photography group at LLL was of great assistance. The computer programming assistance given by J. E. Swanson eliminated many possible problems. S. A. Self gave freely of his time and resources to help determine an LDV arrangement that could be used successfully in the high droplet concentration, two-phase flow. There were several fruitful discussions with F. Durst that provided a great amount of insight for solving the LDV problems encountered. G. C. Dennis helped greatly through her expert coordination of the M. E. Education office and her genuine concern for the students. The assistance of R. C. Baxter and H. J. Weaver in

formulating the macros for the computer formatting of this report undoubtedly saved many hours of effort. This work was performed under the auspices of the U. S. Department of Energy by the Lawrence Livermore Laboratory under contract number W-7405-Eng-48.

Finally, I want to express my appreciation to my family. I thank my mother, E. Floyd Alger, and my grandparents, Thomas F. and Ida F. Quayle, for their support and encouragement throughout my seemingly endless educational process. My wife, MaryL M., has now endured through two degrees. My appreciation for her support cannot be adequately expressed. MaryL, I may yet be able to lower the weeds in our back yard enough that we can watch the children play. To my son, Ethan T., who was born only a couple of weeks before my preliminary exams (now 3 1/2 years old); the "book" is finished and you can now "write on it" too. To my daughter, Kendra M., who was born a few months before my qualifying exam (now 1 3/4 years old); "Daddy (can stay) home" more often now, and I will surely enjoy the change.

This work is dedicated to two great men
that never had such an opportunity:

my father

Terrance M. Alger
1922 - 1954

and my grandfather

Thomas F. Quayle
1900 -

NOMENCLATURE

a	- upper limit distribution function (ULDF) shape parameter
a_l	- combined mirror scattering and absorption loss coefficient
a_n	- Mie scattering coefficient
A	- nozzle cross-sectional area
b_n	- Mie scattering coefficient
c	- speed of light
C	- intensity profile matching procedure optimization constant
C_o	- size distribution function normalization constant
C_D	- droplet drag coefficient
C_n	- Riccati-Bessel function
d_{mv}	- LDV measuring volume diameter
d^*	- conical nozzle throat diameter
D	- droplet diameter
D_b	- laser beam diameter
D_{32}	- Sauter mean diameter
e	- internal energy per unit mass
E	- two-phase flow governing equation vector
E, $E(\theta)$	- energy density
f	- frequency
$f(\alpha)$	- particle size distribution function
F	- Fabry-Perot interferometer (FPI) finesse
F_l	- lens focal length
$g(\zeta)$	- angular scattering function

$G(\theta)$ - Mie theory amplitude function

h - enthalpy per unit mass

$h(\theta)$ - spherical aberration defocusing function

H - two-phase flow governing equation vector

- scattered light - lens intersection radius

$i(\theta,\alpha,m)$ - Mie theory scattering function

$i_d(\theta,\alpha)$ - diffraction theory scattering function

i_1, i_2 - Mie scattering functions for vertical and horizontal polarized light

i - square root of -1

$i(0)$ - transmitted light intensity

I_o - incident light intensity

$J(\theta)$ - scattered light intensity per unit solid angle

J_1, $J_{1(n+1/2)}$ - ordinary Bessel functions of the first kind

$\vec{k}_i$, $\vec{k}_s$ - LDV incident and scattered light direction unit vectors

K - optical constant

l - dispersion thickness

l_{mv} - LDV measuring volume length

L - nozzle length

m - particle relative index of refraction

m_v, m_l - vapor and total masses, respectively

$\dot{m}_v$, $\dot{m}_l$ - vapor and total flow rates, respectively

n - polytropic expansion exponent

N - total number of particles scattering light

N_ψ - particle number density

P - saturation pressure

P_R - FPI resolving power

P_n^1 - Legendre polynomial function

Q - vapor mass flow rate fraction (quality)

Q_{ext} - monodisperse scattering efficiency factor

$\bar{Q}_{ext}$ - mean polydisperse scattering efficiency factor

Q_{ULDF} - ULDF normalized width

r - radius

R - mirror reflectivity

- limiting radius

R^* - nozzle throat radius

R_D - detected pulse rate from pulse generator

Re - real part of an imaginary number

Re_D - droplet Reynolds number based upon diameter

s - object distance

s' - image distance

S - exponential size distribution shape parameter

t - time

- mirror transmissivity

T - FPI light transmission

- temperature

T_{FSR} - FSR sweep period of the FPI

u_d, u_v - droplet and vapor velocities

$\vec{u}_d$ - droplet velocity vector

u_s - isentropic homogeneous exhaust velocity

U - two-phase flow governing equation vector

v_d, v_v – droplet and vapor specific volumes

We – Weber number

X – vapor mass fraction

y^* – rectangular nozzle throat height

Y_1 – ordinary Bessel function of the second kind

z – nozzle axial distance

α – particle size parameter

$\bar{\alpha}$ – size distribution modal size parameter

α_{mm} – mass-mean size parameter

α_o – minimum size parameter

α_{10} – mean particle size parameter

α_{32} – Sauter mean particle size parameter

α_∞ – maximum size parameter

$\alpha_{\pm 1/2}$ – size distribution half width size parameters

β – LDV alignment angle

γ – light extinction coefficient

– scattering angle integration limit

δ – ULDF shape parameter

Δf – Doppler frequency shift

Δf_{FSR} – FPI frequency free spectral range

Δf_1, Δf_2 – Doppler frequency shift in light scattered from each beam of the dual beam backscatter LDV-FPI system

$\Delta\varphi$ – LDV collection aperture included angle

θ – scattering angle

λ - light wavelength

μ - dynamic viscosity

π_n - Legendre polynomial function

ρ - two-phase fluid mixture density

ρ_d, ρ_v - droplet and vapor phase densities

σ - surface tension

τ - integration variable

τ_n - Legendre polynomial function

τ_R - pulse integrator response time

φ - vapor volume fraction

- LDV beam intersection half angle

ω - solid angle

Superscript

* - nozzle throat

Subscripts

a - average

d - droplet phase

c - droplet center

e - nozzle exit

FSR - FPI free spectral range

HP - horizontal polarization

i - spatial index

k - index counter

m	- measured value
n	- index counter
NL	- natural light
p	- particle
v	- vapor phase
VP	- vertical polarization
o	- inlet (stagnation), incident (illumination) or reference value

INTRODUCTION

Geothermal energy is one of the current alternate energy sources to which considerable developmental attention is being given. Major research emphasis is being devoted to hot water deposits rather than dry team sources because they constitute a majority of the known geothermal deposits and because dry steam sources can be utilized with conventional steam turbine technology. The fluid for the hot water geothermal deposits is naturally two-phase at the wellhead unless down hole pumping is provided. The two-phase mixture of water and water vapor also includes various dissolved salts, gases, and other impurities (particulate matter, scale, etc.). In certain geothermal fields, i. e. the Salton Sea geothermal area of California, these impurities can account for as much as 30% of the total mass of the geothermal fluid.

Conventional two-phase geothermal power plants are based upon a single flashed steam cycle. In this process, the two-phase fluid is isenthalpically flashed to a lower pressure, the different fluid phases separated, and the vapor phase used to drive a conventional steam turbine. The separated liquid phase is discarded, wasting a large fraction of the available thermal energy.

To eliminate the large amount of wasted thermal energy in the discarded liquid phase of the single flashed steam cycle, direct expansion of the two-phase wellhead product to the condenser fluid state in a suitable energy conversion device has been proposed [1] - [3]. This geothermal energy conversion method, named the *total flow* process,

would utilize the thermal energy contained in both phases of the two-phase fluid, resulting in greater conversion of the available energy.

The total flow process is not limited to geothermal applications, but can be utilized for any process requiring the use of a two-phase fluid in an energy conversion cycle. Because of both the present need for energy conservation and the development of new energy sources, two-phase expanders should be seriously considered as energy conversion machines for waste-heat and solar cycles where the energy density of the working fluid is low.

One possible total flow device, which provided the impetus for this study, is an impulse turbine driven by a high-velocity, two-phase mixture exhausting from a series of converging-diverging nozzles. Because of the high vapor volume fraction, the high fluid velocity, and the negligible pressure gradient, the two-phase mixture in the nozzle jet can be considered to consist of small spherical droplets suspended in a vapor continuum. The efficient conversion of the energy in this high-velocity, two-phase fluid by an impulse turbine requires small droplets [3], [4]. The reason for this is that large droplets (> 4 μm based upon the theoretical predictions of reference [4]) will not follow the vapor streamlines within the turbine blade passages and will collide with the blade walls. This results in reduced momentum exchange and liquid film pumping losses.

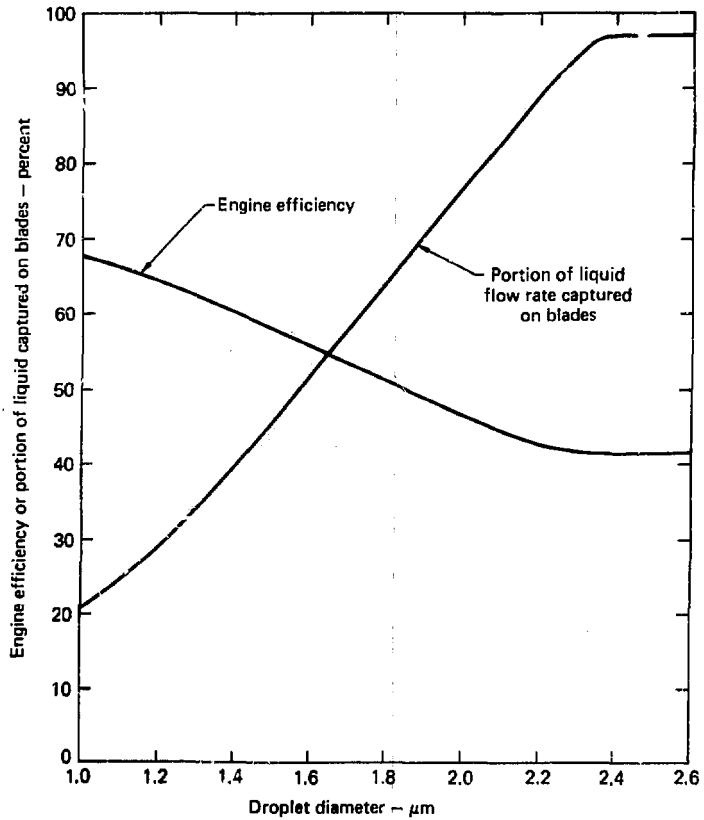

Figure 1. - Engine (isentropic) efficiency and portion of liquid captured as a function of droplet diameter for full admission (Figure 34 of reference [4]).

Figure 1 shows the calculated full admission engine (isentropic) efficiency as a function of droplet diameter for a particular experimental two-phase total flow impulse turbine [4]. The portion of the liquid phase that is captured by the blade walls is also shown as a function of the droplet size. Experimental testing of this turbine with a low-quality, steam-water mixture inlet resulted with a peak single admission engine (isentropic) efficiency near 23%. Numerical calculations based upon the two-phase fluid inlet and exhaust states agreed with this measured efficiency for nozzle exit droplet diameters greater than approximately 2.2 μm. This indicated that the experimental turbine nozzle exit droplet diameter was greater than 2.2 μm. Extrapolations to full admission turbine operation using this calculational method resulted with the information presented in Figure 1. This figure clearly demonstrates the dramatic increase in turbine performance that is associated with a reduction in droplet diameter. Thus, an important consideration of this work was the experimental determination of the nozzle exit droplet size existing in the low-quality, steam-water nozzle jet flows.

Increases in turbine efficiency with larger droplets present in the high-velocity, two-phase flow can be achieved with longer chord length (width) impulse turbine blades to permit increased blade spacing. The ideal turbine efficiency as a function of droplet diameter for several different blade widths is shown in Figure 2 [4]. The ideal efficiency for the impulse blading geometry used for the calculation presented in Figure 1 is shown for reference as the dashed line in Figure 2. It can

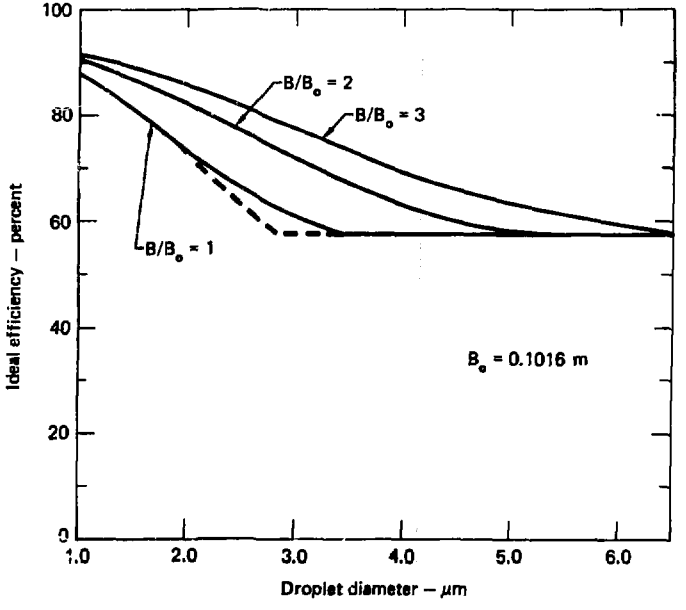

Figure 2. - Idealized rotor performance (isentropic efficiency) as a function of droplet diameter for various blade widths (Figure 35 of reference [4]).

clearly be seen from this figure that significant performance increases can be obtained for droplet diameters < 4 μm when using increased blade widths, and also that the wheel efficiency increases approximately linearly with a reduction in the droplet size. In view of this information, a nozzle design which efficiently produces droplets with diameters < 4 μm is essential for the design of a maximum efficiency turbine.

Existing two-phase nozzle flow studies can be separated into three basic categories; 1) gas-particle, 2) gas-liquid and 3) vapor-liquid nozzle flows. The two-phase, gas-particle nozzle flows are the simplest to analyze because of the fewer dominant interphase transfer mechanisms. Interest in this type of flow has arisen primarily because of the use of metalized solid propellants in rocket motors (e. g., see references [5]-[14]). The next more complex two-phase flow type is gas-liquid flow. Interest in this type of flow has been due to a wide variety of applications, e. g., gas-liquid jet pumps, magnetohydrodynamic power generation, and atomization and spraying equipment (see references [15]-[25]). The final category, vapor-liquid two-phase nozzle flow, is the most complicated of the three categories because of the highly complex interphase transfer mechanisms. Studies of this type of fluid flow have been primarily concerned with high-quality steam-water flows such as occur in steam turbines (e. g., see references [26]-[33]). However, there has also been a significant amount of information published about low-quality nozzle flows which were concerned only with the performance aspects of the nozzles, i. e., nozzle efficiencies,

static pressure profiles and mass flow rates (e. g., see references [3:]-[40]).

Unfortunately, the droplet phase characteristics of the low-quality nozzle flows were not addressed in the previous studies. In particular, no information concerning the average droplet size, the droplet size distribution, the droplet velocity and the droplet spatial variation within the liquid-dominated, two-phase nozzle flows was given. Hence, it was determined that an experimental program to measure these flow characteristics was needed. The primary objective was to develop experimental methods that would yield information concerning the droplet phase flow characteristics that are pertinent to both the impulse turbine blading and nozzle flow efficiencies for two-phase, steam-water mixtures characteristic of self-pumping geothermal wells.

Measurement of the droplet phase characteristics in the single-component, two-phase, liquid-dominated nozzle flows is difficult because of the high velocities, the small droplet diameters, the high droplet number densities, and the complex interphase transfer mechanisms. Conventional diagnostics, such as probing techniques, become unacceptable because of the serious perturbations introduced into the flow, or due to the harsh environment of the flow itself (see [41] and [42] for reviews of general two-phase flow instrumentation). For these reasons, passive measurement techniques based upon the scattering of light were chosen for the necessary two-phase flow measurements.

The droplet size distribution measurement technique developed in this study is a multiparticle light scattering method based upon the scattered light intensity variation within the forward scattering lobe. The droplet size distribution in the nozzle flow is determined by matching the measured scattered light intensity profile with a summation of the intensity contributions of a series of appropriately spaced narrow band size distributions. A numerical optimization technique is used to determine the strengths of the individual bands which yields the best agreement with the measured scattered light intensity profile. Since analytical studies [43], [44] have shown that droplet diameters < 10 μm were to be expected and because droplet diameters < 4 μm are required for efficient turbine operation, the size distribution measurement method was developed for this diameter range. The technique uses the exact Mie scattering theory [45] because there is no simple theoretical light scattering approximation for particles with diameters between approximately 1.0 and 5.0 μm for visible light wavelengths.

The spatial distribution of the droplet phase within the nozzle flow was determined through the use of two different light transmission measurement arrangements. Measurements of the droplet volume fraction across the nozzle jet was accomplished using a light extinction technique, coupled with the results of the droplet size distribution and droplet velocity measurement results. Secondly, photographs of the droplet phase spatial variation throughout the complete nozzle flow was accomplished using a pulsed ruby laser (~ 2 J in a 20 - 30 ns laser pulse) shadowgraph arrangement.

The droplet velocity measurement technique developed for this study was a dual beam backscatter laser-Doppler velocimeter (LDV) arrangement utilizing a scanning confocal Fabry-Perot interferometer (FPI) for direct optical analysis of the Doppler frequency shift of the scattered light. This arrangement is unique in that a reference beam signal is not required, and the alignment ease and stability is increased over that of other LDV-FPI arrangements because modular optical assembly can be readily utilized.

Before presenting the several experimental phases of this study, some basic material on the theoretical aspects of single-component, two-phase flow and a description of the test facility and the initial nozzle design and exploratory testing will be given. This will be followed by separate sections describing each of the specific experimental techniques and apparatus developed and the resulting two-phase nozzle flow measurements. The report is concluded with a summary of important results and conclusions.

LOW-QUALITY, TWO-PHASE NOZZLE FLOWS

GENERAL NOZZLE DESIGN OPERATING CONDITIONS

The geothermal wellhead conditions of Table 1 are representative of the fluid state corresponding to the high-temperatur , high-salinity geothermal wells of the Salton Sea area of California† [1]. The nozzle exit pressure was based upon the minimum sink temperature available at the Salton Sea area on a warm summer day, thus providing a maximum nozzle exhaust velocity for efficient use of the energy resource. This ideal design condition provided a guideline for the nozzle experimentation, but it was not strictly followed for reasons of experimental convenience.

Table 1 presents several additional aspects of the two-phase fluid expansion. It can be seen that the vapor volume fraction is very high throughout a nozzle, but the vapor mass fraction is small. This is interesting because it is the vapor phase that provides the compressibility effects necessary for the acceleration of the entire two-phase fluid within the nozzle. The low volume of the liquid phase, when coupled with the high fluid velocity within the nozzle, allows the characterization of the two-phase fluid as a cloud of small spherical droplets dispersed throughout a vapor phase continuum. The assumption of spherical droplets can be strictly applied only within low acceleration regions of the nozzle flow such that the droplet surface

† - This area is a major geothermal field in the United States and has been selected for development because the deposits are extensive and of comparatively high energy.

Table 1. - Initial nozzle design conditions.

Variable	Inlet	Exhaust
Pressure	2.48 MPa (360 psia)	12.4 kPa (1.8 psia)
Temperature	224 C (435 F)	50 C (122 F)
Enthalpy	1.31 MJ/kg (563 Btu/lbm)	1.03 MJ/kg (444 Btu/lbm)
Vapor volume fraction	0.94	0.99984
Vapor mass fraction	0.189	0.346
Isentropic homogeneous exhaust velocity	--------	742 m/s (2436 ft/s)
Droplet number per unit volume assuming a mean diameter of:		
10 μm	--------	3.06 x 10^5/cm^3
5 μm	--------	2.45 X 10^6/cm^3
1 μm	--------	3.06 X 10^8/cm^3
Droplet separation in diameters	--------	14.8

tension forces dominate the aerodynamic, buoyancy and thermal nonequilibrium forces that tend to cause droplet deformation. However, the spherical droplet assumption will yield calculations that are conservative, i. e., deformed droplets will have better interphase coupling and should break into smaller droplets than would occur if the droplets remained spherical throughout the nozzle. The experimental light scattering droplet size distribution measurements depend upon the spherical droplet assumption and were obtained in the nozzle jet flow region where the deformation producing forces on the droplets are small. Results presented in reference [46] indicate that the angular forward scattered light intensity patterns for spheroidal droplets are very

similar to those for spherical droplets, and that the possible errors would indicate larger spherical droplets than were actually present. Thus, for these reasons and because of the nozzle jet measurement location, it is expected that any droplet size distribution measurement errors due to nonspherical droplets will be small and that the droplet size measurements will be conservative.

A consequence of the large relative amount of mass present in the liquid phase is a large number of droplets per unit volume dispersed throughout the nozzle flow. This factor is of major importance to scattered light measurement techniques because of light attenuation and associated multiple scattering effects. The light attenuation is particularly important to the accuracy of the droplet size distribution measurements because light scattering theory is based upon single spherical particle scattering effects. To ensure that the light incident upon all particles within the light beam path is the same (i. e., single scattering occurs) the recommendation of [32], [47] and [48], that the light transmission of the dispersion be > 20%, was followed. The light transmission is defined as [48]

$$\frac{I(0)}{I_o} = \exp(-\gamma t) \tag{1}$$

where the extinction coefficient, γ, for a monodispersion is given by

$$\gamma = Q_{ext}(\pi D^2/4)N_v \tag{2}$$

Q_{ext}, the scattering efficiency factor, is a function of the droplet diameter and index of refraction (see Appendix A for details of the

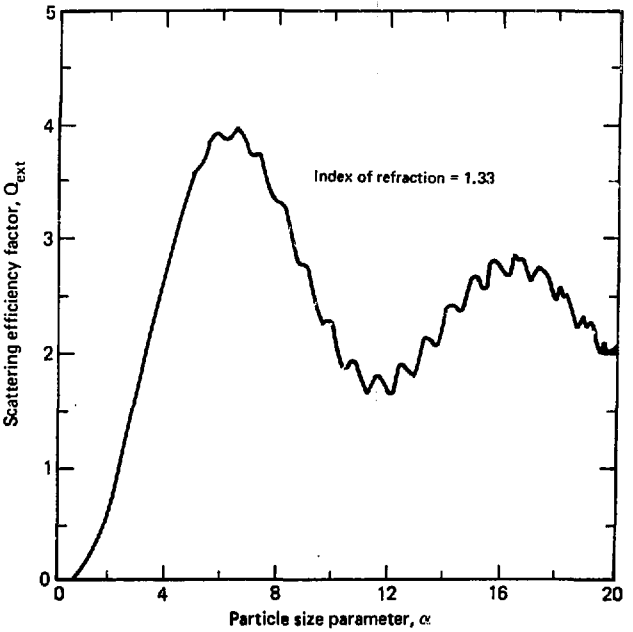

Figure 3. - Scattering efficiency factor, Q_{ext}, as a function of the particle size parameter, α.

definition of Q_{ext} and its calculation), D is the droplet diameter and N_ψ is the droplet number density. Figure 3 presents the scattering efficiency factor, Q_{ext}, as a function of the particle size parameter

$$\alpha = \left(\frac{\pi D}{\lambda}\right) \tag{3}$$

The droplet number density of equation (2) can be written in terms of the average vapor volume fraction, φ, as

$$N_\psi = \frac{(1 - \varphi)}{(\pi D^3/6)} \tag{4}$$

Thus, by the combination of equations (1), (2) and (4), the light transmission equation becomes

$$\frac{I(0)}{I_o} = \exp\left\{-\left[\frac{3(1 - \varphi)Q_{ext}}{2D}\right] \ell\right\} \tag{5}$$

which expresses the influence of the vapor volume fraction and the droplet size.

Figure 4 presents the light transmission of a low-quality, steam-water nozzle exit flow as a function of the ideal exhaust pressure for several monodiameter dispersions (based upon one-dimensional, isentropic homogeneous flow calculations). This graph clearly demonstrates the strong effect of both the vapor volume fraction and the droplet diameter on the light transmission.

The vapor volume fraction, φ, of the two-phase fluid is given by a relationship between the vapor mass fraction, X, the liquid density, ρ_d, and the mixture density, ρ, as

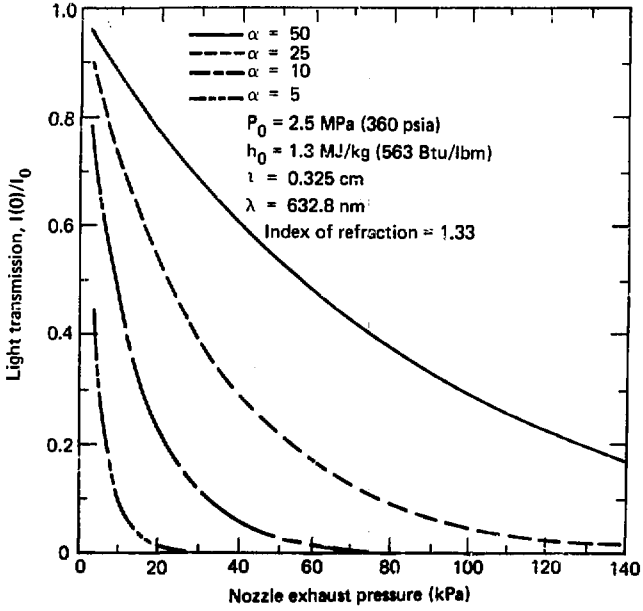

Figure 4. - Light transmission for a low-quality, steam-water nozzle exit flow as a function of the exhaust pressure for several different monodiameter dispersions.

$$(1 - \varphi) = \frac{(1 - X)\rho}{\rho_d} \tag{6}$$

from which the importance of the two-phase fluid state upon the droplet size distributon measurement can be seen. The vapor mass fraction of equation (6) is defined as

$$X = \frac{m_v}{m_t} \tag{7}$$

where m_v and m_t are the vapor and total masses, respectively, within a stationary control volume in the flow. The two-phase mixture density in this control volume can be expressed as

$$\rho = \frac{1}{[X\upsilon_v + (1 - X)\upsilon_d]} \tag{8}$$

where υ_v and υ_d are the vapor and liquid specific volumes, respectively. It must be noted that the vapor mass fraction, X, and the vapor mass flow rate fraction, Q, are not the same unless kinetic equilibrium exists between the phases. The vapor mass flow rate fraction is identical to the fluid quality as defined for use with the equation of state. The relationship between the vapor mass fraction and the vapor mass flow rate fraction is

$$Q = \frac{\dot{m}_v}{\dot{m}_t} = \frac{X}{[X + (1 - X)(u_d/u_v)]} \tag{9}$$

where $\dot{m}_v$ and $\dot{m}_t$ are the vapor and total mass flow rates, respectively. This equation clearly indicates the effect of possible kinetic nonequilibrium.

DROPLET ATOMIZATION MECHANISMS

Critical Weber Number Droplet Atomization

The classical mechanism for droplet atomization in two-phase flows is a mechanical rupture resulting from the aerodynamic forces acting on the droplet to overcome the restraining surface tension forces (see references [50] - [55]). The ratio of the aerodynamic forces to the surface tension force is the Weber number, which is defined as

$$We = \frac{\rho_v(u_v - u_d)^2 D}{\sigma} \tag{10}$$

The critical Weber number, defined as the value of the Weber number at the onset of breakup, must be determined empirically. The measurement of the critical Weber number requires a knowledge of the droplet and vapor (or gas) properties, the droplet and vapor velocities, and the initial droplet diameter. Critical Weber numbers for various droplet-gas combinations typically range between 6 and 14. However, a critical Weber number as low as 1.9 has been reported for a high-quality steam-water nozzle flow [32]. Extensive experimental studies have been conducted by Hinze [50], Lane [51] and others to determine the critical Weber number required for droplet breakup. The critical Weber number droplet breakup has also been shown to be influenced by the droplet natural frequency [53], [55] or the manner in which the continuous phase velocity varies in time [50], [54], but the aerodynamic force - surface tension interaction remains the dominant droplet breakup mechanism.

Critical Weber number droplet breakup occurs in high-velocity, two-phase nozzles because the droplets are unable to maintain kinetic equilibrium with the accelerating vapor phase. This velocity difference is a maximum in the high acceleration nozzle throat region. The maximum stable droplet diameter can be estimated by rearranging equation (10) and inserting an empirically determined critical Weber number and either a measured or calculated maximum phase velocity difference, to obtain

$$D = \frac{\sigma\, We}{\rho_v (u_v - u_d)^2} \tag{11}$$

This method of maximum droplet diameter calculation for computer programs has been used in references [15] and [43] for detailed calculations of quasi-one-dimensional, two-phase nozzle flows. The analysis assumes that the droplets breakup to the maximum stable diameter, forming a monodiameter droplet disperson. Numerical results show that the breakup occurs principally in the nozzle throat region where the fluid acceleration is a maximum. Calculations using these methods demonstrate that enhanced atomization may occur with nozzle throat designs that promote higher vapor phase accelerations (small throat diameters and radii of curvature). Thus, the importance of a geometry dependent nozzle calculation, as developed by Comfort, et. al. [43], for two-phase nozzle flow predictions is evident.

Thermal Nonequilibrium (Boiling) Droplet Atomization

A second droplet breakup model that is especially applicable to single-component, two-phase nozzle flows is the breakup of droplets due to thermal nonequilibrium boiling effects [44]. This model, named the boiling breakup model, depends only upon the temperature difference between the droplet interior and the vapor phase. In single-component, two-phase nozzle flows, the heat transfer resistance from the droplet surface to the continuous vapor phase is small when compared to the thermal resistance for conduction within the droplet itself. As the low-quality, two-phase fluid expands through the nozzle, the vapor phase cools rapidly. The surface temperature of the droplets is maintained at the vapor phase temperature by convection and evaporation, but there is a lag of the internal droplet temperature due to the finite heat conduction rate within the droplet. The higher temperature at the droplet center leads to boiling (cavitation) and resulting droplet breakup.

For small droplets the surface tension induced internal droplet pressure can be significant, which tends to prevent boiling. The maximum stable droplet diameter results when the saturation pressure corresponding to the internal temperature of the droplet equals the external pressure plus the pressure due to the surface tension. This pressure equilibrium condition can be expressed as

$$P(T_c) = P(T_v) + 4\sigma/D \qquad (12)$$

Upon breakup, the newly formed droplets will, in general, be of different temperatures, depending upon the location of their origin in the original droplet. Because of this, it becomes calculationally convenient to use the droplet mass averaged temperature rather than the center temperature to determine the maximum stable droplet size. Solving equation (12) for this droplet diameter yields [44]

$$D = \frac{4\sigma}{[P(T_a) - P(T_v)]} \tag{13}$$

The use of equation (13) for the calculation of the maximum stable droplet diameter is more fundamental than the use of the critical Weber number breakup criterion, in that it requires no empirically determined parameters.

THEORETICAL MODELING OF LOW-QUALITY, TWO-PHASE NOZZLE FLOWS

The prediction of single-component, two-phase flow through a converging-diverging nozzle is difficult because of the mass, momentum and energy transfer mechanisms that exist between the phases. The additional complications of droplet - wall impact and boundary layer - liquid film shear and droplet shedding (the wall liquid film will be thin because of the small liquid volume and may be in the form of rivulets) in combination with the fluid turbulence effects must be considered in the two-phase model for a complete analysis. Even when including only the simplest reasonable models, the two-phase equations of motion must be solved numerically. Presently available calculational techniques are already complex, but they employ relatively simple models

and neglect many two-phase flow complexities because of a lack of experimental information, a physical understanding of the phenomena involved and the computer speed and storage required.

Because of the specific two-phase nozzle flow application which prompted this study, it was decided that the quasi-one-dimensional solution technique of Comfort, et. al. [43] would be the most useful of the existing two-phase flow solution methods (see reference [43] for a discussion of the applicability of the existing two-phase flow solution techniques to total flow impulse turbine and nozzle design work). This solution technique is geometry dependent so that the effects of the nozzle throat geometry on the droplet phase characteristics can be modeled. The thermal equilibrium model (entitled 1D2FAZEQ) [43], utilizing a critical Weber number droplet breakup criterion, and the thermal nonequilibrium model (entitled 1D2FAZNEQ) [44], utilizing a boiling breakup criterion, will both be used for the two-phase nozzle flow predictions and experimental comparisons. The equations of motion, the pertinent assumptions and the solution technique for these two numerical methods will be briefly discussed next.

Thermal Equilibrium Numerical Model (1D2FAZEQ)

The numerical determination of the quasi-one-dimensional, two-phase nozzle flowfield variables requires the simultaneous solution of either a set of coupled partial differential equations or a set of partial differential equations coupled with ordinary differential equations,

depending upon the equation formulation reference frame. The different possible equation formulations for two-phase flow modeling (e. g , Eulerian mixture - Lagrangian droplet, Eulerian vapor - Eulerian droplet, etc.) are discussed in detail by Comfort [4]. The thermal equilibrium calculational model was formulated using the partial differential equations corresponding to the two-phase mixture derived in an Eulerian reference frame and the ordinary differential equations for the droplet phase derived in a Lagrangian reference frame. This formulation of the governing equations requires the solution of two continuity equations, two momentum equations, one energy equation and one equation of state for pure water using thermal equilibrium saturated fluid properties. Since the nozzle geometry is specified, the six unknown solution variables are: pressure, P, mixture density, ρ, mass fraction, X, vapor velocity, u_v, droplet velocity, u_d, and droplet diameter, D.

The time dependent, two-phase Eulerian mixture continuity, momentum and energy equations of motion are written as

$$\frac{\partial U}{\partial t} + \frac{\partial E}{\partial z} + H = 0 \tag{14}$$

where

$$U = \begin{Bmatrix} \rho A \\ \rho A[Xu_v + (1 - X)u_d] \\ \rho A[X(e_v + u_v^2/2) + (1 - X)(e_d + u_d^2/2)] \end{Bmatrix} \tag{15}$$

$$E = \begin{Bmatrix} \rho A[Xu_v + (1 - X)u_d] \\ \rho A[Xu_v^2 + (1 - X)u_d^2] + PA \\ \rho A[Xu_v(h_v + u_v^2/2) + (1 - X)u_d(h_d + u_d^2/2)] \end{Bmatrix} \tag{16}$$

$$H = \begin{Bmatrix} 0 \\ -P\dfrac{dA}{dz} \\ 0 \end{Bmatrix} \tag{17}$$

The mixture equations are introduced in this form to facilitate their solution using the time dependent MacCormack numerical technique [56]. This is a non-centered differencing scheme requiring no explicit artificial viscosity for the calculation of shock wave effects. By using time dependence, hyperbolic equations are maintained for both the subsonic and the supersonic flow regimes, eliminating flow regime matching problems.

The momentum (droplet drag) equation for an individual droplet, derived in the Lagrangian reference frame is given by

$$\rho_d u_d \frac{du_d}{dz} = \frac{3\rho_v C_D}{4D}(u_v - u_d)|u_v - u_d| - \frac{dP}{dz} \tag{18}$$

where the droplet drag coefficient, C_D, for a single droplet is given by [15]

$$C_D = 3.271 - 0.8893(\ln Re_D) + 0.03417(\ln Re_D)^2 + 0.001443(\ln Re_D)^3 \tag{19}$$

which is applicable for the droplet Reynolds number range:

$0.1 < Re_D < 2 \times 10^4$. The effect of nearby droplets or droplet deformation on the drag coefficient and the effect of the virtual mass and Bassett forces on the droplets have been neglected for calculational simplicity, but could be included if desired. Equation (18) is applicable to the trajectory of a single droplet for given initial conditions. Because a steady-state solution is desired, the initial conditions for all droplets of a given size, beginning at a particular point in space, is assumed to be the same. Furthermore, the trajectory of a single droplet is the locus of all droplets of the same initial conditions, throughout problem space.

Because of the thermal equilibrium assumption, either the continuity or the energy equation related to the droplet field can be eliminated. The steady-state continuity equation is simpler to use and is given as

$$D = D_o \left[\frac{(1 - X)}{(1 - X_o)} \left(\frac{\rho}{\rho_o} \right) \left(\frac{\rho_{do}}{\rho_d} \right) \left(\frac{u_d}{u_{do}} \right) \left(\frac{A}{A_o} \right) \right]^{1/3} \tag{20}$$

Droplet size reduction can occur as a result of evaporation (equation (20)) or atomization (critical Weber number breakup equation (11)); the mechanism producing the smaller size (maximum stable droplet diameter) being operative.

The equation of state (saturation) relations used for the Eulerian mixture calculations are

$$\rho_v = \rho_v(P) \; ; \; \rho_d = \rho_d(P) \; ; \; h_v = h_v(P) \; ; \; h_d = h_d(P) \; ;$$
$$e_v = e_v(P) \; ; \; e_d = e_d(P) \qquad (21)$$

and the equation of state relations used for the Lagrangian droplet calculations are

$$\mu_v = \mu_v(P) \; ; \; \sigma = \sigma(P) \qquad (22)$$

The saturation properties, equations (21) and (22), were utilized as functions of the saturation pressure, rather than saturation temperature, for calculational ease. Cubic spline curve fits of these properties, based upon the computerized ASME steam tables [57], were used for calculational speed (prior to the use of cubic spline curve fits approximately 80% of a problem run time was equation of state related).

Figure 5 presents a description of the numerical solution method utilizing this system of equations. An iterative procedure that alternates between the Eulerian mixture and the Lagrangian droplet systems of equations is used to determine the final steady-state solution.

Thermal Nonequilibrium Numerical Model (1D2FAZNEQ)

The modification of the thermal equilibrium calculational model to include the effects of thermal nonequilibrium and boiling droplet breakup is conceptually simple. The thermal nonequilibrium model

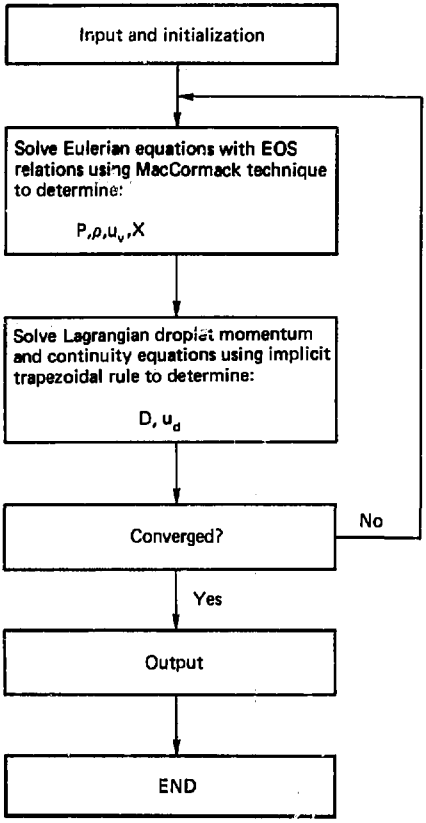

Figure 5. - Thermal equilibrium numerical solution procedure (1D2FAZEQ).

utilizes the Eulerian mixture equations and the Lagrangian droplet momentum equation (equations (14) - (19)) as in the equilibrium model, but the droplet continuity equation, equation (20), is replaced by the Lagrangian droplet energy equation written in finite difference form as [44]

$$D_{i+1} = \frac{D_i \rho_{d,i} (h_{va} - e_{d,i})}{\rho_{d,i+1} (h_{va} - e_{d,i+1})} \tag{23}$$

where

$$h_{va} = (h_{v,i} + h_{v,i+1})/2 \tag{24}$$

Droplet size reduction can occur as a result of evaporation (equations (23) and (24)) or atomization (boiling breakup equation (13)); the mechanism producing the smaller size (maximum stable droplet diameter) being operative.

The equation of state relations for the thermal nonequilibrium Eulerian portion of the calculations are

$$\rho_v = \rho_v(P) \; ; \; \rho_d = \rho_d(P) \; ; \; h_v = h_v(P) \; ; \; e_v = e_v(P) \; ;$$
$$h_d = c_{} T_d \; ; \; e_d = h_d - P/\rho_d \tag{25}$$

and the equation of state relations for the Lagrangian droplet portion of the calculation are given by equation (22).

The system of equations for the thermal nonequilibrium solution is now complete except for the relations necessary to calculate the droplet temperature. The droplet temperature is modeled using the superposition

of two different solutions for thermal conduction in a spherical droplet. One solution is that of a step temperature change in the droplet surface temperature, corresponding to the temperature change in the vapor phase, as the droplet moves through the computational cells of the finite difference grid. The second droplet conduction solution accounts for the vapor phase temperature variation (assumed to be a ramp) from cell to computational cell. The superposition of these two droplet conduction solutions yields an average value for the thermal nonequilibrium droplet temperature as a function of position within the calculational grid. A schematic of the numerical solution process for the thermal nonequilibrium model is shown in Figure 6.

PREDICTED EFFECT OF NOZZLE GEOMETRY ON DROPLET PHASE CHARACTERISTICS

Nozzle Throat Geometry for Maximum Velocity Gradient

Analytical studies of two-phase, gas-particle flows in rocket nozzles [7] have shown that the expansion of the two-phase mixture in the throat region can be treated as a single phase with an adjusted polytropic expansion exponent, n. The velocity gradient in the throat region of an axisymmetric nozzle is then given by

$$\frac{du_v^*}{dz} = u_v^* \left[\frac{4}{(n+1)R^* d^*}\right]^{1/2} \tag{26}$$

where R^* is the throat radius of curvature and d^* the throat diameter.

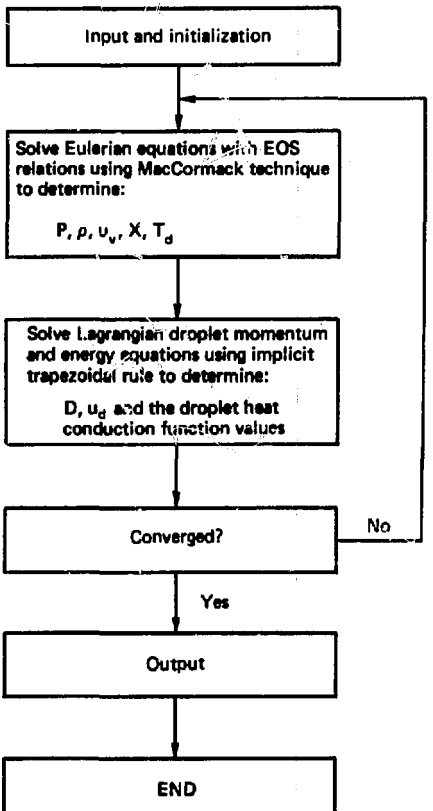

Figure 6. - Thermal nonequilibrium numerical solution procedure (1D2FAZNEQ).

Equation (26) is an explicit functional relation from which the effects of changes in the nozzle throat radius of curvature and diameter on the nozzle throat velocity gradient can be predicted. By increasing the fluid velocity gradient (i. e., a reduction in R^* and/or d^*) in the nozzle throat region the gas-droplet velocity difference is increased, which increases droplet breakup due to both aerodynamic forces and thermal nonequilibrium effects. However, there is a practical limit to the minimum values for R^* and d^* that can be utilized. The throat diameter is mainly limited by boundary layer displacement thickness considerations and mass flow rate requirements, but as the throat radius of curvature becomes very small there will be a radius (depending upon the nozzle flow inlet conditions) for which the flow is unable to follow the nozzle wall, and boundary layer separation will occur immediately downstream of the nozzle throat. Because of the favorable pressure gradient, the boundary layer will reattach at a location downstream of this separation point, but the flow geometry will be determined by the fluid flow at the separation point and not the actual nozzle wall geometry. Thus, there must be a practical limit realized for the fluid acceleration in the nozzle throat region.

Numerical Nozzle Flow Predictions

Although the validity of the computer programs described in the previous sections has not been established, they are capable of indicating the trends to be expected from nozzle geometry changes. Therefore, to aid in planning and understanding the experimental

program, calculations of low-quality, two-phase nozzle flows were carried out. These predictions were made specifically to investigate the theoretical effect of nozzle throat geometry on the droplet phase characteristics for rectangular cross-section nozzles (rectangular cross-sections were chosen to be consistant with the impulse turbine and experimental nozzle geometries). The calculations were made using both 1D2FAZEQ and 1D2FAZNEQ for three different nozzle throat radii of curvature (2.540 cm, 1.270 cm, and 0.318 cm radii), while the remainder of the nozzle geometry was held constant. Also, nozzle flow predictions were made using 1D2FAZEQ for the different radii of curvature and two different throat heights (0.318 cm and 0.635 cm). The calculations were performed for the nozzle inlet conditions and geometries approximating available experimental values (see the two-phase flow experimental apparatus section for a discussion of the use of the theoretical models for the initial experimental nozzle design). Both 1D2FAZEQ and 1D2FAZNEQ were used for the calculations to investigate the changes in the droplet phase produced by the different atomization mechanisms. 1D2FAZEQ calculations are based upon a critical Weber number droplet breakup criterion. Although there is no definitive experimental information regarding the correct value of the critical Weber number to be used for low-quality steam-water mixtures, these calculations were based upon a value of 6.0, which is the commonly used value for two-component droplet breakup in nozzles.

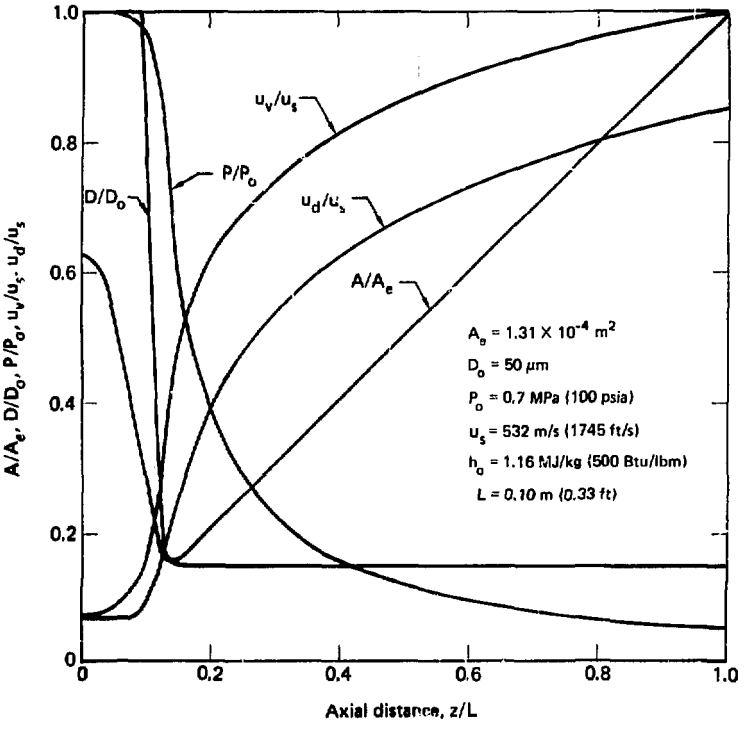

Figure 7. - 1D2PHAZEQ predicted results showing the dimensionless nozzle area profile, droplet diameter, pressure and phase velocities versus distance along the nozzle axis.

Figure 7 presents the 1D2FAZEQ predicted nozzle flowfield variables for the indicated geometry and inlet conditions. All variables are plotted in the same figure to demonstrate the importance of the nozzle throat geometry on the droplet phase characteristics. The nozzle throat region is the location where esentially all the droplet breakup occurs. Droplets are accelerated in the diverging section of the nozzle but further breakup is negligible. It should be noted that these calculations are based upon the assumption of one-dimensional flow and thus, cannot account for any spatial (two- or three-dimensional) variation of the droplet phase characteristics.

The predicted effect of the throat radius of curvature and throat height upon the droplet diameter at the nozzle exit for constant inlet conditions is shown in Figure 8. This graph clearly demonstrates the predicted effect of the nozzle throat geometry on the droplet diameter. It can be seen that the droplet diameters predicted by 1D2FAZNEQ are of the same order (about 15% smaller) as those predicted by 1D2FAZEQ using a critical Weber number of 6.0. A value of 1.0 for the critical Weber number results with diameters much smaller than those predicted using the boiling breakup model.

Figure 9 presents the predicted droplet velocity at both the nozzle throat and the nozzle exit as a function of the throat radius of curvature (see Figure 8 to correlate with the nozzle exit droplet diameter). Because of the nozzle length required to expand the steam-water mixture to subatmospheric pressures ($A_e \approx 3$ at 101.4 kPa

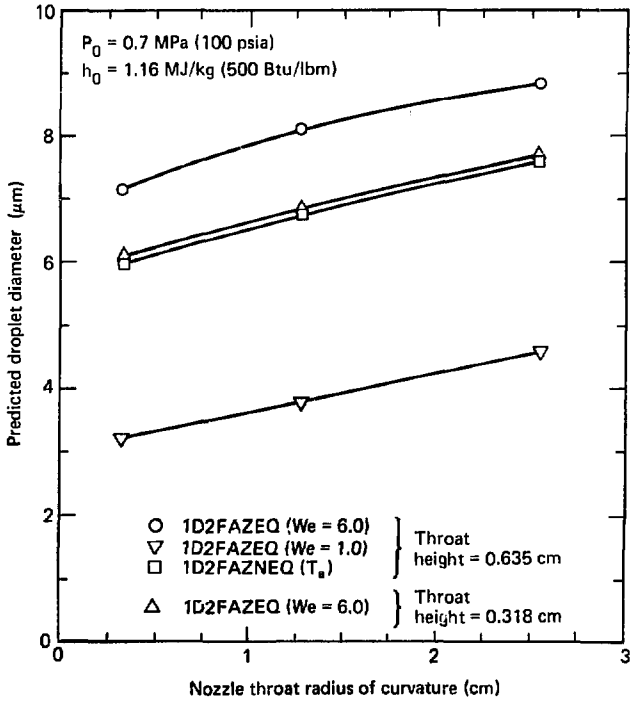

Figure 8. - Calculated results using both 1D2FAZEQ and 1D2FAZNEQ for demonstrating the effect of nozzle throat radius of curvature and throat height on the droplet diameter.

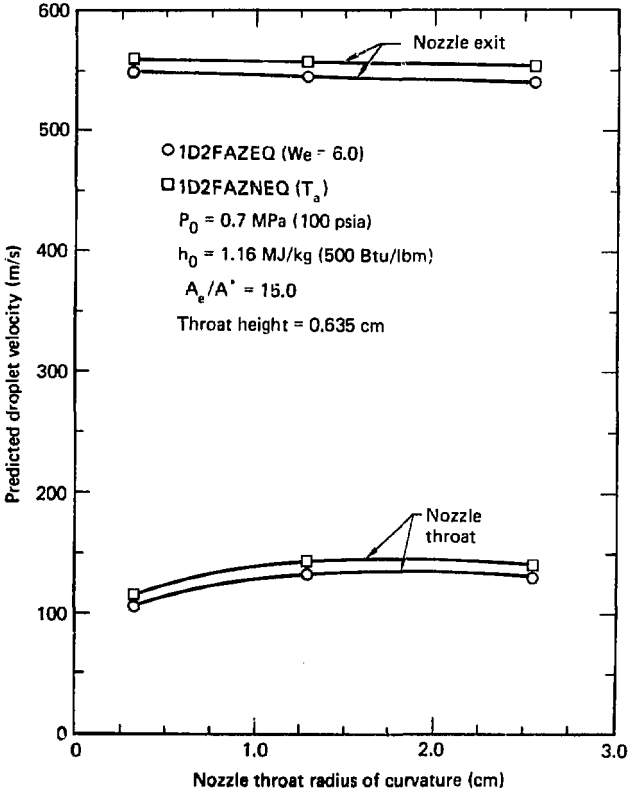

Figure 9. - 1D2FAZEQ and 1D2FAZNEQ predicted droplet velocities at the nozzle exit and throat versus the throat radius of curvature.

(14.7 psia) while $A_e = 15$ at 13.8 kPa (2.0 psia) because of the large water vapor specific volume changes at subatmospheric pressures) and because of the relatively small differences between the predicted nozzle exit droplet diameters in terms of the droplet momentum considerations, the droplet velocity at the nozzle exit is nearly constant with respect to the throat geometry variation. At the nozzle throat, however, there is a much greater percentage change in the droplet velocity with a change in the throat radius of curvature. This velocity variation is caused by both the different droplet diameter histories occuring within the high acceleration throat region and the different nozzle lengths required to reach the minimum area (because of the different radii of curvature).

The results of the calculations presented in Figure 9 indicate that the determination of the nozzle exit droplet diameter from a correlation between a droplet velocity measurement and a numerical prediction of the droplet exit velocity is not practical (see reference [58] for a report upon this concept for a simple two-component, two-phase nozzle flow). However, the measurement of the droplet velocity, in conjunction with an independent droplet diameter measurement, will provide complementary information concerning both the liquid-phase flow within the nozzle and the accuracy of the numerical prediction methods. Thus, the droplet velocity measurements obtained during this study were used only to complement the other measurement techniques in determining the nozzle flow characteristics and the spatial variation of the droplet size and concentration within the nozzle jet flows.

TWO-PHASE FLOW EXPERIMENTAL APPARATUS

GEOTHERMAL TEST FACILITY

The droplet phase characteristics studies were conducted using nozzles operating at the geothermal test facility at the Lawrence Livermore Laboratory. The test facility was designed to provide clean-water, two-phase flow conditions characteristic of those produced at the wellhead of self-pumping geothermal wells. Figure 10 presents a schematic representation of the interior of this two-phase flow test facility, showing the control room and the different possible test stations. Figure 11 is a photograph of the test facility exterior, showing the hot water generator, condenser system and related support equipment. A complete description of the geothermal test facility is given by Weiss and Shaw [59].

TWO-PHASE NOZZLE TEST STATION

Figures 12 and 13 present operational schematics of the nozzle test station and nozzle test chamber, respectively. The compressed liquid from the hot water generator is isenthalpically flashed to a two-phase mixture by a control valve prior to the nozzle entrance. The resulting two-phase mixture is then expanded through the test nozzle to an exhaust pressure controlled by a condenser - vacuum pump system combination. The flash control valve regulates the nozzle inlet pressure by controlling the total mass flow rate entering the nozzle. A liquid bypass line that connects the hot water generator directly with the

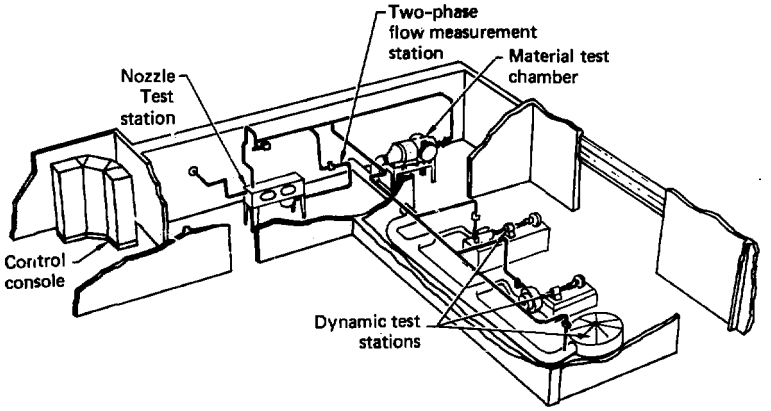

Figure 10. - Schematic representation of the geothermal two-phase flow test facility interior.

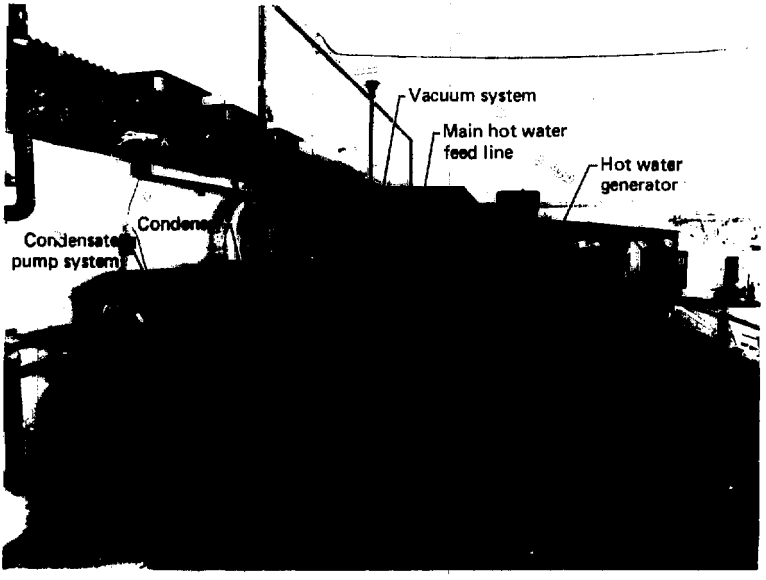

Figure 11. - Photograph of the geothermal two-phase flow test facility exterior.

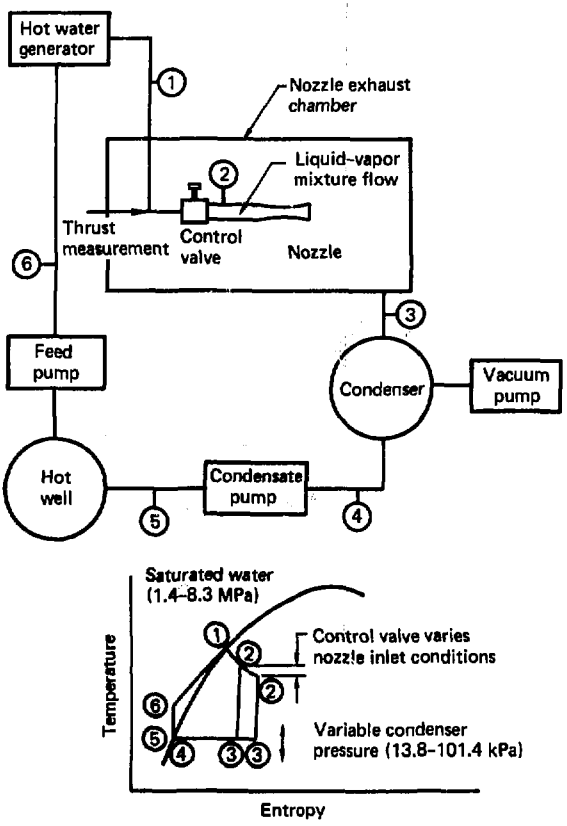

Figure 12. - Schematic representation (upper) and operation cycle (lower) of the nozzle test station.

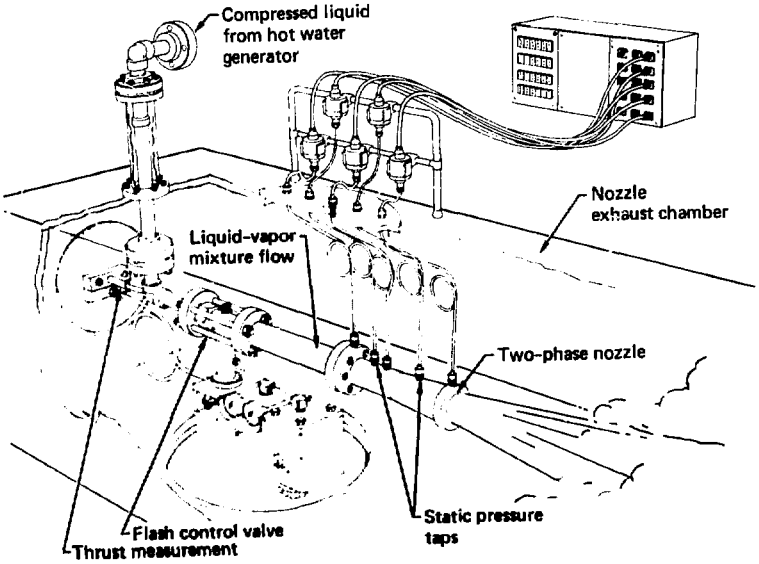

Figure 13. - Nozzle test chamber schematic representation.

condenser system is regulated by an automatic control valve to allow variations in nozzle mass flow rate (inlet pressure) to occur while maintaining the hot water temperature and pressure (enthalpy) constant. The capability for total mass flow rate and thrust measurements are included at the nozzle test station (see reference [40]) but were not utilized for this study. The pressure and temperature data (hot water generator conditions and nozzle static wall taps) were collected in the control room (see Figure 14) and recorded on paper tape.

EXPERIMENTAL TWO-PHASE NOZZLES AND DESIGN CONSIDERATIONS

A total of six different nozzle configurations were tested during the various phases of the droplet phase characteristics work. The nozzles were rectangular in cross-section and of constant thickness in the dimension parallel to the diagnostic laser beam direction. Figure 15 presents the different numerical designations and geometries for these nozzles. The nozzles were designed using the thermal equilibrium theoretical model (1D2FAZEQ) since the thermal nonequilibrium model (1D2FAZNEQ) was not available at nozzle design time.

Experimental Nozzle Geometries and Test Conditions Determination

Nozzle number 1 was designed with the intent of establishing a baseline nozzle for the droplet phase characteristics determination study, i. e., an experimental nozzle to simulate the total flow impulse turbine nozzle throat geometry [4] and to provide an experimental

Figure 14. - Photograph of the geothermal two-phase flow test facility control room.

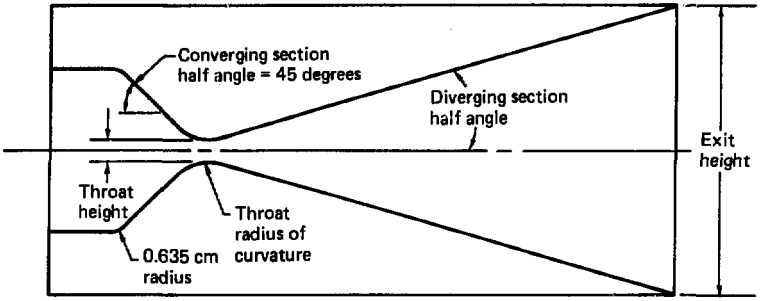

Nozzle No.	Throat radius of curvature (cm)	Throat height (cm)	Thickness (cm)	Diverging half angle (deg)	Exit height (cm)
1†	0.635	0.440	1.750	10.0	5.53
2	0.051	0.635	0.325	17.5(10.7)††	9.53
3	0.318	0.635	0.325	11.1	9.53
4	2.540	0.635	0.325	11.2	9.53
5	0.051	0.318	0.325	17.5(10.7)††	9.21
6†	0.318	0.635	1.905	11.1	9.53

†Transparent sidewalled nozzle.

††Nozzle no's. 2 and 5 had a compound angle divergence section. The divergence half angle was 17.5 degrees just after the throat, which rapidly tapered into 10.7 degrees for the majority of the diverging section length.

Figure 15. - Numerical designations and dimensions of the experimental nozzles.

verification of the usefulness of the droplet phase characteristics measurement techniques and the accuracy of the numerical flow models. The nozzle was designed to incorporate the use of transparent sidewalls to allow experimentation using all the proposed droplet phase diagnostics. The transparent sidewalls were fabricated of 2.54 cm thick pyrex glass plates to be able to safely withstand the high temperature and high pressure operating conditions (the steam-water mixture temperature is 224 C (435 F) at a pressure of 2.5 MPa (360 psia)). A photograph of nozzle number 1, as installed in the nozzle test chamber, is shown in Figure 16. The nozzle exhaust was connected directly to the condenser piping to eliminate the requirement of a vacuum in (or windows on) the nozzle exhaust chamber.

Because of the limited expansion ratio of nozzle number 1 (limited to $A_e/A^* = 12.6$ for a reasonable divergence angle, length and mass flow rate), the exit pressure for the 2.5 MPa (360 psia) inlet pressure, 18.9% inlet quality nozzle expansion is calculated using 1D2FAZEQ as 57.9 kPa (8.4 psia). This relatively high pressure and the resultingly low vapor volume fraction, when combined with the predicted droplet diameter of 5 μm and the 1.75 cm nozzle thickness, yields a very low value for the light transmission. This eliminated the possibility of any light scattering droplet size measurements at the high pressure inlet condition. However, a 1D2FAZEQ calculation for this nozzle, operating at an inlet pressure of 0.7 MPa (100 psia) and an inlet quality of 29.7%, yielded an exit pressure of 14.5 kPa (2.1 psia) and a resulting light transmission of near 22% (the predicted droplet diameter

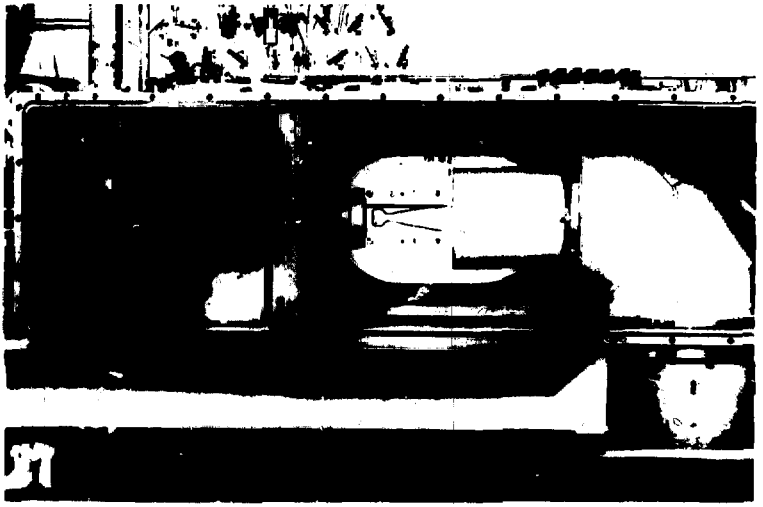

Figure 16. - Photograph of the transparent sidewalled nozzle number 1 installed in the nozzle test chamber.

increased to 6.1 μm at this lower pressure inlet condition) for a light wavelength of 632.8 nm (He-Ne laser). This calculation indicates that light scattering droplet size measurements should be possible at the lower nozzle inlet pressure conditions, provided that the predicted droplet size is correct. Since the laser-Doppler velocimeter and the shadowgraph measurements are not as sensitive to the dispersion transparency as the light scattering measurements, nozzle number 1 was fabricated for the initial testing of the laser diagnostic techniques.

During the two-phase flow testing of transparent nozzle number 1, several unexpected problems became evident. It was determined that the light transmission at the nozzle exit was much lower than that calculated using 1D2FAZEQ (indicating much smaller than predicted droplet diameters), even at the lowest reasonable inlet pressure of 344.7 kPa (50 psia) (inlet quality near 34% and exit pressure near 10.3 kPa (1.5 psia)). This completely eliminated the possibility of light scattering droplet size distribution measurements for this nozzle. Also, it was found that the droplet - transparent wall impact created a thin liquid film on the transparent wall that caused a great amount of disturbance to the laser beam diagnostics, causing inaccurate light transmission measurements and eliminating the laser beam focus intersection necessary for the laser-Doppler velocimeter measurements. However, it was determined that the pulsed ruby laser shadowgraph system would work well for this transparent nozzle arrangement, yielding photographs of the complete nozzle flowfield.

The use of nozzle number 1 to test the different diagnostic techniques yielded several important results. Because of the high light attenuation that is characteristic of smaller than predicted droplets existing within the nozzle flow, it was determined that very thin (parallel with the laser beam direction) nozzles would be required for the light scattering droplet size distribution and light transmission measurements. The actual nozzle thickness, 0.325 cm (nozzle numbers 2 - 5), was chosen only after extensive consideration of both the light transmission requirements and the calculated effects of the boundary layer [60]† upon the nozzle flow characteristics. Also, it was found that nozzle jet flow measurements of the droplet size distribution, droplet velocity and droplet spatial variation were required to avoid transparent wall - liquid film disturbances. Fortunately, the shadowgraph photographs of the entire flowfield could be accomplished with the transparent sidewalled nozzles, even when the light attenuation by the flow was extremely high (transmission << 20% in the high pressure flow regions). These important results led to the design and incorporation of the experimental nozzle numbers 2 - 6 (variable nozzle arrangements) for the droplet characteristics - nozzle wall contour changes study.

† - A two-phase boundary layer prediction method based upon an integral techniquo was developed to calculate the effects of the boundary layer on the flow between turbine blades and in nozzles. Because of the momentum source due to the droplets entering a two-phase dispersed droplet-in-vapor boundary layer, the calculated boundary layer thickness and shear stress was essentially constant with distance along the nozzle wall. This resulted with a much thinner boundary layer at the nozzle exit (this is consistant with the experimental observations) than would be predicted by modeling the two-phase boundary layer as a single dense phase.

Variable Two-Phase Nozzle

The variable nozzle (nozzle numbers 2 - 6) was designed to allow extensive experimental flexibility. The nozzle body was designed to readily incorporate the use of many different nozzle wall contour variations using replaceable nozzle walls, i. e., the throat radius of curvature, the throat height and the nozzle thickness could be easily modified using interchangeable nozzle wall contours. It was also designed to operate both in an open jet mode (using metal sidewalls and enclosed within the nozzle exhaust vacuum chamber) for the light scattering droplet size distribution, the light transmission droplet spatial distribution and the LDV droplet velocity measurements, and in a closed jet mode (using transparent sidewalls with the nozzle connected directly to the condenser piping) for the shadowgraph photographs. Figure 17 is a photograph of the disassembled variable nozzle showing the contours corresponding to the variable nozzle numbers 2 - 5.

Photographs of the open jet variable nozzle arrangement, as installed in the nozzle test chamber, are presented in Figures 18 and 19. These figures clearly indicate the complexity of the geometry required to contain the nozzle in a sealed vacuum chamber and still maintain the close coupling required by the optical components. The diffuser was necessary to collect the nozzle jet flow to avoid window wetting problems. However, window wetting did occur during warmup and when the nozzle was operating at off design back pressures, requiring the wiper arrangement for removing the spray prior to any measurements.

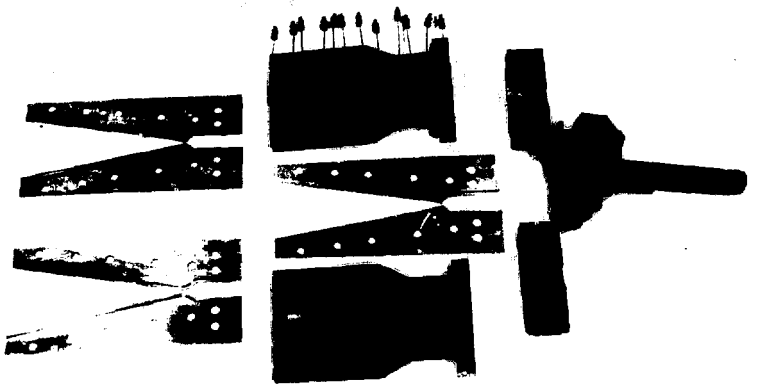

Figure 17. – Photograph of the disassembled variable nozzle. The nozzle wall contours shown correspond to nozzle numbers 2 – 5.

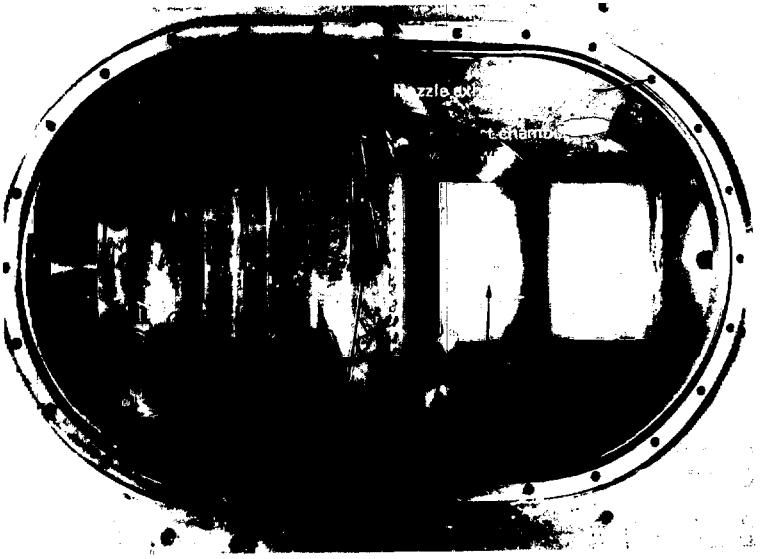

Figure 18. - Side view photograph of the variable nozzle open jet arrangement installed in the nozzle test chamber.

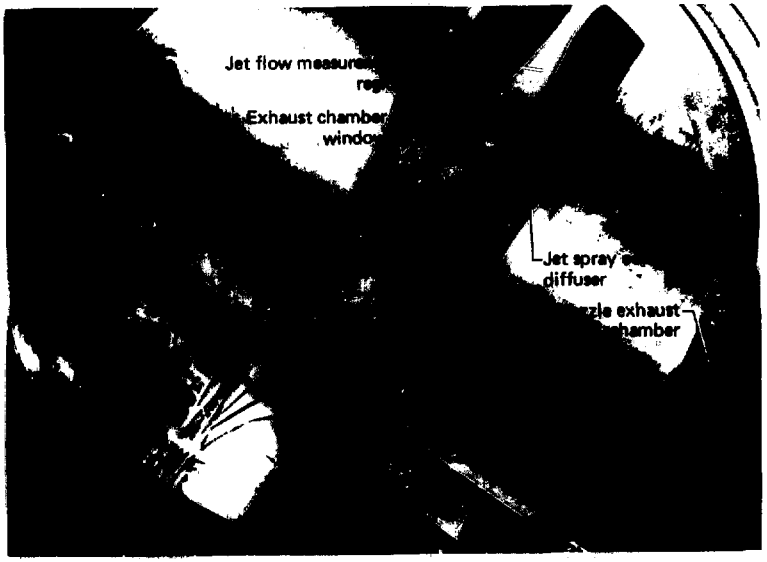

Figure 19. - Top view photograph of the variable nozzle open jet arrangement installed in the nozzle test chamber.

Also, to avoid window condensation problems, it was found that the windows had to be maintained at a temperature higher than that of the fluid saturation state within the exhaust chamber. This condition was achieved by operating the exhaust chamber at atmospheric pressure (i. e., a temperature of 100 C (212 F)) for a period of time to heat the windows prior to the droplet phase characteristics measurements for which subatmospheric pressure (lower fluid saturation temperature) was required.

A photograph of the transparent walled variable nozzle number 6, as installed in the nozzle test chamber, is shown by Figure 20. The nozzle exhaust is connected directly to the condenser piping to eliminate the requirement of a vacuum in (or windows on) the nozzle exhaust chamber. The nozzle thickness was chosen at 1.91 cm to be used with the shadowgraph flow visualization system only. The transparent walls were again fabricated of 2.54 cm thick pyrex glass plates to preclude any sidewall failures due to the high temperatures and pressures of the two-phase nozzle flow.

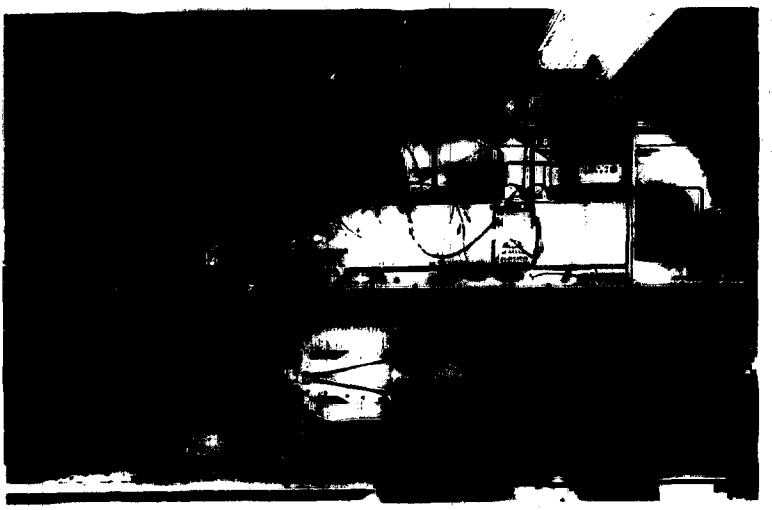

Figure 20. - Side view of the variable transparent walled nozzle number 6 installed in the nozzle test chamber.

LIGHT SCATTERING

DROPLET SIZE DISTRIBUTION DETERMINATION

LIGHT SCATTERING BY SPHERICAL PARTICLES

The light intensity scattered by a spherical particle† depends upon the incident light intensity, wavelength and polarization, the particle diameter and refractive index, and the observation direction relative to the illumination direction. The basic theory for the scattering of collimated monochromatic light by a single spherical particle in a homogeneous medium was developed by Mie [45]. The result for the intensity per unit solid angle of the scattered light, $J(\theta)$, as a function of the angle from the incident direction is expressed in terms of the Mie scattering function, $i(\theta,\alpha,m)$, by [49]

$$J(\theta) = K\, i(\theta,\alpha,m) \tag{27}$$

where

$$K = \left(\frac{\lambda}{2\pi}\right)^2 I_o \tag{28}$$

The particle size parameter, α, is given by equation (3). Calculations based upon equation (27) have shown that for a particle whose diameter is nearly equal to the incident light wavelength, the structure of the scattered light intensity distribution is very complex. For particles much smaller than the incident light wavelength the Mie theory

† - A discussion of the reasons for the spherical droplet assumption and the possible errors involved with nonspherical droplets is presented on page 10 of this report.

calculations can be approximated by the simpler Rayleigh-Gans theory. For particles much larger than the incident light wavelength the simpler diffraction theory becomes applicable as an approximation to Mie theory. The Mie scattering function, $i(\theta,\alpha,m)$, and its calculation is presented in Appendix A.

The results obtained from the scattering of light by a single spherical particle can be directly extended to the scattering of light by a cloud of monodiameter particles using superposition to obtain [49]

$$J(\theta) = K\, N\, i(\theta,\alpha,m) \tag{29}$$

where N is the number of particles scattering light. This equation is applicable for a monodispersion provided that the light incident upon all particles has not been significantly altered by the scattering effects of the other particles, i. e., single scattering occurs. The topic of monodisperse particle sizing is discussed in detail in references [49], [61] - [63].

The light scattered from a dispersion containing particles of many different sizes can be determined by the superposition of the scattering effects of each particle in a manner similar to the monodisperse particle sizing represented by equation (29). By defining a particle size distribution function, $f(\alpha)$, as

$$\int_0^\infty f(\alpha)d\alpha = N \tag{30}$$

the scattered light intensity variation caused by a polydispersion is

given by [61]

$$J(\theta) = K \int_0^\infty i(\theta,\alpha,m) f(\alpha) d\alpha \qquad (31)$$

The use of this result is again limited to dispersions with sufficiently low particle concentrations so that single scattering effects dominate.

PARTICLE SIZE DISTRIBUTION DETERMINATION FROM SCATTERED LIGHT INTENSITY PATTERNS

Particles Large Compared to the Incident Light Wavelength

In principle, the scattered light intensity variation can be used to determine the particle size distribution which produced this variation. Many different investigators have studied this problem for both large and small particle polydispersions. For large particle polydispersions ($\alpha > 20$) and small scattering angles ($\theta \approx \sin\theta$), the Mie scattering function, $i(\theta,\alpha,m)$, can be replaced by the much simpler diffraction theory scattering function, $i_d(\theta,\alpha)$, [49]

$$i_d(\theta,\alpha) = \left[\frac{\alpha J_1(\alpha\theta)}{\theta}\right]^2 \qquad (32)$$

for the polydisperse scattered light intensity distribution given by equation (31). Analytical inversion of the resulting equation to obtain an explicit relationship between the particle size distribution function, $f(\alpha)$, and the scattered light intensity variation yields [64], [65]

$$f(\alpha) = -2\pi\left(\frac{2\pi}{\lambda}\right)^2 \int_0^\infty \frac{d}{d\theta}\left[\frac{\theta^3 J(\theta)}{I_0}\right]\left(\frac{\theta}{\alpha}\right) J_1(\alpha\theta) Y_1(\alpha\theta)\, d\theta \qquad (33)$$

Descriptions of the basic large particle polydispersion size distribution inversion technique and several variations and applications are given in references [32] and [64] - [72] (a summary of the diffraction theory based particle size distribution inversion equations is presented in Appendix B). The large particle techniques could not be used for the nozzle jet flow work because the droplets involved are, in general, smaller than the lower limit for which diffraction theory is applicable.

Particles Small Compared to the Incident Light Wavelength

Several different multiparticle light scattering techniques have been developed for the determination of particle size distributions in polydispersions with diameters less than or nearly equal to the incident light wavelength (e. g., see references [73] - [78]). These methods generally require an *a priori* assumption of the form of the size distribution function, with the experimental data providing the information necessary to determine the distribution function shape parameters. Also, the distribution functions must be monomodal and of narrow width, otherwise the characteristic patterns in the light scattering curves will be masked by the superposition of the patterns characteristic to each of the different sizes. The experimental complexity (large angular and/or many wavelength variations are required) in combination with the aforementioned restrictions limited

the usefulness of these size distribution inversion techniques for the complex nozzle flow conditions.

Because of the geometrical constraints imposed by the nozzle exhaust chamber (only small angle measurements could be reasonably obtained) and the small diameter droplets produced by the two-phase nozzles, it was found that no existing method for size distribution determination could be used. Because of this, a modified optical arrangement was devised and a new procedure was developed for evaluating the particle size distribution using the measured scattered light intensity profile. This new method uses the exact Mie theory in order to be applicable to the small spherical particle range of interest.

PARTICLE SIZE DISTRIBUTION INVERSION METHOD

The numerical inversion of equation (31), a Fredholm integral equation of the first kind, for the size distribution function, $f(\alpha)$, has been studied by several authors (e.g., see references [79] - [82]). The inversion techniques of Phillips [79] and Hanson [80] require small $\Delta\alpha$ steps (consistent with the numerical integration quadrature formula used) and values of the scattered light intensity at relatively large forward scattering angles in order to obtain an accurate result for the inverted size distribution function, $f(\alpha)$. These techniques are relatively insensitive to groups of small particles with comparatively broad size distributions and require high accuracy in the scattered light intensity measurements. These requirements involve undesireably long computer run times and greater experimental complexities for the

nozzle jet flow measurements. The statistical inversion method of Turchin, et. al. [81], as studied in detail by Shifrin, et. al. [82], was of limited value because of its complexity and its insensitivity to the small particle range ($\alpha < 8$) for broad size distributions.

Measured Size Distribution Function Representation by a Series of Narrow Individual Size Distributions

During the investigation of possible size distribution inversion techniques it was determined that a conceptually simple inversion method based upon scattered light intensity profile matching could be developed. This inversion process is accomplished by representing the measured scattered light intensity profile by a summation of contributions from the intensities produced by a series of arbitrarily shaped and suitably spaced narrow individual particle size distribution functions. That is, the measured scattered light intensity, $J_m(\theta)$, is expressed as

$$J_m(\theta) = \sum_{k=1}^{n} C_k J_k(\theta) \tag{34}$$

in which the $J_k(\theta)$ are the intensities calculated from an appropriately spaced series of narrow band particle size distributions, and the C_k's are constants which determines the contribution of each individual distribution. The constants, C_k, are determined by a minimization of the sum of squared error between the measured intensity profile and the calculated intensity profile using the numerical optimization technique

of Powell [83]. Each of the individual intensity profiles, $J_k(\theta)$, are calculated using equation (31) as

$$J_k(\theta) = K \int_0^\infty i(\theta,\alpha,m) f_k(\alpha) d\alpha \tag{35}$$

The individual size distribution functions, $f_k(\alpha)$, and their spacing must be specified appropriately to approximate the size distribution function to be determined. In the limit as $n \to \infty$ in equation (34) and as the individual size distribution functions of equation (35) become delta functions, equation (34) simply reduces to the integral equation (31).

The measured scattered light intensity represented by equation (34), when combined with equation (35), yields

$$J_m(\theta) = K \int_0^\infty i(\theta,\alpha,m) \sum_{k=1}^{n} C_k f_k(\alpha) d\alpha \tag{36}$$

The measured light intensity can also be expressed in terms of the size distribution function of the polydispersion, $f_m(\alpha)$, as

$$J_m(\theta) = K \int_0^\infty i(\theta,\alpha,m) f_m(\alpha) d\alpha \tag{37}$$

By a direct comparison of equations (36) and (37), the measured size distribution function, $f_m(\alpha)$, becomes

$$f_m(\alpha) = \sum_{k=1}^{n} C_k f_k(\alpha) \tag{38}$$

Thus, by the optimized reconstruction of the measured scattered light intensity profile, $J_m(\theta)$, from a series of individual narrow band intensity profiles, $J_k(\theta)$, (calculated using the specified size

distribution functions, $f_k(a)$) the size distribution function of the polydispersion, $f_m(a)$, can be determined using equation (38). Example calculations and experimental measurements using this inversion method are presented in the following sections.

Theoretical Verification of Proposed Size Distribution Inversion Method

Several numerical experiments were performed to investigate the applicability of the scattered light intensity profile matching procedure for the inversion of particle size distribution functions. The numerical experiments included example inversions of three different size distribution functions; 1) a narrow monomodal size distribution, 2) a broad monomodal size distribution and 3) a bimodal size distribution. Particular attention was given to both the maximum forward scattering angle required and the number of narrow band size distributions necessary for a given size distribution inversion accuracy. Calculations were performed for which a monomodal size distribution function was specified, a scattered light intensity profile was calculated with equation (31) using this size distribution function and the Mie scattering function (the numerical quadrature used was Simpson's 1/3 rule), and then the optimization technique was applied to determine the strengths of the series of assumed narrow band size distributions. Any arbitrarily shaped function could conceivably be used to form the series of narrow band size distribution functions. However, it was found that smooth functions provided the most accurate size distribution function inversions.

The process for determining an appropriate group of narrow band size distribution functions is basically an iterative one. The first step is to calculate scattered light intensity profiles for several assumed monomodal size distribution functions. Comparison of these calculated intensity distributions with the true intensity profile provides a guide for the particle size range that must be included by the narrow band size distribution function series. An assumed series of narrow band size distribution functions is then chosen, and the true intensity profile reconstructed with the optimization procedure. If acceptable agreement between the optimized and the true intensity profiles is not obtained after this reconstruction, the series of narrow band size distribution functions must be modified. Continuation of this procedure leads to a final series of narrow band size distributions which, when their respective intensity distributions are combined using the optimization procedure, yields acceptable agreement with the known intensity distribution.

It was found through these calculations that for the small particle range of interest, the inverted size distribution function was very nearly the same as the specified distribution function, irrespective of the initial solution guess (an initial guess for the C_k's is required to start the optimization procedure). It was also determined that constraints has to be applied to the optimization calculation to preclude any large negative C_k's that could result in negative values for $f_m(a)$. Similar results should be possible for large particle polydispersions, but due to the increased calculational time required

for the Mie scattering functions, the optimization technique becomes inefficient and an inversion method based upon diffraction theory would be better utilized.

Narrow Monomodal Particle Size Distribution Function Inversion - To demonstrate the iterative process required for the determination of the series of narrow band distribution functions, a narrow monomodal size distribution function was chosen and its related scattered light intensity profile calculated using equation (31). The monomodal size distribution function was formed using the upper limit distribution function (ULDF), given by the equation [47], [84]

$$f(\alpha) = \frac{C' \exp(-\{\delta \ln[a\alpha/(\alpha_\infty - \alpha)]\}^2)}{\alpha^4(\alpha_\infty - \alpha)} \tag{39}$$

where C' is defined for normalization such that†

$$\int_0^\infty f(\alpha)d\alpha = 1 \tag{40}$$

The shape of a given ULDF is difficult to specify using the shape parameters a and δ of equation (39) because of their geometrically indirect interpretations. Because of this, it is more useful to eliminate them in favor of two other variables with more direct geometrical interpretations. Two such variables are the modal size parameter, $\bar{\alpha}$, and the normalized size distribution width, Q_{ULDF}.

† - The use of the size distribution functions given by equations (39) and (44) with the definition of C' given by equation (40), in conjunction with the light scattering integral equation, equation (31), is equivalent to the specification of N = 1 in equation (30).

Designating the larger and smaller half peak size parameters of the distribution function as $\alpha_{+1/2}$ and $\alpha_{-1/2}$, respectively, the normalized function width, Q_{ULDF}, is defined as

$$Q_{ULDF} = (\alpha_{+1/2} - \alpha_{-1/2})/\bar{\alpha} \tag{41}$$

Solving equation (39) for the modal size parameter, $\bar{\alpha}$, yields the shape parameter, a, in terms of the shape parameter, δ, the normalized half width, Q_{ULDF}, and the half peak size parameters, $\alpha_{\pm 1/2}$,

$$a = (\alpha_\infty/\bar{\alpha} - 1)\ \exp[(1/\delta^2)(2.5\bar{\alpha}/\alpha_\infty - 2)] \tag{42}$$

The function half width size parameters, $\alpha_{\pm 1/2}$, are related to the shape parameters, a and δ, by the transcendental equation

$$(\alpha_{\pm 1/2}/\bar{\alpha})^4(\alpha_\infty - \alpha_{\pm 1/2})/(\alpha_\infty - \bar{\alpha}) - 2\ \exp[-\delta^2(\{\ \ln[a\alpha_{\pm 1/2}/(\alpha_\infty - \alpha_{\pm 1/2})]\}^2 - \{\ \ln[a\bar{\alpha}/(\alpha_\infty - \bar{\alpha})]\}^2)] = 0 \tag{43}$$

Thus, by the specification of the normalized function width, Q_{ULDF}, the maximum size parameter, α_∞, and the modal size parameter, $\bar{\alpha}$, the ULDF shape parameters a and δ and the resulting size distribution function curve can be determined by simultaneously solving equations (41) - (43).

The narrow monomodal size distribution function chosen for the theoretical size distribution inversion method verification was formed using equation (39) with $\bar{\alpha} = 7.5$, $Q_{ULDF} = 1.0$ and $\alpha_\infty = 20$. Using the light intensity profile calculated for this size distribution function as experimental data, the series of narrow band distribution functions

must now be determined for the size distribution function inversion process. To find the modal size parameter range of interest for the inversion process, several size distribution functions were assumed and their intensity profiles calculated. Two of these intensity profiles (upper and lower curves) are presented in Figure 21, along with the intensity profile calculated for the narrow monomodal ULDF (center curve) for comparison. All profiles have been normalized to 1.0 at $\theta = 0$ degrees for this comparison. The scattered light intensity profiles for the assumed distribution functions were calculated using exponential size distribution functions given by [61]

$$f(\alpha) = C' \ (\alpha - \alpha_o) \ \exp\{-[(\alpha - \alpha_o)/S]^3\} \qquad (44)$$

for $\alpha > \alpha_o$. The normalization constant C' is determined using equation (40), and the shape parameter, S, is defined by

$$S = (\bar{\alpha} - \alpha_o)3^{1/3} \qquad (45)$$

The exponential size distribution functions were chosen for their smoothness and because of the simplicity in specifying both the modal size and the amount of overlap between successive functions for use in the series of narrow band size distribution functions.

The upper intensity profile of Figure 21 was calculated using an exponential size distribution function with $\bar{\alpha} = 5$ and $\alpha_o = 10^{-3}$, and the lower intensity profile was calculated using an exponential distribution function with $\bar{\alpha} = 15$ and $\alpha_o = 10$. It can be seen that the modal size parameter of the lower intensity profile is larger than that of the

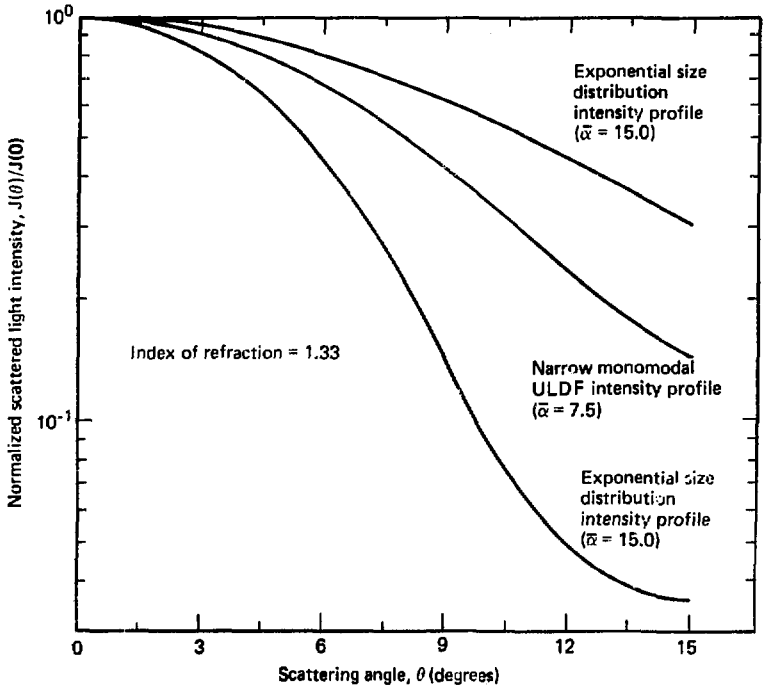

Figure 21. - Normalized scattered light intensity profile calculated *using the narrow monomodal size distribution function (center curve)* compared with the normalized intensity profiles calculated using two different exponential monomodal size distribution functions (top and bottom curves).

narrow monomodal ULDF. This is because the larger the particles, the higher the intensity gradient, $dJ(\theta)/d\theta$, at small angles, and conversely. Similarly, it can be seen that the slope of the upper intensity profile is less than that of the intensity profile calculated for the narrow monomodal ULDF. These comparisons indicate that the modal size parameter of the monomodal ULDF is greater than $\bar{a} = 5$ but less than $\bar{a} = 15$. From these comparisons, the series of narrow band size distribution functions of Figure 22 were chosen. The narrow monomodal ULDF is also shown in Figure 22. The five narrow band distribution functions were chosen to completely span the approximate range of particle sizes indicated by the true scattered light intensity distribution and to allow a function overlap near one half to provide for the necessary superposition to occur when using the optimization procedure.

Figure 23 presents both the input scattered light intensity profile calculated using the monomodal ULDF and the resulting optimization reconstructed scattered light intensity profile using the narrow band size distribution functions shown in Figure 22. The optimization procedure was used to match the true intensity profile at 0.5 degree intervals for this calculation. The scattering angle range, 1 - 14 degrees, was chosen to be consistant with the experimental capability. However, calculations indicate that a scattering angle range as small as 1 - 5 degrees can be used to obtain good size distribution inversion accuracy for this particle size spectrum. The agreement between the two

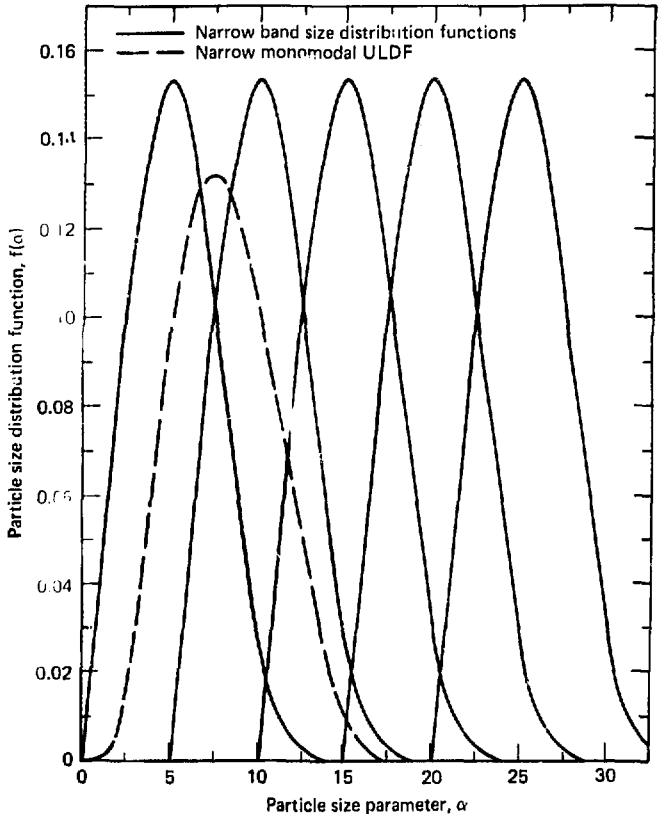

Figure 22. - Narrow band and narrow monomodal size distribution functions.

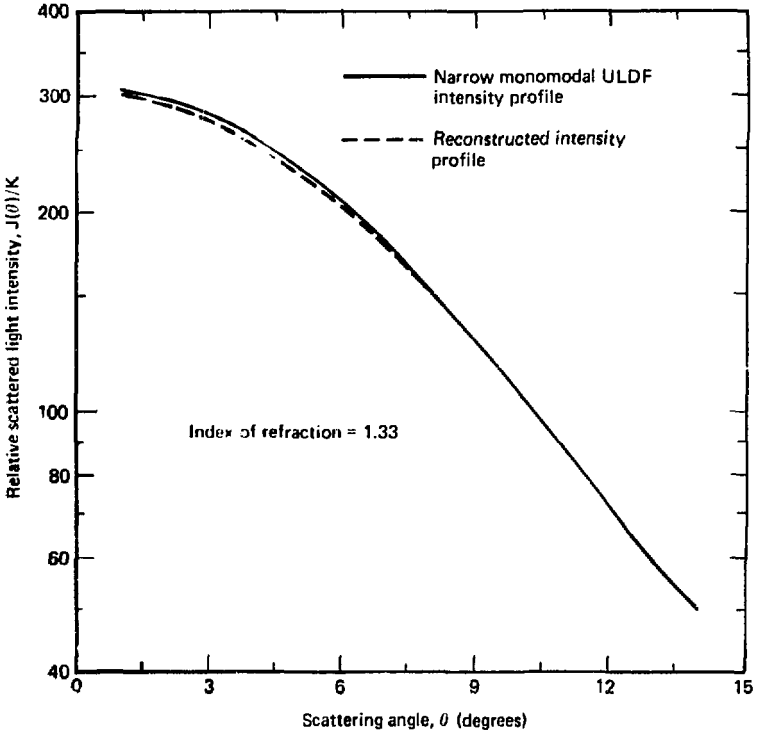

Figure 23. - Input narrow monomodal and narrow band reconstructed size distribution scattered light intensity profile comparison.

curves is excellent and can be used as a measure of the size distribution inversion accuracy.

Figure 24 presents the narrow monomodal ULDF, the inverted size distribution function and their respective calculated mass fractions (the determination of which is very important for impulse turbine blade flow passage design). The mass fraction is defined by the equation

$$\text{mass fraction} = \frac{\int_0^a a^3 f(a)da}{\int_0^\infty a^3 f(a)da} \qquad (46)$$

Also presented in this figure are data comparing the mean particle size parameters, the Sauter mean particle size parameters and the mass-mean particle size parameters of the monomodal ULDF and the inverted particle size distribution functions. The mean particle size parameter is defined as

$$a_{10} = \frac{\int_0^\infty af(a)da}{\int_0^\infty f(a)da} \qquad (47)$$

and the Sauter mean particle size parameter is given by

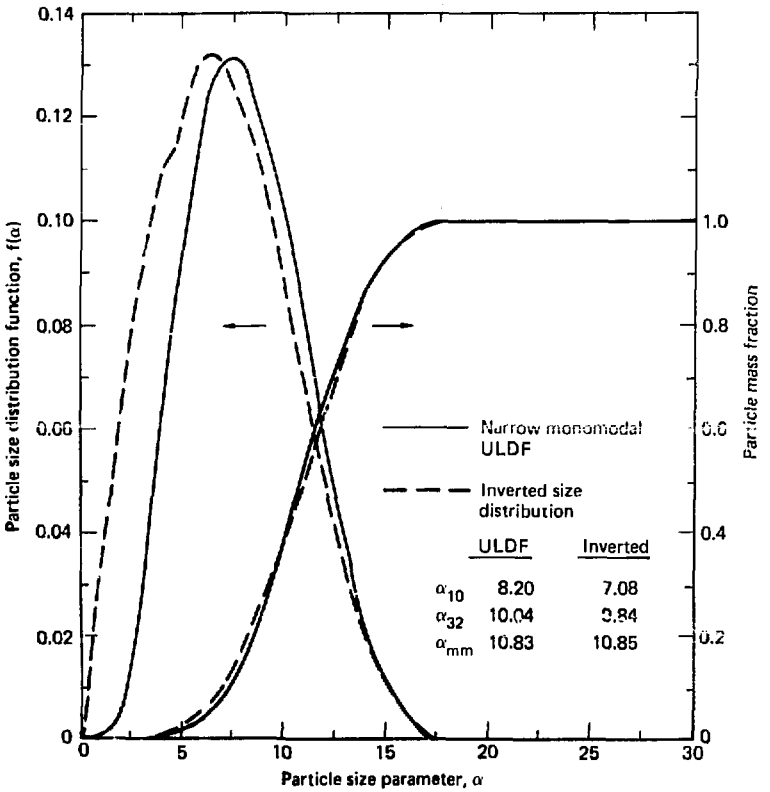

Figure 24. - Comparison of the narrow monomodal and inverted size distribution functions and their respective mass fractions.

$$a_{32} = \frac{\int_0^{\infty} a^3 f(a)da}{\int_0^{\infty} a^2 f(a)da} \tag{48}$$

The mass-mean particle size parameter, a_{mm}, is defined such that

$$\frac{\int_0^{a_{mm}} a^3 f(a)da}{\int_0^{\infty} a^3 f(a)da} = 0.5 \tag{49}$$

From these comparisons, the accuracy and uniqueness of the constrained optimization size distribution inversion method can be seen.

If the input narrow monomodal ULDF and the reconstructed scattered light intensity profiles of Figure 23 had been significantly different, the size distribution inversion accuracy would have been poor and a different set of narrow band distribution functions would have been necessary (based upon the results of the first set) to provide a better inversion accuracy. This iterative process for the determination of the narrow band size distribution functions must be continued until the reconstructed scattered light intensity profile matches the true intensity profile within acceptable accuracy limits. The iteration procedure used to obtain the series of narrow band size distribution functions generally converges within one or two different series assumptions.

Broad Monomodal Particle Size Distribution Function Inversion - To further verify the usefulness and accuracy of the narrow band size distribution inversion method, a broad monomodal particle size distribution was chosen and its related scattered light intensity pattern was calculated to be used as though it were experimental data. The particle size distribution was formed by using a ULDF with $\bar{a} = 22$, $Q_{ULDF} = 0.75$ and $\alpha_{\infty} = 50$.

The inversion of this distribution function follows the same process as that which was used for the narrow particle size distribution function inversion. The scattered light intensity profiles for several different assumed particle size distributions were calculated and compared with the intensity profile calculated using the broad monomodal size distribution. This comparison was made to determine the appropriate range in the modal size parameter that must be covered by the narrow band size distribution functions. Based upon this comparison, the series of narrow band size distribution functions shown in Figure 25 was chosen. The broad monomodal size distribution function is also shown in this figure for comparison.

The intensity profile calculated using the broad monomodal size distribution and the intensity profile resulting from the narrow band size distribution optimization process (intensity profiles matched at 0.5 degree intervals) is shown in Figure 26. The scattering angle range, 1 - 10 degrees, was chosen to be consistant with the experimental capability. From the agreement between these intensity profiles it

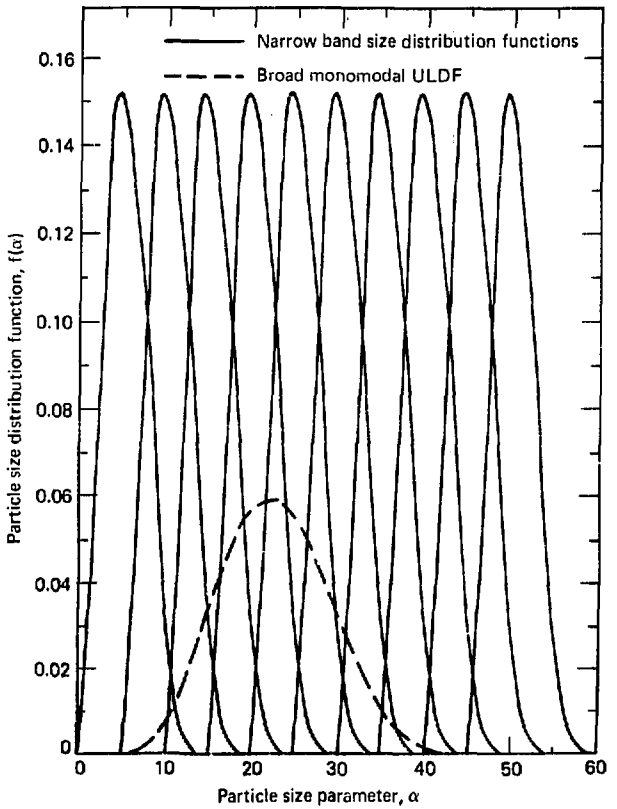

Figure 25. - Narrow band and broad monomodal size distribution functions.

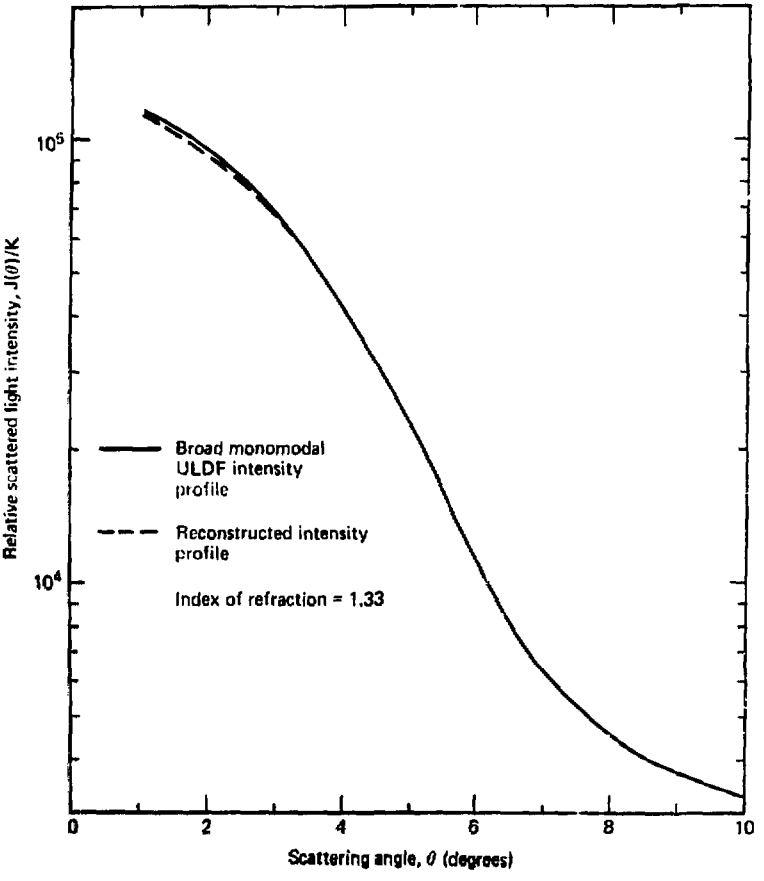

Figure 26. - Input broad monomodal and narrow band reconstructed size distribution scattered light intensity profile comparison.

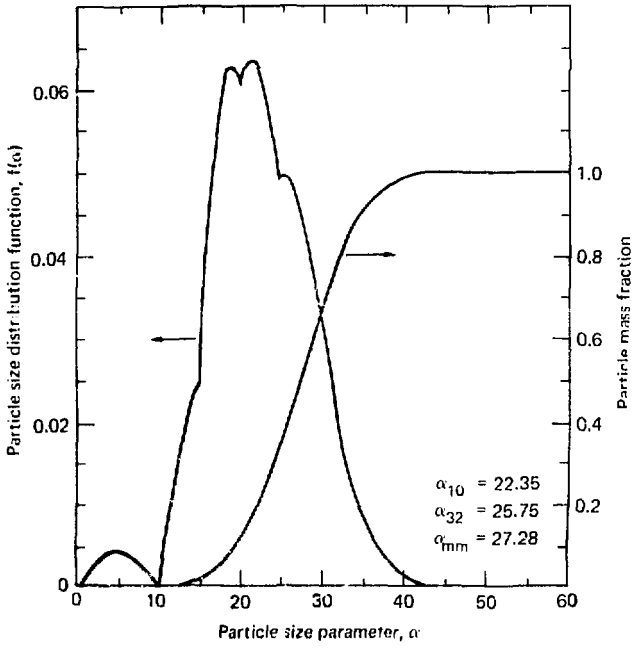

Figure 27. Inverted broad monomodal size distribution function and its mass fraction profile.

appears that there is good accuracy in the particle size distribution inversion. However, the inverted size distribution function and the resulting mass fraction, shown in Figure 27, indicates that a second assumption for the series of narrow band size distribution functions is needed.

The second assumption for the series of narrow band size distribution functions is shown in Figure 28. The broad monomodal particle size distribution function is also shown in the figure for comparison. The narrow band size distribution functions were broadened to allow more smoothing of the inverted size distribution function and to utilize fewer functions for the intensity profile matching process.

The intensity profile calculated using the broad monomodal size distribution and the intensity profile resulting from the optimization process using the second assumed series of narrow band size distributions is shown in Figure 29. The agreement is such that the two intensity profiles are nearly identical. This indicates that the inversion of the broad monomodal size distribution is accurate.

Figure 30 presents the broad monomodal size distribution function, the inverted size distribution function and their respective mass fractions. Also presented are the different mean particle size parameters for the broad monomodal and inverted size distribution functions. These comparisons confirm the excellent inversion accuracy indicated by the intensity profile matching procedure. The much better agreement in this case suggests that the best inversion accuracy is

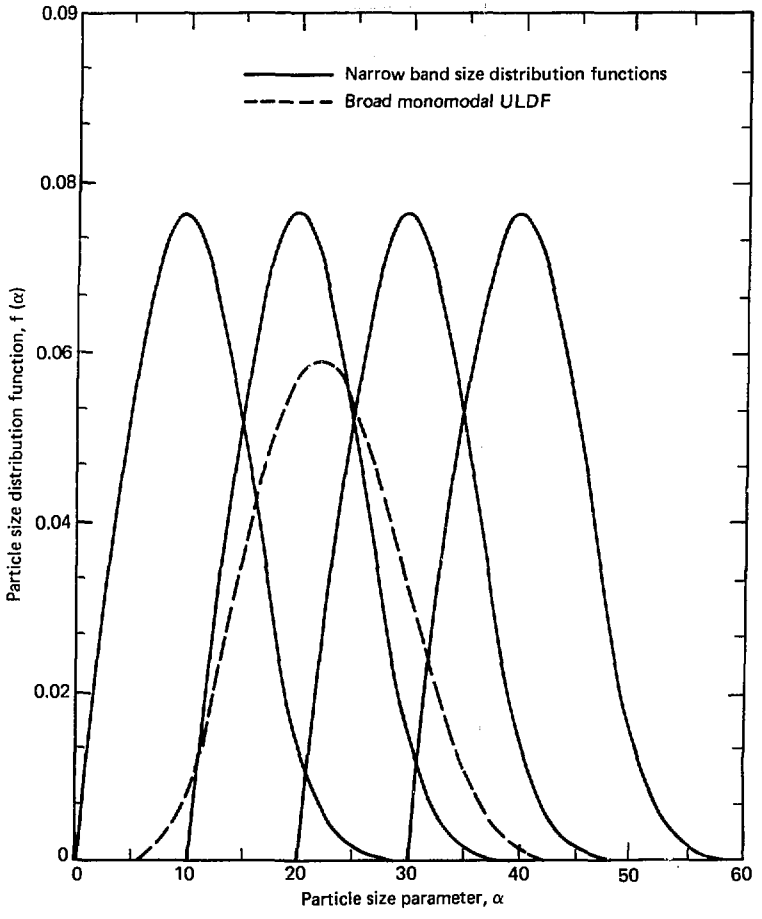

Figure 28. - Narrow band (second assumed series) and broad monomodal size distribution functions.

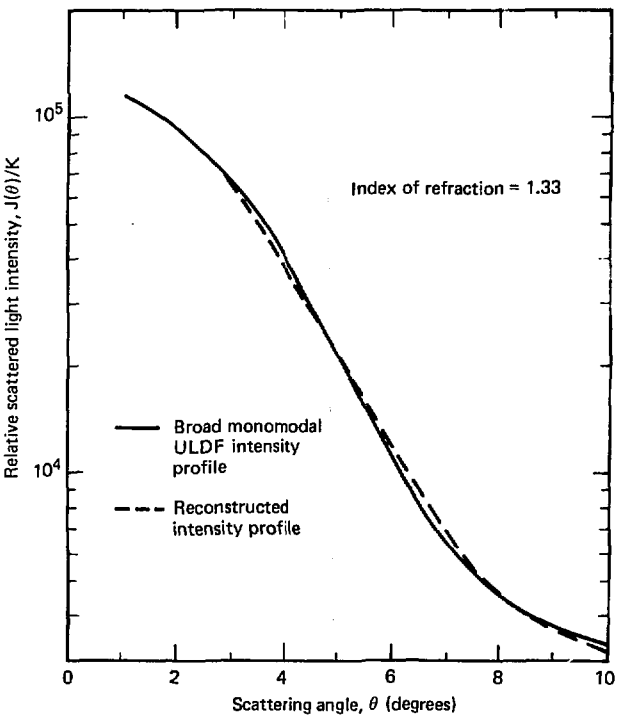

Figure 29. - Input broad monomodal and narrow band resonstructed (using the second assumed series) size distribution scattered light intensity profile comparison.

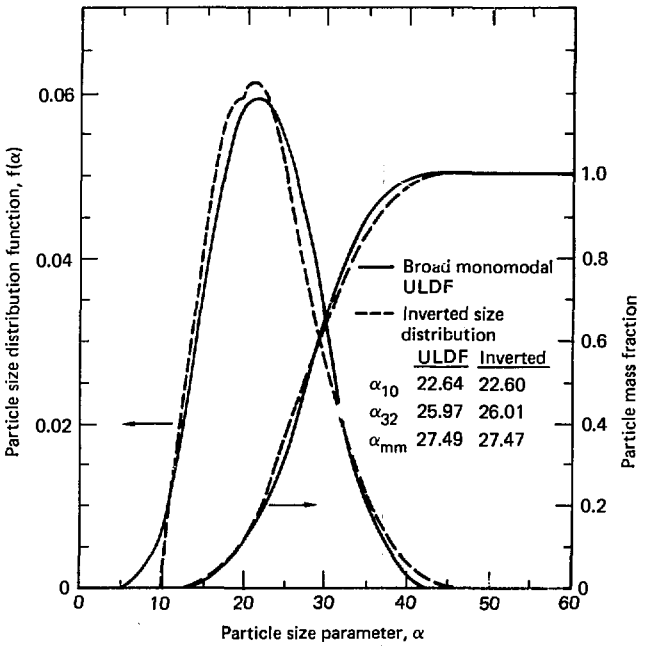

Figure 30. - Comparison of the broad monomodal and inverted size distribution functions and their respective mass fractions.

obtained when the true size distribution is spanned by approximately four of the narrow band size distribution functions (compare Figures 25 and 28). Also, it is interesting to note that even with the poor size distribution inversion that occurred for the first series of assumed narrow band size distributions (compare Figures 27 and 30) the mean size parameters and the mass fraction, both determined from an integration of the inverted size distribution function, were accurate. This has also been found to be true for other broad size distribution function inversions, and it indicates that the mean size parameters can be determined accurately without the need for an exact inversion of the size distribution function.

Bimodal Particle Size Distribution Function Inversion - The theoretical inversion of a bimodal particle size distribution using the narrow band size distribution intensity profile matching method was also accomplished to more fully demonstrate the applicability of this method. The bimodal size distribution function was formed by the addition of a ULDF with $\bar{\alpha} = 5$, $Q_{ULDF} = 1.0$ and $\alpha_{\infty} = 50$ to a second ULDF with $\bar{\alpha} = 25$, $Q_{ULDF} = 0.5$ and $\alpha_{\infty} = 50$. The second ULDF was multiplied by 6.0 to amplify the relative magnitude between the two functions.

The bimodal size distribution function and the assumed narrow band distribution functions are shown in Figure 31 for comparison. The narrow band size distribution functions were chosen in a manner similar to that which was used previously for the monomodal size distribution function inversions. The scattered light intensity profile for the

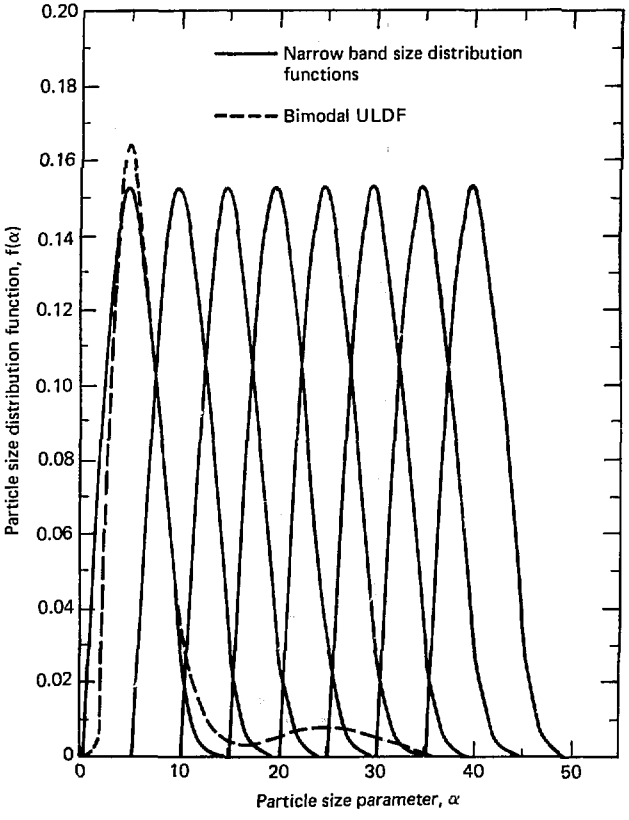

Figure 31. - Narrow band and bimodal size distribution functions.

bimodal size distribution function was calculated using equation (31) to be used as though it were experimental data. Then, the scattered light intensity profiles of several assumed size distributions were calculated for comparison with this intensity profile to determine the modal size parameter range that must be covered by the narrow band size distribution functions.

Figure 32 presents the scattered light intensity profile calculated using the bimodal size distribution function and the resulting optimization reconstructed scattered light intensity profile using the narrow band size distribution functions. The optimization procedure was used to match the true intensity profile at 0.5 degree intervals for this reconstruction. The scattering angle range, 1 - 14 degrees, was chosen to be consistant with the experimental capability. However, calculations indicate that a scattering angle range as small as 1 - 10 degrees could be used to obtain good size distribution inversion accuracy for this particle size spectrum. Scattered light intensity information concerning the small size spectrum of the bimodal size distribution is masked by that of the large size spectrum of the distribution when the scattering angle range is limited to < 10 degrees. Good size distribution inversion accuracy is indicated by the excellent agreement between the true and reconstructed scattered light intensity profiles shown in Figure 32.

Figure 33 presents the bimodal size distribution function, the inverted size distribution function and their respective mass fractions.

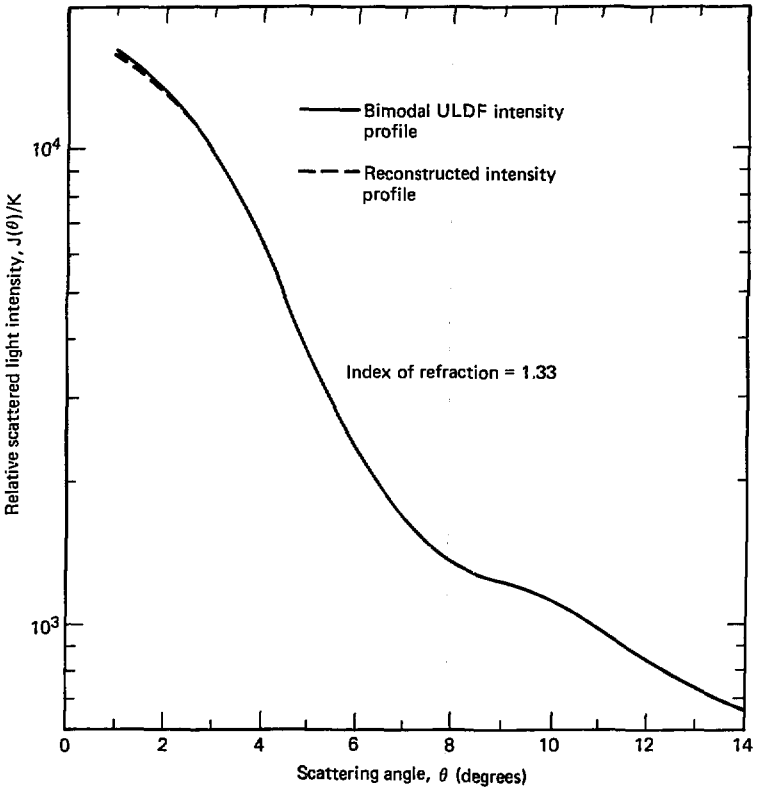

Figure 32. - Input bimodal and narrow band reconstructed size distribution scattered light intensity profile comparison.

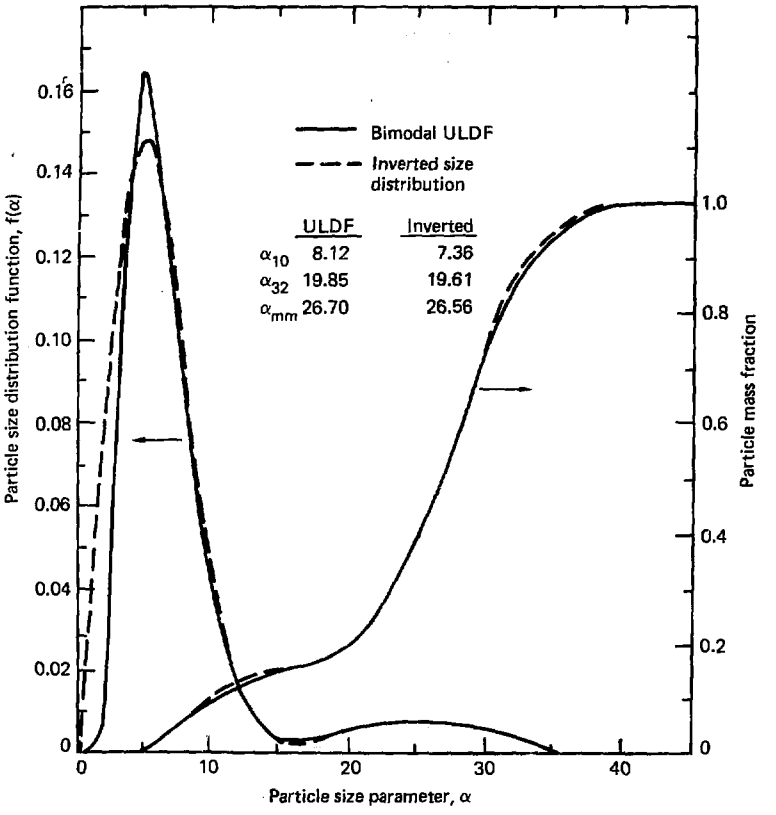

Figure 33. - Comparison of the bimodal and inverted size distribution functions and their respective mass fractions.

Also presented are the different mean particle size parameters for the bimodal and inverted size distribution functions. As with the monomodal size distribution inversions, the agreement between the input and inverted functions is excellent. The capability for multimodal size distribution function inversions is very important to the understanding of two-phase nozzle flows, since flow channeling of the droplet phase and boundary layer - liquid film shearing action at the nozzle wall appears to cause complex particle size distribution functions (see the experimental work presented in references [71], [85]).

EXPERIMENTAL SCATTERED LIGHT MEASUREMENT SYSTEM

Optical System Arrangement

The purpose of the experimental light scattering system was to measure the scattered light intensity, $J_m(\theta)$, as a function of the scattering angle for the determination of the droplet size distribution in the two-phase, liquid-dominated nozzle jet flow. This measurement was accomplished using the optical arrangement shown schematically in Figure 34. A photograph of the beam forming and film calibration optics is shown in Figure 35. Photographs of the open jet two-phase nozzle installation as seen from the side and top of the nozzle exhaust chamber are shown in Figures 18 and 19, respectively. A photograph of the scattered light collecting lens and calibrated film arrangement installed at the nozzle test chamber is shown in Figure 36. These photographs clearly illustrate the geometrical complexity involved with

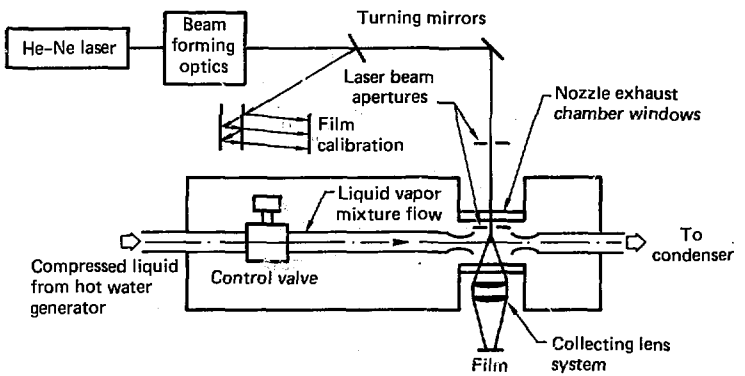

Figure 34. - Schematic of the optical system used for the scattered light intensity profile measurements.

Figure 35. – Photograph of the beam forming and calibration optics for the experimental scattered light measurement system.

Figure 36. - Photograph of the scattered light collecting lens and calibrated film arrangement installed at the nozzle test chamber.

the installation and operation of the optical system for the two-phase nozzle flow experiments.

As seen in Figures 34 - 36, the scattered light intensity measurement is based upon the use of a calibrated film for the scattered light detection. This provides a very simple arrangement for experimentally obtaining high spatial (angular) resolution scattered light information, but it requires a complex data analysis procedure. A discussion of the film calibration and the data analysis procedure is presented in Appendix C.

As shown in Figure 34, the light from a He-Ne laser (laser output power of 5 mW of horizontally polarized light at λ = 632.8 nm) is shuttered and attenuated (using crossed polarizers to allow variable attenuation) appropriately for the film sensitivity and apertured to eliminate the scattered light from the optical components before traversing the nozzle jet flow. Kodak† linagraph shellburst 2474 film was used because of its red light sensitivity and its 10.2 X 12.7 cm format. The light scattered from the droplets in the flow is collected with a lens combination and directed to the film plane located at the focal length. The collecting lens system for the nozzle jet flow measurements was designed after the arrangement used by Chin, et. al. [64]. However, modification was necessary to eliminate spherical aberration problems that are encountered for larger scattering

† - Reference to a company or product name does not imply recommendation of the product by the University of California or the U. S. Department of Energy to the exclusion of others that may be suitable.

angles with finite measuring volumes. The aberration problems were essentially eliminated by using a combination of two 7 cm diameter, 60 cm focal length plano-convex lenses in series to form an effective 30 cm focal length system. This lens system was located approximately 10 cm from the nozzle jet flow and apertured to 5.1 cm in diameter to allow a near 14 degree collection half angle. A discussion of the lens system design considerations is presented in Appendix D.

Each individual piece of film was calibrated to ensure high measurement accuracy because of possible variations in the emulsions and development processes. The film was calibrated using a partially transmitting mirror combination which forms a series of light beams of differing, but known relative energy (see Appendix C). The portion of the film exposed by these light beams is scanned using a microdensitometer to provide the necessary film density – energy density relationship for the film calibration. The exposure due to the collected scattered light is also scanned using the microdensitometer, and the resulting film density information is converted to energy density using the film calibration information in a adaptation of the numerical analysis procedure developed by Weaver, et. al. [86]. The resulting energy density profile is a measure of the scattered light intensity variation and can be used directly in the droplet size distribution inversion procedure unless the absolute number of droplets traversed by the light beam need be known (see Appendix D). In this way, the inverted size distribution function will be identical to the

absolute size distribution function, except for the difference of a constant multiplier.

The scattered light intensity measurements were corrected for extraneous scattered light (e. g., due to optical components, jet flow spray, optical winows, etc.) by subtracting the measured extraneous scattered light intensity profile from the measured nozzle jet flow scattered light profile. The extraneous scattered light was determined while operating the nozzle by measuring the scattered light from a laser beam that was passed above the nozzle jet flow. This correction was, in general, very small and was largest at small scattering angles.

Verification of Optical Arrangement and Data Determination Procedure

An experimental verification of the optical arrangement and the data determination procedure was accomplished by substituting a glass beads-in-water polydispersion in place of the nozzle flow of Figure 34. The glass bead polydispersion had a modal diameter near 15 μm. The polypolydispersion was continually agitated using a magnetic stirring arrangement to maintain constant glass bead dispersion uniformity.

The scattered light intensity profiles for this polydispersion were determined according to the previous description, except that the collecting lens to polydispersion distance was increased due to the small scattering angle required. Because of the large modal particle diameter and the broad particle size distribution, the size distribution function was determined using the large particle inversion method (see

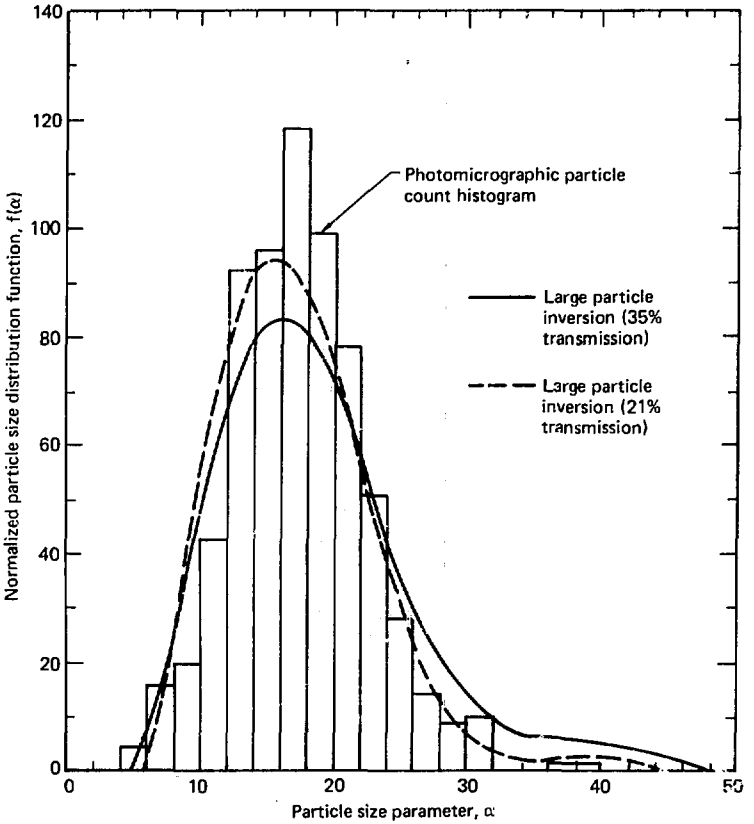

Figure 37. - Comparison of the size distribution functions obtained using the large particle inversion technique with a photomicrographic particle count for a glass beads-in-water polydispersion.

equation (33) and Appendix B). The inverted particle size distributions obtained for light transmissions of 35% and 21% are compared to a photomicrographic particle count (~ 700 particles counted) in Figure 37. The light transmission of the dispersion was maintained > 20% to ensure dominant single scattering effects. The two particle size distributions and the particle count histogram were normalized to equivalent areas under each curve for the comparison. The comparatively good agreement between the inverted particle size distribution functions and the particle count histogram of Figure 37 demonstrates the applicability of the experimental optical arrangement and the data determination procedure to particle size distribution measurements.

EXPERIMENTAL NOZZLE JET FLOW DROPLET SIZE DISTRIBUTION MEASUREMENTS

Results for Nozzle Numbers 2 - 4

Light scattering measurements were made using nozzle numbers 2 - 4 to determine the effect of the nozzle throat radius of curvature on the droplet size distribution in the high-velocity nozzle jet flow. In order to obtain the > 20% light transmission required for the light scattering measurements, the nozzles were operated at inlet pressures of 0.7 MPa (100 psia) and 1.0 MPa (150 psia) at the near ideal expansion exhaust pressures of 13.8 kPa (2.0 psia) and 20.7 kPa (3.0 psia), respectively. The enthalpy of the two-phase mixture entering the nozzles was maintained near 1.16 MJ/kg (500 Btu/lbm) for experimental convenience and to be consistant with geothermal wellhead conditions.

Light scattering data was taken at the nozzle jet centerline and at a position located 2.4 cm vertically from the jet centerline to determine any droplet size distribution changes occurring between these spatial locations. The axial measurement location was approximately 1.0 cm from the nozzle exit for all light scattering measurements.

Figure 38 presents the measured relative scattered light intensity profiles for each of the different nozzles (nozzle numbers 2 - 4) and for inlet and exhaust pressures near 0.7 MPa (100 psia) and 13.8 kPa (2.0 psia), respectively. Similarly, the measured scattered light intensity profiles for inlet and exhaust pressures near 1.0 MPa (150 psia) and 20.7 kPa (3.0 psia), respectively, are shown in Figure 39. For each different nozzle, the upper intensity profile corresponds to the nozzle jet centerline measurement position, and the lower intensity profile was determined at a position located 2.4 cm vertically from the nozzle jet centerline. Each of the intensity profiles has been multiplied by a different arbitrary constant for this presentation. Table 2 lists the nozzle operating conditions at which each of the scattered light intensity profiles were measured. The measured light transmission for each intensity profile is also given in Table 2.

It can be seen from Figure 38 that the scattered light intensity profiles indicate that as the nozzle throat radius of curvature increases, the droplet size in the nozzle jet flow also increases. This can be seen by comparing the slopes of the intensity profiles at small

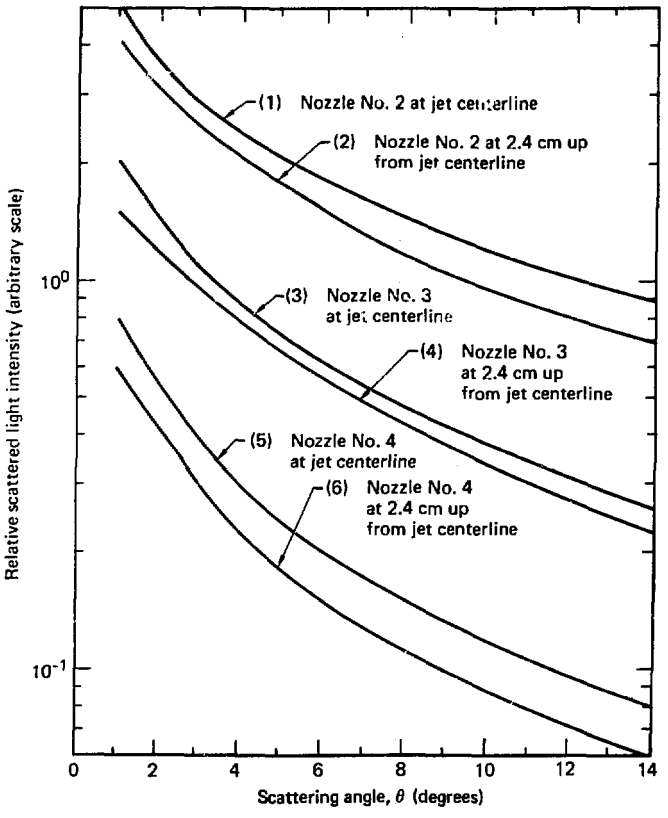

Figure 38. - Measured relative scattered light intensity profiles for nozzle numbers 2 - 4. The nozzle operating conditions (inlet pressures near 0.7 MPa (100 psia) and exhaust pressures near 13.8 kPa (2.0 psia)) corresponding to the different scattered light intensity profiles are listed in Table 2.

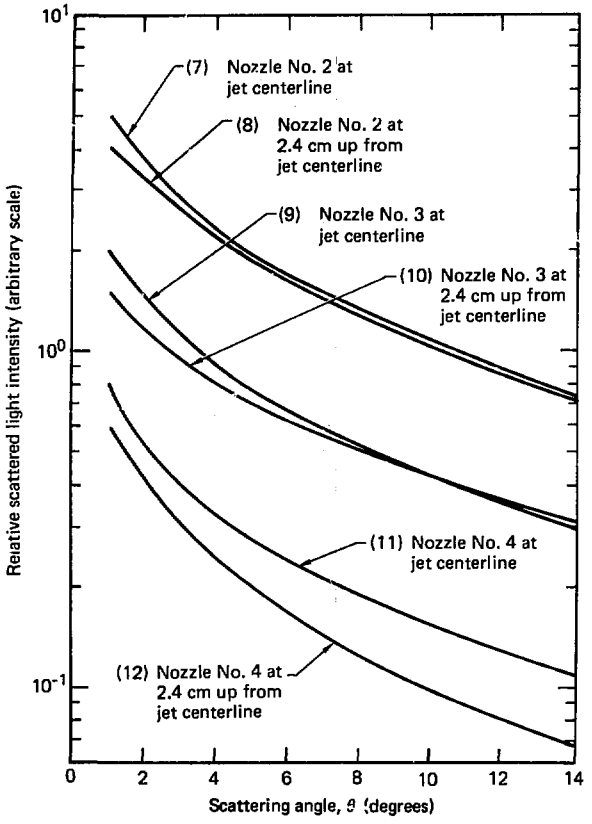

Figure 39. - Measured relative scattered light intensity profiles for nozzle numbers 2 - 4. The nozzle operating conditions (inlet pressures near 1.0 MPa (150 psia) and exhaust pressures near 20.7 kPa (3.0 psia)) corresponding to the different scattered light intensity profiles are listed in Table 2.

Table 2. - Nozzle operating conditions corresponding to the scattered light intensity profiles of Figures 38 and 39.

Profile No. (Nozzle No.)	Inlet Pressure, MPa (psia)	Inlet Enthalpy, MJ/kg (Btu/lbm)	Exhaust Pressure, kPa (psia)	Light Transmission (λ = 632.8 nm)
1 (2)	0.75 (109)	1.17 (501)	15.2 (2.2)	0.31
2 (2)	0.70 (102)	1.16 (498)	15.2 (2.2)	0.29
3 (3)	0.80 (116)	1.21 (518)	16.5 (2.4)	0.30
4 (3)	0.74 (108)	1.17 (503)	13.1 (1.9)	0.35
5 (4)	0.70 (102)	1.14 (489)	14.5 (2.1)	0.27
6 (4)	0.77 (111)	1.15 (494)	14.5 (2.1)	0.32
7 (2)	1.04 (151)	1.17 (501)	17.9 (2.6)	0.19
8 (2)	1.03 (150)	1.19 (510)	22.8 (3.3)	0.20
9 (3)	1.05 (153)	1.17 (504)	22.1 (3.2)	0.20
10 (3)	1.05 (152)	1.20 (516)	21.4 (3.1)	0.22
11 (4)	1.08 (156)	1.16 (499)	20.0 (2.9)	0.20
12 (4)	1.13 (164)	1.17 (504)	19.3 (2.8)	0.22

angles. However, the intensity profiles shown in Figure 39 do not show this same trend. This indicates that the droplet size changes due to nozzle throat contour modifications are very small and that the accuracy of the nozzle jet flow scattered light intensity measurements is such that these small diameter changes cannot be resolved. Further light scattering measurements have confirmed this trend for the range of nozzle conditions studied.

The inversion of the nozzle jet flow droplet size distribution functions from the scattered light intensity profiles were accomplished in a manner similar to that described previously for the theoretical size distribution inversions. The scattered light intnesity profiles for several assumed monomodal size distribution functions were

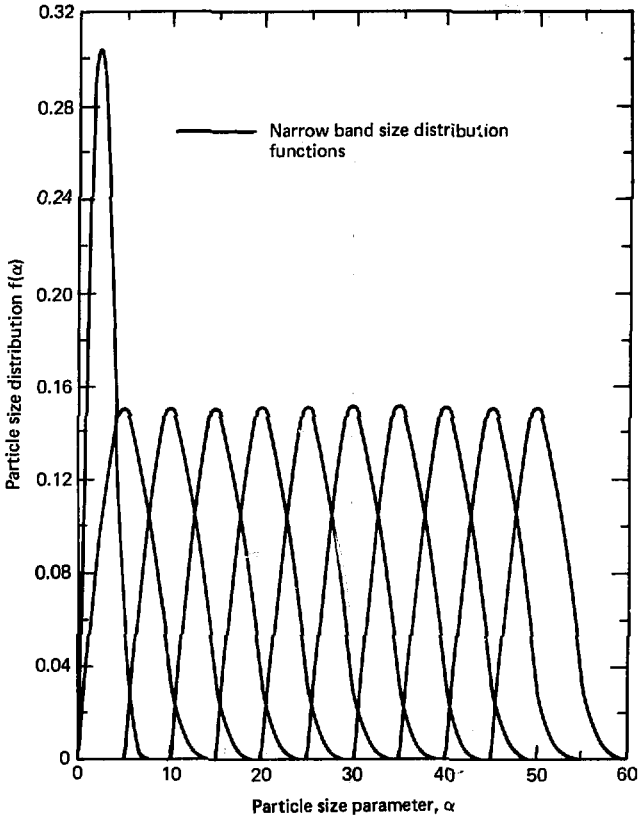

Figure 40. – Assumed series of narrow band size distribution functions used for the two-phase nozzle jet flow experimental droplet size distribution function inversions.

calculated and compared with the experimental intensity profiles. From this comparison, the series of narrow band size distribution functions shown in Figure 40 were chosen. These functions were specified to cover a size parameter range from 0 to nearly 60 to include all the possible droplet diameters that were indicated by the measured intensity profiles.

The measured and optimization reconstructed intensity profiles for the 0.7 MPa (100 psia) nozzle inlet pressure experiments are shown in Figure 41, and those for the 1.0 MPa (150 psia) nozzle inlet pressure are shown in Figure 42. Because of the near equivalency between the intensity profiles determined at the nozzle jet centerline and at the position 2.4 cm vertical from the nozzle jet centerline, only the jet centerline intensity profiles were reconstructed for the droplet size distribution inversion process. The optimization procedure was used to match the measured intensity profiles at 0.5 degree intervals for these reconstructions. The agreement between the measured and reconstructed intensity profiles indicates good inversion accuracy for the droplet size distributions.

Figures 43 and 44 present the droplet size distributions and mass fractions (see equation (46)) measured at the nozzle jet centerline for the 0.7 MPa (100 psia) and 1.0 MPa (150 psia) inlet pressures, respectively. The pertinent average droplet size parameters for these droplet size distributions are listed in Table 3. The waviness of the mass fraction curves is caused by a combination of the multimodal nature

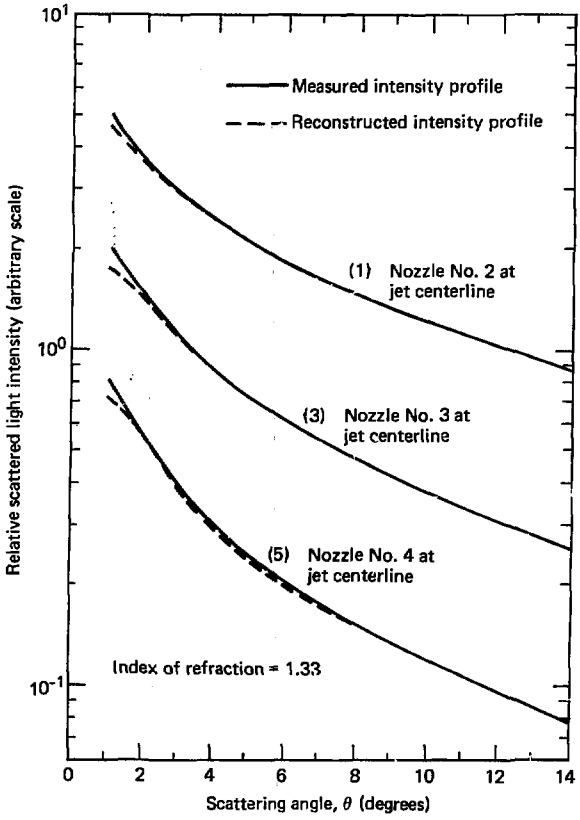

Figure 41. – Comparison of the measured and reconstructed relative scattered light intensity profiles for the two-phase nozzle jet flow experiments. The intensity profiles presented were determined at the nozzle jet centerline for a nozzle inlet pressure near 0.7 MPa (100 psia). The nozzle operating conditions are listed in Table 2.

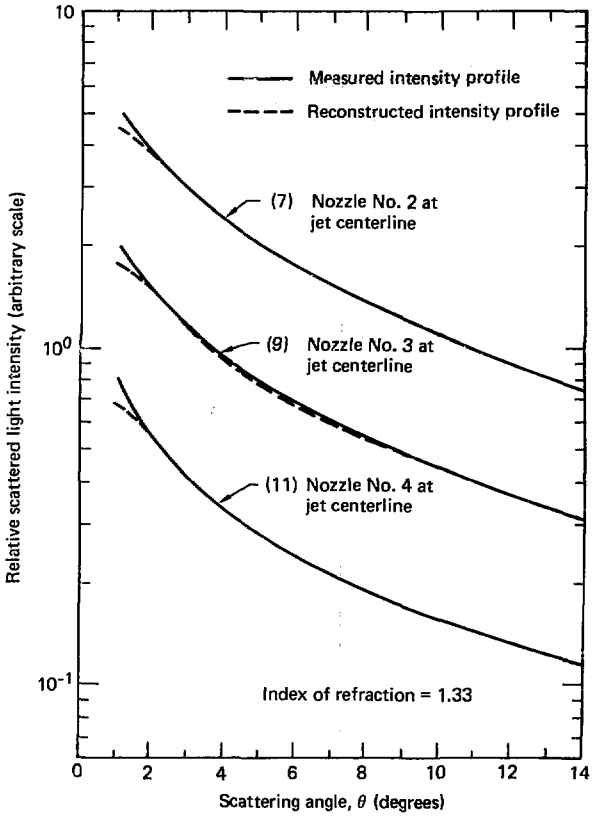

Figure 42. – Comparison of the measured and reconstructed relative scattered light intensity profiles for the two-phase nozzle jet flow experiments. The intensity profiles presented were determined at the nozzle jet centerline for a nozzle inlet pressure near 1.0 MPa (150 psia). The nozzle operating conditions are listed in Table 2.

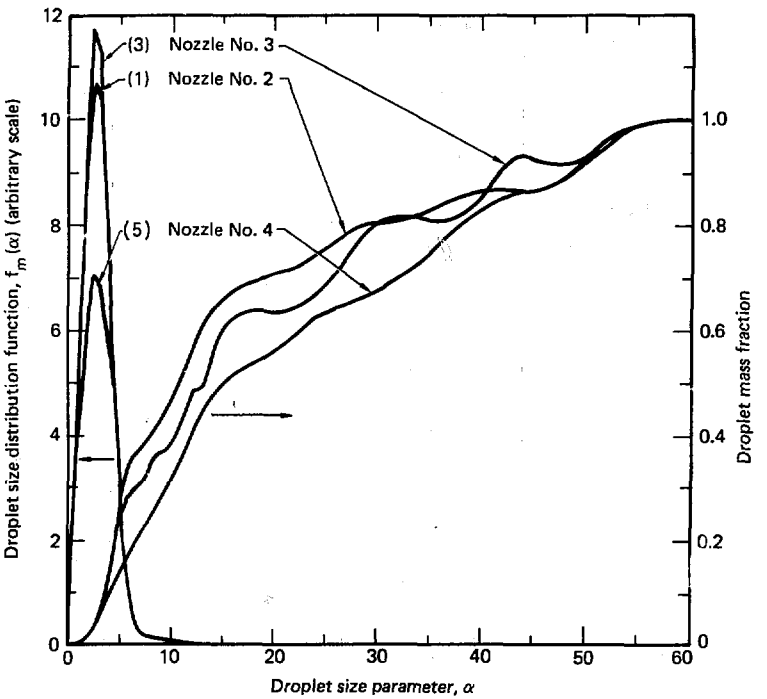

Figure 43. - Measured droplet size distributions and their respective mass fractions resulting from the scattered light intensity profile reconstructions of Figure 41.

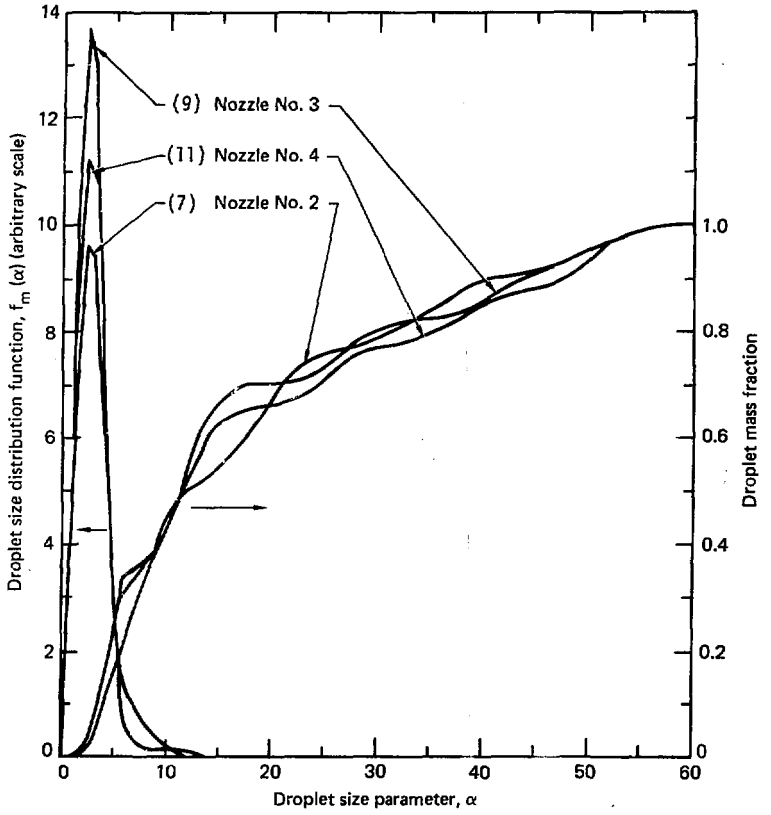

Figure 44. – Measured droplet size distributions and their respective mass fractions resulting from the scattered light intensity profile reconstructions of Figure 42.

of the droplet size distributions, the broadness of the droplet size distributions and the degree of approximation afforded by the series of narrow band size distribution functions. Further refinements in the series of narrow band size distribution functions could eliminate the waviness in the droplet mass fraction profiles, but the droplet size distribution, the average droplet diameters and the average mass fraction profiles would change very little.

Table 3. – Average droplet size parameters for the measured nozzle jet flow droplet size distributions shown in Figures 43 and 44.

Curve No. (Nozzle No.)	Modal Size Parameter, $\bar{\alpha}$	Mean Size Parameter, α_{10}	Sauter Mean Size Parameter, α_{32}	Mass Mean Size Parameter, α_{mm}
1 (2)	2.4	2.9	7.1	10.3
3 (3)	2.4	2.9	8.1	12.1
5 (4)	2.4	3.2	10.2	14.7
7 (2)	2.4	3.3	8.7	11.9
9 (3)	2.4	2.9	7.4	11.3
11 (4)	2.4	2.9	7.8	11.4
Average =	2.4	3.0	8.2	12.0

As indicated by the scattered light intensity profiles and presented in Table 3, there is little difference between the droplet sizes obtained for the different nozzle jet flow measurements. Thus, it can be concluded that changes in droplet size due to nozzle throat radius of curvature changes are small, and that the accuracy of the experimental measurements was not sufficient to detect these small changes. The largest errors involved were those associated with the

nozzle exhaust chamber window and jet spray extraneous scattering. An estimate of the total error involved in these measurements indicated that an accuracy of better than ±20% (±0.4 μm for a 2.0 μm diameter droplet) could be expected for this small droplet diameter regime. Since the predicted droplet size change with changes in nozzle throat geometry was on the order of 15% (see Figure 8), the experimental error band was too great to determine this small droplet diameter difference.

Interestingly, the droplet size distributions have modal diameters near 0.5 μm, but the Sauter mean diameters are near 1.7 μm and the mass-median droplet diameters are near 2.4 μm. This indicates that the nozzle jet flow is dominated by a large number of very small droplets, but they constitute only a small fraction of the total droplet mass. In view of this information, it can be concluded that there are several possible droplet size distributions occurring in the nozzle jet flow. The small droplets (< 2.4 μm) can be associated with the core flow region of the nozzle jet, while the larger droplets may be generated by the boundary layer - liquid film shearing action occurring along the nozzle walls and particularly near the nozzle throat (see references [71] and [85] for similar conclusions concerning two-phase nozzle flows).

Measurements of the droplet size distribution in nozzles with small jet widths as used for this work are likely to produce information that is biased towards large droplet sizes because the nozzle wall boundary effects are much more significant than would be found in large

cross-section impulse turbine nozzles. Thus, the measurements presented herein are conservative, in that a greater fraction of the liquid mass would be expected to be present as small droplets for the impulse turbine blade flow using similar but larger cross-section nozzles.

Results for Nozzle Number 5

The droplet size distribution measurements using nozzle numbers 2 - 4 could not address the effect of the nozzle inlet pressure or throat height upon the droplet size distribution because of their limited expansion ratios and constant throat heights, respectively ($A_e/A^* = 15$ for nozzle numbers 2 - 4). Higher inlet pressures could not be addressed because at an inlet pressure of 2.1 MPa (300 psia) and an inlet enthalpy of 1.16 MJ/kg (500 Btu/lbm) the ideal exhaust pressure would be near 41.4 kPa (6 psia); much too high to satisfy the light transmission requirements (see Figure 4).

To overcome this limitation, variable nozzle number 5 ($A_e/A^* = 29$) was assembled for testing. From an extension of the measured static pressure profiles obtained using nozzle numbers 2 - 4, it was estimated that at an inlet pressure of 2.1 MPa (300 psia) and an inlet enthalpy of 1.16 MJ/kg (500 Btu/lbm) the ideal exhaust pressure would be near 22.1 kPa (3.2 psia). This exhaust pressure would be sufficiently low so that the light transmission requirements could be satisfied and droplet size distribution measurements could be obtained.

During an initial flow test of nozzle number 5, it was determined that the nozzle inlet enthalpy and pressure would be difficult to control. This was mainly because at the very low mass flow rate involved ($A^* = 0.103\ cm^2$ ($0.016\ in^2$)), the heat transfer from the two-phase test facility piping was significant. Also, at the exhaust pressures expected for ideal nozzle expansions, there was a great amount of exhaust chamber window wetting due to nozzle jet spray. The window wetting was apparently caused by underexpanded nozzle operation, which would severely limit the light scattering measurements.

Following this preliminary test, an analysis of the nozzle static pressure profile indicated that the pressure at any given area ratio location in the nozzle was higher than those for corresponding area ratios in nozzle numbers 2 - 4. Figure 45 presents the static pressure profiles for nozzle numbers 3 and 5 for a constant inlet enthalpy. The two pressure profiles should be identical†, and the shift in the pressure profile for nozzle number 5 can only be explained by either flow separation near the nozzle throat or a change in the nozzle area ratio (increase in the throat area). Because of the small throat size, a small change in the throat height would result with a large change in the area ratio. However, this possibility was eliminated by a measurement of the throat area at the time of the nozzle disassembly.

† - A plot of log P/P_0 versus log A/A^* for a nozzle operating with a two-phase, steam-water mixture at the inlet will produce a single line, irrespective of the nozzle inlet pressure or quality as long as the inlet enthalpy is maintained constant. This was shown by Alger [40] and has been confirmed in numerous other two-phase nozzle tests at LLL.

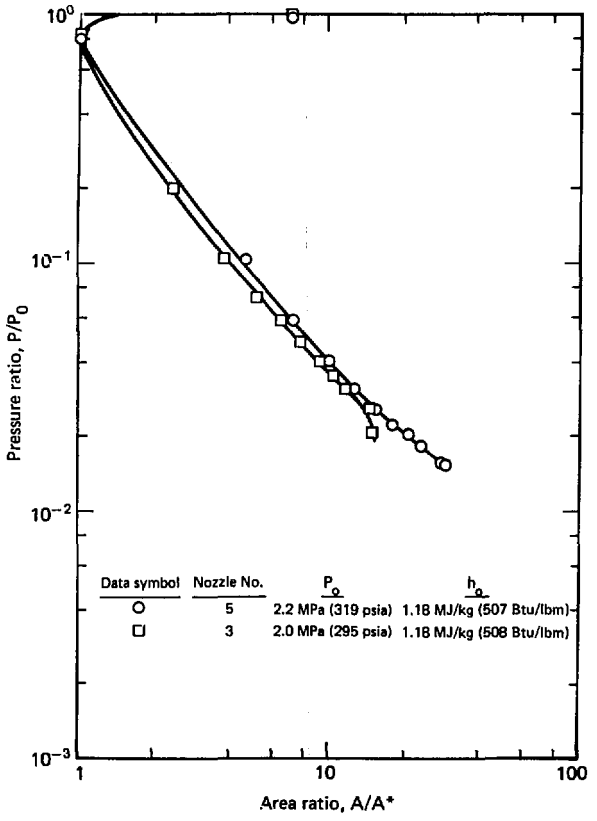

Figure 45. - Static pressure profiles for variable nozzle numbers 3 and 5. The shift in the pressure profile for nozzle number 5 towards higher static pressures indicates that flow separation occurred near the throat.

Thus, it was concluded that flow separation was the cause of the pressure profile shift shown in Figure 45.

During the initial testing of nozzle number 5, light transmission tests indicated that a light scattering measurement could be obtained for a maximum nozzle inlet pressure of 1.4 MPa (200 psia) exhausting to a pressure of 19.3 kPa (2.8 psia). In this case, the nozzle was operated underexpanded to allow a light transmission near 20%. Scattered light intensity profiles for a jet centerline measurement location and two different nozzle inlet and exhaust pressures is shown in Figure 46. Also shown in this figure is a light scattering measurement obtained for nozzle number 3 (intensity profile 3 of Figure 38). The nozzle operating conditions at which these data were taken are presented along with the corresponding light transmission measurements in Table 4.

A comparison of the scattered light intensity profiles of Figure 46 indicates that all of the inverted size distribution functions will be essentially identical. Thus, it can be concluded that changes in droplet size due to nozzle inlet pressure or throat height changes are small for the variations tested. The determination of these small changes in the size distribution function is limited only by the accuracy of the scattered light intensity measurement system and not by the narrow band size distribution inversion method. Thus, an increase in experimental accuracy could allow small changes in the size distribution function to be resolved. Further effort to eliminate the

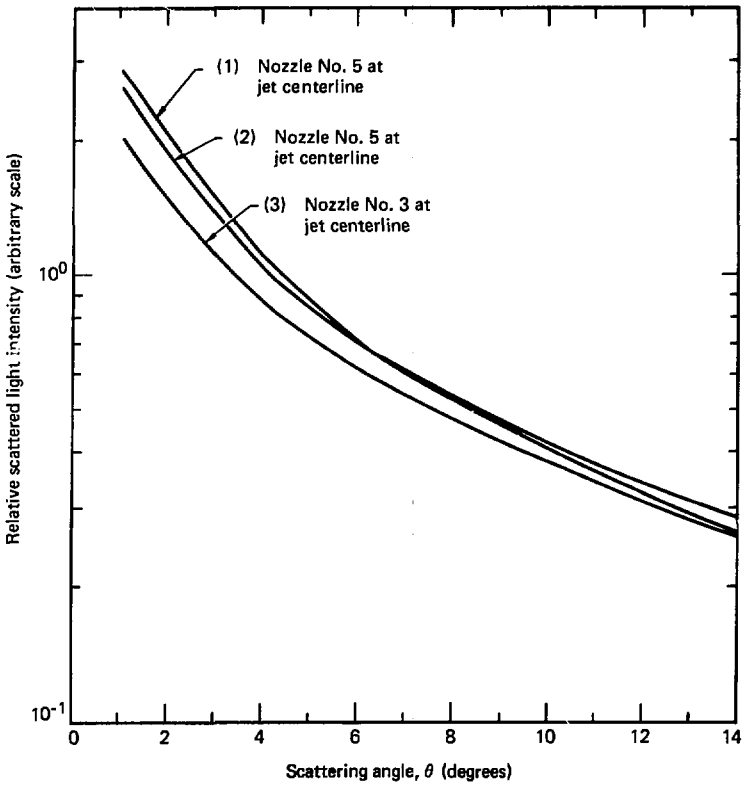

Figure 46. - Measured scattered light intensity profiles for nozzle number 5 operating at inlet pressures near 1.4 MPa (200 psia) and 0.7 MPa (100 psia). A scattered light intensity profile for nozzle number 3, operating at an inlet pressure of 0.7 MPa (100 psia), is also shown for comparison (profile number 3 of Figure 38). The nozzle operating conditions are listed in Table 4.

Table 4. - Nozzle operating conditions corresponding to the scattered light intensity profiles of Figure 46.

Profile No. (Nozzle No.)	Inlet Pressure, MPa (psia)	Inlet Enthalpy, MJ/kg (Btu/lbm)	Exhaust Pressure, kPa (psia)	Light Transmission (λ = 632.8 nm)
1 (5)	1.41 (204)	1.15 (494)	19.3 (2.8)	0.18
2 (5)	0.72 (105)	1.12 (481)	12.4 (1.8)	0.32
3 (3)	0.80 (116)	1.21 (518)	16.6 (2.4)	0.30

flow separation to allow lower exhaust pressures (higher inlet pressures) was deemed unwarranted.

COMPARISON OF MEASURED WITH PREDICTED DROPLET SIZES

The predicted nozzle exit droplet diameter variation as a function of the throat radius of curvature for an inlet pressure of 0.7 MPa (100 psia) and an inlet enthalpy of 1.16 MJ/kg (500 Btu/lbm), as shown in Figure 8, can be compared directly with the measured average droplet sizes listed in Table 3 since the nozzle operating conditions are similar (see Table 2). It can be seen that the predicted droplet diameters using either the thermal equilibrium dynamic breakup (We = 6.0) or the thermal nonequilibrium boiling breakup (average droplet temperature) model are approximately a factor of 3 greater (predicted diameters near 7.5 μm) than the measured nominal mass-mean droplet diameter. These prediction methods might be expected to yield a maximum stable droplet diameter that could exist in a one-dimensional, two-phase nozzle flow, but do not account for the occurrance of many

smaller sized droplets which could form when a single large drop breaks up (see references [50], [51] and [87] - [89]). Since Figures 43 and 44 indicate that about a 7% mass fraction of droplets as large as 10 μm in diameter existed within the nozzle jet flow, it appears that the breakup models employed predict approximately the maximum stable droplet diameter.

However, to improve predictions of the entire nozzle flowfield, the calculated droplet diameter must agree more closely with the experimental data. An improvement of the theoretical models could be accomplished by one or a combination of several methods. One could be the inclusion of a delayed droplet breakup criterion. This would be consistant with the natural oscillation time of a spherical droplet [15], i. e., droplet breakup would not be allowed until a period of time equal to the droplet natural oscillation time had passed. This would cause the droplet to be in a region of greater kinetic and thermal nonequilibrium when breakup was allowed, which should yield smaller droplets. A second possibility for increasing the droplet breakup, which pertains only to the thermal nonequilibrium model, would be to account for a finite mass transfer rate between the phases [90]. This would cause a greater temperature difference to exist between the phases, which would yield greater boiling droplet breakup. However, the most obvious and the simplest means of increasing droplet breakup is to decrease the value of the critical Weber number to yield agreement with experimental results (as indicated in Figure 8, a critical Weber number < 1.0 would be required). An empirical constant could similarly be

included in the boiling breakup model to increase the predicted droplet breakup. This method, though not as physically meaningful as the other possibilities, would yield immediate results with minimum effort.

It is concluded from this comparison of measured with predicted droplet sizes that it is not possible to specify whether kinetic or thermal nonequilibrium forces dominate droplet breakup within the nozzle flow. In fact, it could be that an additional breakup mechanism which yields many small droplets from a single large drop may be present. Also, since surface tension plays an important role in droplet breakup (see equations (11) and (13)), it will be necessary to determine whether surface tension is affected by rapid surface mass transfer. It could be that the concept of equilibrium surface tension is not applicable in such a situation†.

† - The surface tension of the water used in these experiments was measured under equilibrium conditions at room temperature and found to be essentially equal to that quoted in the literature.

DROPLET PHASE

SPATIAL DISTRIBUTION DETERMINATION

Two different experimental optical arrangements were used to determine the spatial distribution characteristics of the droplet phase within the low-quality, two-phase nozzle flow. The two measurement systems were based upon the physical principle of light extinction due to the scattering of light incident upon the particles of a polydispersion. The first method employed a photosensor for a point by point measurement of the light transmission through the nozzle jet flows. This method could only be applied in the nozzle jet flow region because of the wall liquid film problems encountered with the transparent walled nozzles. The second optical system utilized was a shadowgraph arrangement which provided a continuous record of the light transmitted throughout the complete nozzle flow. Because only flow visualization was of interest for the shadowgraph measurements, the transparent walled nozzles were utilized without concern for either the transparent wall - liquid film or the amount of light extinction.

POLYDISPERSE LIGHT TRANSMISSION ANALYSIS

A theoretical analysis of the light transmitted through a polydispersion is more complicated than the analysis presented previously for a monodispersion (e. g., see equations (1) - (5)). The incluson of the scattering effects of each particle in the

polydispersion results with the light transmission equation as [85], [91]

$$\frac{I(0)}{I_o} = \exp\left\{-\left[\frac{3(1-\varphi)\bar{Q}_{ext}}{2D_{32}}\right] t\right\} \tag{50}$$

where the average scattering efficiency factor, $\bar{Q}_{ext}$, is defined as

$$\bar{Q}_{ext} = \frac{\int_0^\infty Q_{ext}\alpha^2 f(\alpha)d\alpha}{\int_0^\infty \alpha^2 f(\alpha)d\alpha} \tag{51}$$

and the Sauter mean diameter, D_{32}, is defined according to equation (48) ($\alpha_{32} = \pi D_{32}/\lambda$). As stated for the light scattering droplet size distribution measurements, single scattering effects must dominate if accurate light scattering (or transmission) measurements are to be obtained.

A comparison between the polydisperse average scattering efficiency factor, $\bar{Q}_{ext}$, given by equation (51) and the monodisperse scattering efficiency factor, Q_{ext}, as a function of the Sauter mean particle size parameter, α_{32}, is shown in Figure 47 ($\alpha_{32} = \alpha$ for a monodispersion). The polydisperse calculations were made using different narrow exponential size distribution functions (see equation (44)). This figure shows that when droplets are either small or large when compared to the incident light wavelength, the average scattering efficiency factor can be approximated without a knowledge of the size distribution function. For the case of small particles ($\alpha_{32} < 4$), $\bar{Q}_{ext}$ and Q_{ext} are

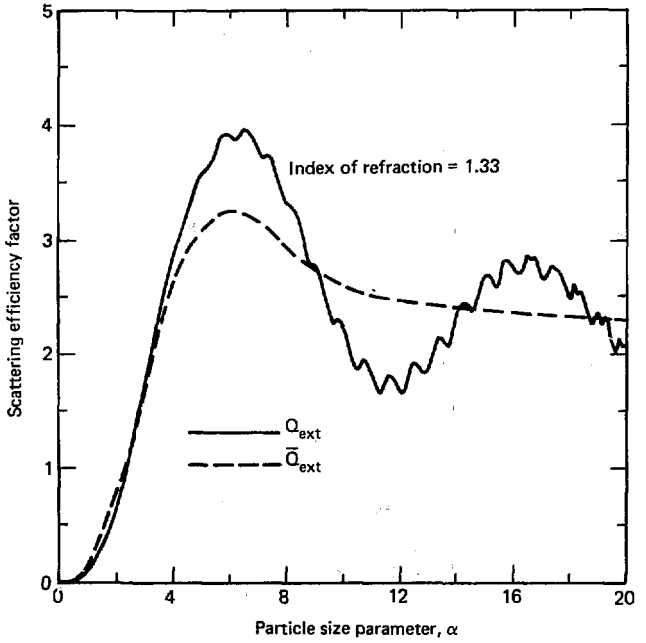

Figure 47. – Comparison of the mean polydisperse scattering efficiency factor, $\bar{Q}_{ext}$, with the monodisperse scattering efficiency factor, Q_{ext}.

essentially equal. When the particles are large ($\alpha > 10$), $\bar{Q}_{ext}$ can be approximated by a linear or constant function for reasonable size parameter ranges. However, when the polydispersion is comprised of particles with sizes between these extremes, no simple means for determining (or approximating) $\bar{Q}_{ext}$ exists without a knowledge of the particle size distribution function.

The application of equation (50) to light transmission measurements in a constant thickness polydispersion results with the vapor volume fraction, φ, the average scattering efficiency factor, $\bar{Q}_{ext}$, and the Sauter mean particle diameter, D_{32}, as unknowns. Light transmission measurements at two different light wavelengths can determine both the vapor volume fraction, φ, and the mean specific particle cross-section, $\bar{Q}_{ext}/D_{32}$. If either of these parameters had been known from other means, a transmission measurement at a single wavelength would only have been necessary to determine the other. In the specific case of very small particles ($\alpha_{32} < 4$), $\bar{Q}_{ext}$ and Q_{ext} are essentially equal and are only a function of the Sauter mean diameter and the incident light wavelength. Thus, for very small or monodisperse size distributions, transmission measurements at two different light wavelengths can yield the vapor volume fraction and the Sauter mean diameter directly. Transmission measurements at several (> 2) different wavelengths are required to determine these parameters when the particle size distribution is multimodal [92]. Further information concerning droplet size and concentration measurements using light extinction methods is given by references [93] - [97].

EXPERIMENTAL DROPLET PHASE SPATIAL DISTRIBUTION MEASUREMENT APPARATUS

Light Transmission Experimental Arrangement

The experimental apparatus used for the light transmission measurements incorporated a receiving optics system similar to that used by Gumprecht and Sliepcevich [98]. A schematic diagram of the experimental arrangement used for this study is shown in Figure 48. The sending and receiving optics arrangement for this system was similar to that used for the light scattering droplet size distribution measurements shown in Figure 34 (there was no need for the film calibration optics used for the light scattering measurements). The light beam from a laser was properly attenuated and apertured by the sending optics and directed to the nozzle jet flow. The light transmitted through the nozzle jet flow was collected by the same lens combination that was used for the light scattering measurements (30 cm effective focal length) and focused to an aperture plate - photosensor combination for detection. The aperture was maintained < 0.5 cm in diameter to allow simple optical alignment while providing an effective collection half angle of less than 0.5 degrees.

Shadowgraph Experimental Arrangement

The experimental arrangement used for the light extinction - flow visualization measurements was essentially the same as that used for typical back-lighted shadowgraph systems [99]. The use of a shadowgraph

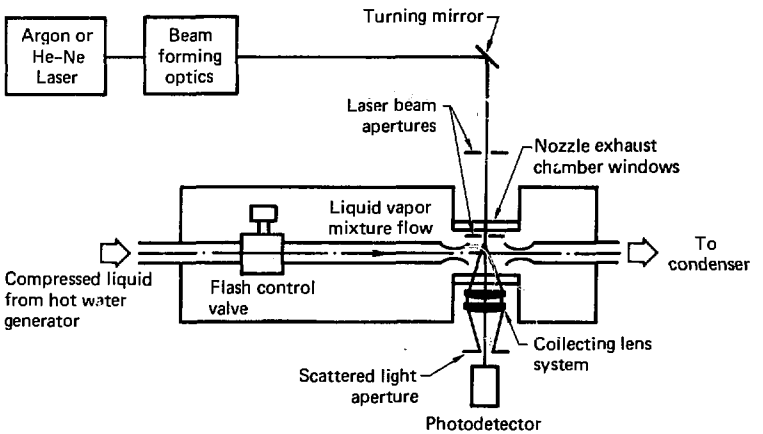

Figure 48. - Schematic of the experimental light transmission optical arrangement.

for single phase fluid flows provides a measurement of the density gradient. However, for the low-quality, dispersed droplet-in-vapor flows of interest, the use of this optical arrangement provides a continuous measurement of the light transmission characteristics of the flow.

The shadowgraph arrangement used for this work is shown schematically in Figure 49. The light from a pulsed ruby laser (λ = 694.3 nm) is expanded and directed to a ground glass scattering plate such that the light leaving the scattering plate is incident upon the two-phase flow in a transparent sidewalled nozzle. The ruby laser energy output was approximately 2 J with a pulse width (controlled by a bleachable dye cell) of 20 - 30 ns. A photograph of the ruby laser is shown in Figure 50. The light transmitted through the nozzle flow was collected and recorded on film using a camera. As with the light scattering droplet size distribution measurements, Kodak linagraph shellburst 2474 film was used because of its red light sensitivity and its 10.2 X 12.7 cm format.

Because of the transparent nozzle wall - liquid film light beam disturbance throughout the nozzle flow and because of the high light attenuation at locations other than the low pressure nozzle exit, this measurement method was used to provide near stop action photographs for flow visualization purposes only. However, this method could be developed (using a calibrated film and the proper sending and receiving optics arrangements) to provide a continuous record of the light

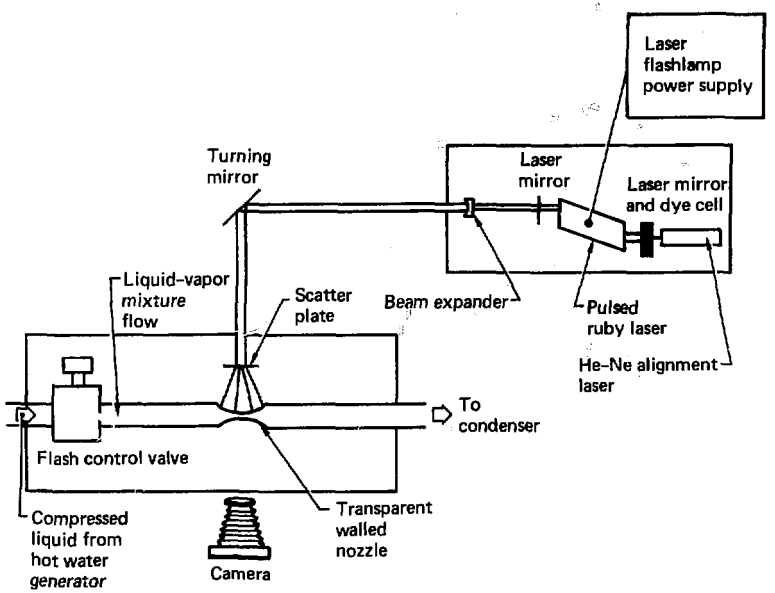

Figure 49. – Schematic of the pulsed ruby laser shadowgraph flow visualization system.

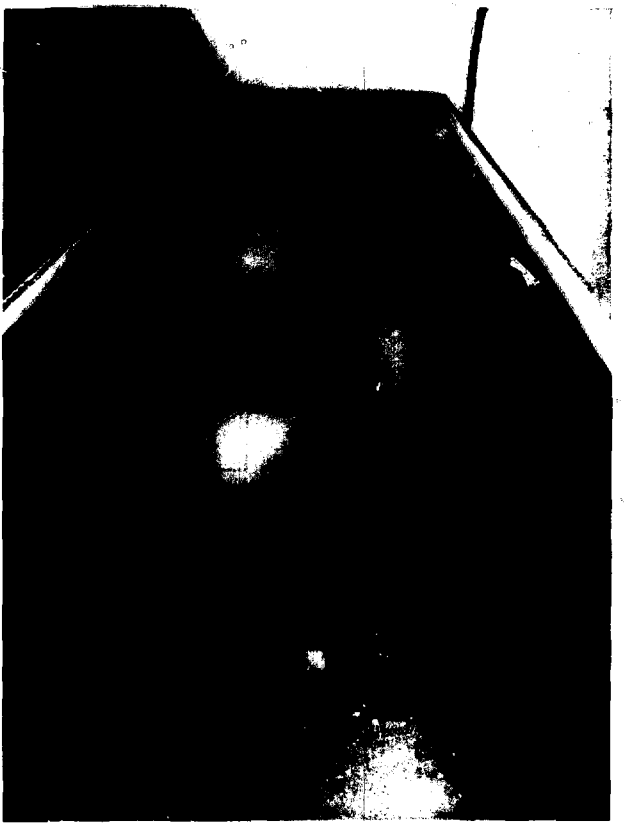

Figure 50. - Photograph of the pulsed ruby laser used for the shadowgraph flow visualization measurements.

transmission through the low-pressure nozzle jet flow region. The use of two or more different wavelengths in this manner could yield a continuous record of the vapor volume fraction and the mean specific droplet cross-section within a two-phase nozzle jet flow.

EXPERIMENTAL DROPLET PHASE SPATIAL DISTRIBUTION MEASUREMENTS

Light Transmission Measurements

Light transmission measurements were obtained in the jet flow region using nozzle numbers 2 - 4 to determine any possible differences due to the nozzle throat geometry. Nozzle number 5 was not utilized for light transmission measurements both because there was no measureable droplet size change between the droplets in the jet flow of this nozzle and the droplets in the jet flows of nozzle numbers 2 - 4 and because of the flow separation and associated window wetting problems that occurred with the operation of this nozzle.

The light transmission measurements were not intended to measure the droplet size directly, but they were to be utilized as a measure of the spatial distribution of the droplet phase within the nozzle jet flow. For this reason, multiple wavelength light transmission measurements were not obtained†. Measurements of the light transmission

† - Light transmission measurements were obtained at the nozzle jet flow centerline using the light wavelengths of the He-Ne (λ = 632.8 nm) and the argon (λ = 514.5 nm) lasers, but they were not intended for multiple wavelength comparisons because of the small wavelength difference.

spatial variation within the nozzle jet flows were obtained using an argon laser oscillating at a wavelength of 514.5 nm.

Figure 51 presents the measured light transmission variation in the nozzle jet flow as a function of the vertical distance from the flow centerline. These measurements were determined in the two-phase nozzle jet flows at a near constant inlet enthalpy of 1.16 MJ/kg (500 Btu/lbm) and nozzle inlet pressures near 0.7 MPa(100 psia), 1.0 MPa (150 psia) and 1.4 MPa (200 psia). The nozzle exhaust pressures were near 13.8 kPa (2.0 psia), 20.7 kPa (3.0 psia) and 27.6 kPa (4.0 psia), respectively. The nozzle operating conditions for these data are presented in Table 5. As with the light scattering droplet size distribution measurements, the experimental information does not show any differences that can be attributed to nozzle throat geometry variation. This is probably due to both the insensitivity of the droplet diameter changes with throat geometry variations and the inaccuracies associated with these experimental measurements. An estimate of the errors involved in these measurements indicated that an accuracy of better than ±10% could be expected.

Figure 51 also indicates that there are no measureable light transmission profile changes with changes in the nozzle inlet pressure. This is true for the 0.7 MPa (100 psia) to 1.4 MPa (200 psia) inlet pressure range investigated. This is consistant with the droplet size distribution measurement results previously discussed, and it indicates that very accurate measurements would be necessary to determine the

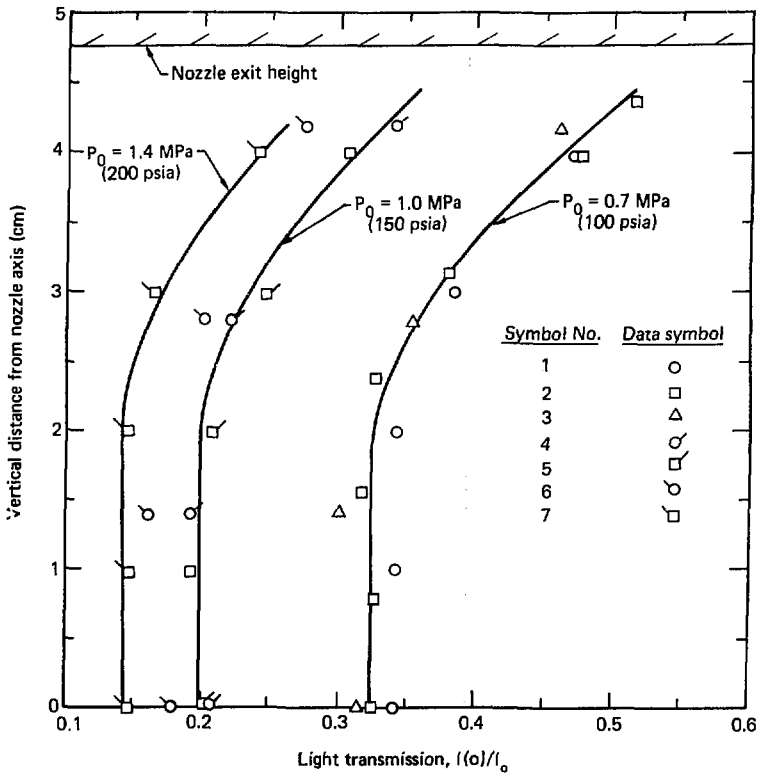

Figure 51. – Measurements of the light transmission as a function of the vertical distance from the nozzle jet flow centerline. The measurements were obtained for nozzle numbers 2 – 4 operating at inlet pressures near 0.7 MPa (100 psia), 1.0 MPa (150 psia) and 1.4 MPa (200 psia). The nozzle operating conditions are listed in Table 5.

Table 5. - Nozzle operating conditions corresponding to the light transmission measurements shown in Figure 51.

Symbol No. (Nozzle No.)	Inlet Pressure, MPa (psia)	Inlet Enthalpy, MJ/kg (Btu/lbm)	Exhaust Pressure, kPa (psia)
1 (2)	0.68 (99)	1.15 (494)	17.2 (2.5)
2 (3)	0.66 (96)	1.15 (492)	13.8 (2.0)
3 (4)	0.71 (103)	1.13 (485)	13.8 (2.0)
4 (3)	1.08 (156)	1.17 (503)	19.3 (2.8)
5 (4)	0.97 (141)	1.14 (491)	20.7 (3.0)
6 (3)	1.38 (197)	1.18 (506)	29.6 (4.3)
7 (4)	1.31 (190)	1.16 (497)	26.9 (3.9)

small changes that occur because of nozzle throat geometry and/or inlet pressure changes. It should be noted that strong multiple scattering effects were encountered for the light transmission data corresponding to the 1.4 MPa (200 psia) inlet pressure, invalidating the information for other than qualitative comparison purposes.

The information presented in Figure 51 can be further utilized to provide a better understanding of the spatial variation of the droplet phase within the two-phase, liquid-dominated nozzle jet flows. Equation (50) shows that the light transmission for a constant thickness polydispersion is a function of the variables: $(1 - \varphi)\bar{Q}_{ext}/D_{32}$. Thus, assuming that the mean specific droplet cross-section, $\bar{Q}_{ext}/D_{32}$, is a constant at any location in the nozzle jet flow (the variation of this parameter is not expected to be great because of the spatial uniformity in the droplet size distribution and droplet velocity measurements), the

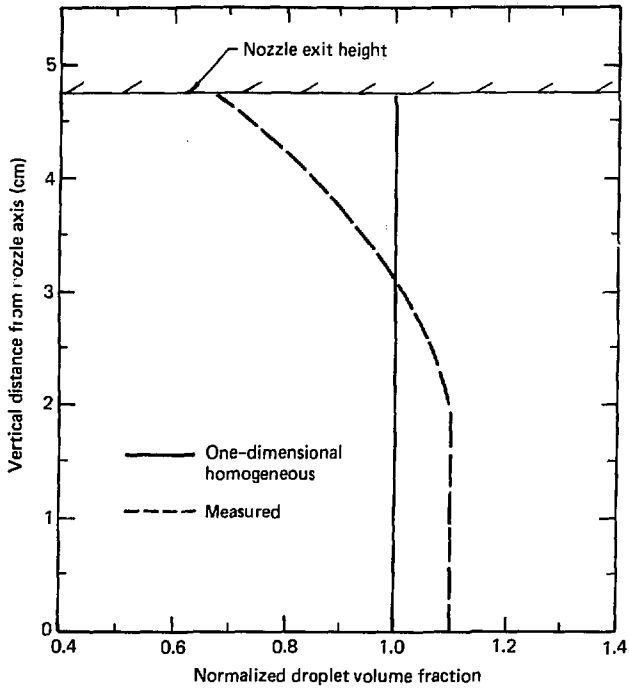

Figure 52. - Normalized droplet volume fraction variation across the nozzle jet half width.

light transmission results simply become a measure of the droplet volume fraction, $(1 - \varphi)$. This quantity can be normalized using the one-dimensional, homogeneous droplet volume fraction to yield the result shown in Figure 52. The line corresponding to the one-dimensional, homogeneous droplet volume fraction variation is shown for reference. The area under the experimental curve has been normalized to equal the area under the one-dimensional curve for the comparison.

The experimental curve of Figure 52 is a result of the light transmission data corresponding to the nozzle inlet pressures of 0.7 MPa (100 psia) and 1.0 MPa (150 psia). Only one curve is shown because of the near identical relative light transmission profiles for the two inlet pressures. This figure indicates that the droplet phase is quite uniformly distributed over the nozzle jet profile, and the actual droplet volume fraction is approximately a factor of 1.1 greater than the one-dimensional droplet volume fraction at the nozzle jet centerline. This droplet volume fraction profile is much more spatially uniform than those that were obtained for two-component, gas-particle flows [7]. However, comparison of this profile with droplet volume fraction profile obtained for a high quality nozzle flow [100] shows good agreement.

The light transmission measurements can also be utilized to corroborate the light scattering droplet size distribution measurements. This requires a calculation of the exponent of equation (50). In order to accomplish this calculation, a nozzle inlet enthalpy of 1.15 MJ/kg

(492 Btu/lbm), a nozzle inlet pressure of 0.7 MPa (96 psia) and a nozzle exit pressure of 13.8 kPa (2.0 psia) was chosen for the nozzle operating conditions to correspond with the data set number 2 of Figure 51. This yields a one-dimensional, homogeneous droplet volume fraction of 2.2×10^{-4} at the nozzle jet flow centerline (after multiplication by the factor of 1.1 indicated by the results shown in Figure 52). Now, calculating the mean scattering efficiency factor according to the measured droplet size distribution for nozzle number 3 (see Figure 43) yields $\bar{Q}_{ext} = 2.3$ for $\alpha_{32} = 10.0$ ($\lambda = 514.5$ nm). A calculation of the light transmission using these variables yields ($l = 0.325$ cm) $I(0)/I_o = 0.22$. This value is much lower than the light transmission measurements obtained. Thus, assuming a larger Sauter mean diameter of 2.0 μm and linearly extending $\bar{Q}_{ext}$ according to the percentage changes indicated by Figure 47 results with $\bar{Q}_{ext} = 2.2$ and $I(0)/I_o = 0.31$. This value is very nearly the same as the value obtained for the transmission measurement used for the comparison. Thus, the light transmission measurement indicates that a Sauter mean diameter near 2.0 μm existed in the nozzle jet flow, which agrees very well with the Sauter mean diameters obtained from integrations of the droplet size distribution functions measured at the nozzle jet centerline (see Table 3). Similar results can be obtained by considering the 1.0 MPa (150 psia) light transmission measurements.

Also, it should be noted that the change in the measured light transmission values between the 0.7 MPa (100 psia) and 1.0 MPa (150 psia) nozzle inlet pressure data of Figure 51 corresponds directly

with changes in the droplet volume fraction at the respective 13.8 kPa (2.0 psia) and 20.7 kPa (3.0 psia) exhaust pressures. This confirms that there is little droplet diameter change with an inlet pressure change for the range of operating conditions presented. A similar comparison cannot be accurately applied to the 1.4 MPa (200 psia) nozzle inlet pressure data because of the multiple scattering effects involved.

Shadowgraph Flow Visualization Measurements

Shadowgraph flow visualization photographs were obtained for various two-phase nozzle flow conditions using the transparent walled nozzle numbers 1 and 6. In particular, the nozzle inlet and throat region flow patterns, the droplet flow channeling throughout the nozzle flows and the two-phase boundary layer separation and shock wave flow phenomena were photographed using the pulsed ruby laser shadowgraph arrangement. The nozzle operating conditions for each of the following shadowgraph photographs are presented in Table 6.

A shadowgraph photograph of the two-phase flow in nozzle number 6, operating at an inlet pressure near 0.7 MPa (100 psia), is shown in Figure 53. The entire nozzle length was not photographed so that better resolution in the nozzle inlet and throat flow regions could be obtained. This photograph† shows the flow in these regions very

† - The apparent flow nonuniformities adjacent to the contoured nozzle walls are not caused by flow phenomena. Rather, they are the unfortunate result of too liberal of an application of a silicone sealer compound used to cushion and seal the glass sidewall - metal contoured wall joint area.

Table 6. - Nozzle operating conditions corresponding to the shadowgraphs photographs shown in Figures 53 - 56.

Figure No. (Nozzle No.)	Inlet Pressure, MPa (psia)	Inlet Enthalpy, MJ/kg (Btu/lbm)	Exhaust Pressure, kPa (psia)
53 (6)	0.72 (105)	1.17 (501)	24.8 (3.6)
54 (6)	0.24 (35)	1.15 (494)	77.9 (11.3)
55 (1)	0.71 (103)	1.20 (514)	73.1 (10.6)
56 (6)	0.72 (105)	1.17 (505)	35.9 (5.2)

clearly. The regions of high droplet concentration appear as darker areas because of the increased light extinction due to the increased light scattering in these areas. It can be seen that several different droplet channeling regions are formed in the nozzle converging section. The upper and lower droplet channeling regions appear to be caused by the turning of the flow in the converging section of the nozzle, i. e. the vapor phase turns from the parallel inlet flow to follow the converging nozzle walls, but the droplet phase cannot react as rapidly and crosses the vapor phase streamlines to form regions of high droplet concentration due to the combined effects of vapor phase turning and collisions with the nozzle walls and other droplets. The central droplet channel appears less dense than the others and probably consists of those droplets least subjected to the turning effects of the nozzle walls.

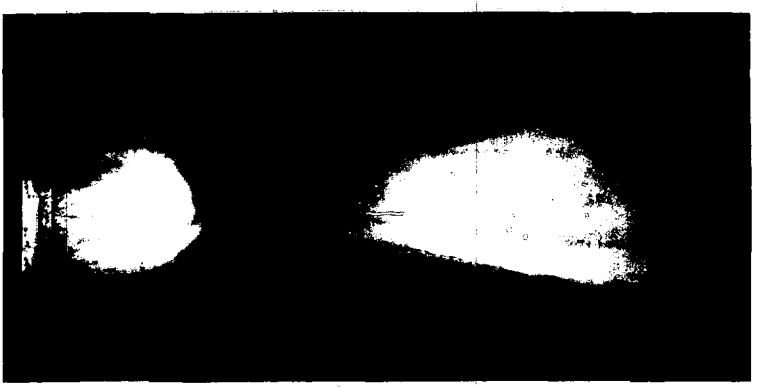

Figure 53. - Shadowgraph photograph of the two-phase flow in nozzle number 6 operating at an inlet pressure near 0.7 MPa (100 psia). The nozzle operating conditions are listed in Table 6.

The two-phase fluid leaving the throat appears to be fairly uniformly mixed, except for one high droplet concentration region that exists throughout the complete supersonic nozzle flow. It is interesting that this droplet channeling does not follow the nozzle axis, but is displaced a considerable distance from the axis throughout the diverging section of the nozzle. This channeling region is most likely formed of relatively large droplets because of its origin in a nonuniform droplet concentration region of the nozzle throat and its inability to disperse. From the information contained in this photograph, it appears that flow channeling in the diverging section of the nozzle could be eliminated and subsequently, the droplet breakup could be enhanced by a phase separation prior to the nozzle inlet with a properly implemented phase remix in the nozzle converging section near the nozzle throat.

Figure 54 presents a shadowgraph photograph of a shock wave occurring just downstream of the nozzle throat region in nozzle number 6. The location of the normal shock this close to the nozzle throat required a very low pressure inlet condition (241.3 kPa (35 psia)). At this low inlet pressure the droplet phase flow patterns were greatly changed over those shown in Figure 53, i. e., droplet channeling in the converging section is mainly restricted to the central region, and the flow downstream of the nozzle throat appears very uniform in the droplet spatial distribution. It can be seen that the normal shock profile is severly distorted over that which would be obtained for a pure gas flow. This distortion is presumably due to the spatial kinetic and thermal

Figure 54. - Shadowgraph photograph of a normal shock wave occurring downstream of the nozzle throat region in nozzle number 6 operating at an inlet pressure near 241.3 kPa (35 psia). The nozzle operating conditions are listed in Table 6.

nonequilibrium occurring because of the spatial variation in the droplet phase concentration.

During the experimental time that was taken to locate this shock wave, several interesting nozzle flow phenomena were observed. It was noted that for any reduction in the nozzle inlet pressure (< 34.5 kPa (5 psia) change), the shock wave would immediately move upstream through the throat region and cause the nozzle to operate completely subsonic. Conversely, for any increase in the nozzle inlet pressure (< 34.5 kPa (5 psia) change), the shock would begin to move downstream, the boundary layer flow would separate and the normal shock would become an oblique shock - normal shock combination.

Figures 55 and 56 present shadowgraph photographs of the boundary layer separation and shock wave phenomena that occurred for high velocity shock conditions. Figure 55 was obtained by operating nozzle number 1 at an inlet pressure near 0.7 MPa (100 psia) and at an exhaust pressure of 73.1 kPa (10.6 psia). In this photograph, the boundary layer separation and oblique shock patterns can be seen at both the upper and lower nozzle walls. In the central flow region there exists a curved *normal* shock wave. The peak of the curvature is located at the point of maximum droplet concentration, indicating that the droplet concentration has a strong effect upon the shock structure. Also, it should be noted that the droplet channeling appears to be more pronounced for this nozzle than it was for nozzle number 6 (nozzle number 1 has a larger throat radius of curvature). A pressure profile

Figure 55. – Shadowgraph photograph of the boundary layer separation and shock structure that existed near the exit in nozzle number 1 operating at an inlet pressure near 0.7 MPa (100 psia). The nozzle operating conditions are listed in Table 6.

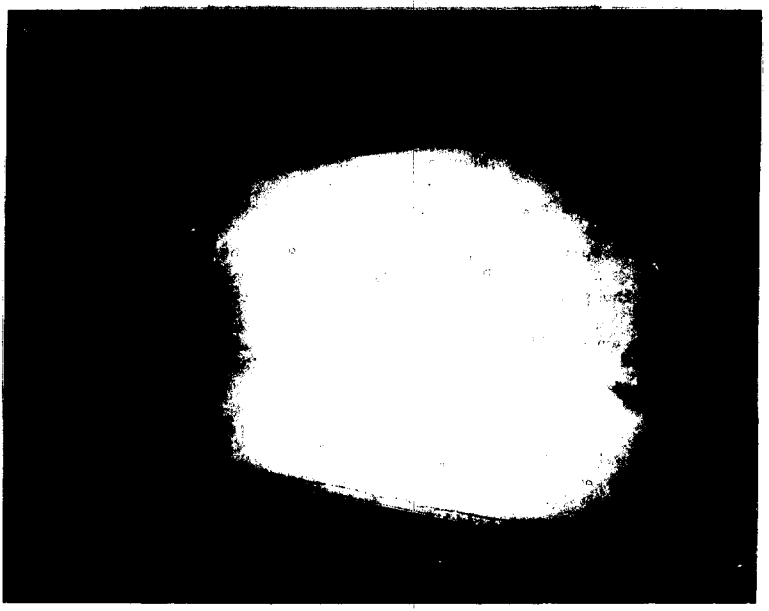

Figure 56. - Shadowgraph photograph of the boundary layer separation and shock structure that existed near the exit (at right side of photograph) in nozzle number 6 operating at an inlet pressure near 0.7 MPa (100 psia). The nozzle operating conditions are listed in Table 6.

typical of a nozzle operating under similar conditions was presented in reference [43]. This photograph verifies the occurrence of the boundary layer separation and oblique shock phenomena proposed in reference [43].

Figure 56 was obtained by operating nozzle number 6 at an inlet pressure near 0.7 MPa (100 psia) and at an exhaust pressure of 35.9 kPa (5.2 psia). As in Figure 55, the boundary layer separation and oblique shocks can clearly be seen at the nozzle walls. However, in this case the normal shock structure is even more complex. This is evidently due to the two droplet channeling streams that can be observed entering the shock at the peaks of the shock curvature. A comparison of the droplet channeling shown in Figures 55 and 56 indicates that the droplet channeling in the diverging section of the nozzle is reduced by a reduction in the throat radius of curvature. Also, because of the small flow regions occupied by the channeled droplets and their possible spatial variation with both nozzle geometry and inlet condition changes, any measurement of the droplet sizes in these regions would require many measurements and high spatial resolution.

LASER-DOPPLER VELOCIMETER

DROPLET VELOCITY DETERMINATION

DOPPLER FREQUENCY SHIFT OF LIGHT SCATTERED FROM A MOVING DROPLET

Measurement of the velocity of a moving droplet using a laser-Doppler velocimeter depends upon two basic physical principles. The first principle is that the droplet will scatter a fraction of any incident light; a topic that was discussed in previous sections of this report. The second basic principle is that the light scattered from the moving droplet can be different in frequency from the incident light frequency. This frequency difference is proportional to the droplet velocity relative to the light source velocity and is commonly called the Doppler frequency shift.

The well known Doppler effect in accoustics can be simply explained for a stationary sound source and a moving (constant velocity) observer. As the observer moves towards the sound source, sound waves are encountered more frequently than if the observer were to remain stationary, i. e., the observer would hear a higher frequency than that of the sound source. Conversely, if the observer moves away from the sound source, a lower frequency would be heard. However, in the case of a stationary observer and a moving source, the observer experiences wavelength changes rather than frequency changes.

A similar Doppler effect occurs when analyzing the frequency change of the light scattered from a moving droplet. The analysis of the total Doppler frequency shift in the scattered light must be performed in two steps. First, the droplet is treated as a moving observer relative to a stationary light source. The frequency of the incident light, as experienced by the droplet (see Figure 57 for the details of the scattering geometry), can be written as

$$f_p = \frac{(c - \vec{u}_d \cdot \vec{k}_i)}{\lambda_i} \tag{52}$$

In this case, if the droplet is moving towards the light source, the droplet experiences light at a frequency higher than that of the light source. Secondly, this higher frequency light is scattered from the moving droplet to a stationary observer for measurement. Because this situation can be represented as a moving source – stationary observer, the wavelength of the light received at the observation point will be changed. This new wavelength can be expressed as

$$\lambda_s = \frac{(c - \vec{u}_d \cdot \vec{k}_s)}{f_p} = \lambda_i \frac{(c - \vec{u}_d \cdot \vec{k}_s)}{(c - \vec{u}_d \cdot \vec{k}_i)} \tag{53}$$

In this case, if the droplet is moving towards the stationary observer, the light wavelength observed will be smaller than that scattered from the droplet. This will result with an even higher light frequency at the observation location than present in either the scattered (relative to the droplet) or unscattered light beams. The Doppler frequency shift, the difference between the light source frequency and the scattered light frequency, can be written as

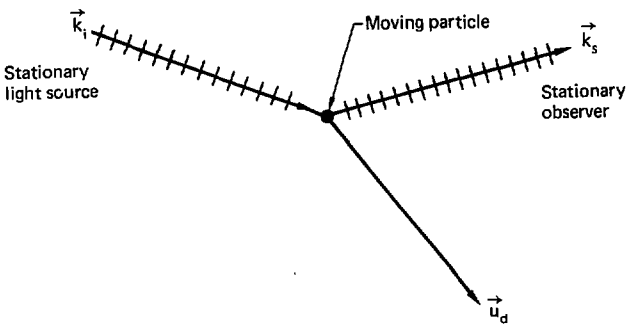

Figure 57. – Diagram indicating the incident, $\vec{k}_i$, and scattered, $\vec{k}_s$, light direction unit vectors for a droplet moving with a constant velocity vector, $\vec{u}_d$.

$$\Delta f = f_i - f_s = c \left(\frac{1}{\lambda_i} - \frac{1}{\lambda_s} \right) \tag{54}$$

Upon combining equations (52) - (54), the total Doppler frequency shift becomes

$$\Delta f = \left(\frac{\vec{u}_d}{\lambda_i} \right) \cdot (\vec{k}_i - \vec{k}_s) \tag{55}$$

where the approximation that $c >> |\vec{u}_d|$ has been applied. Note also that the index of refraction of the continuous phase has been assumed equal to one for this derivation.

DOPPLER FREQUENCY SHIFT DETERMINATION

The Doppler frequency shift caused by a particle traveling at a speed corresponding to most physical continuum flow situations is very small when compared to the initial light frequency. For example, a droplet traveling at a velocity of 10 m/s will produce a maximum normalized frequency shift of $\Delta f/f_i = 6.7 \times 10^{-8}$, or 1 part in 15 million. This is exceedingly small, and would be difficult to measure with the best spectroscopic techniques available. However, because of the high frequency of the incident light (4.7×10^{14} Hz for $\lambda = 632.8$ nm), a frequency shift of 1 part in 15 million corresponds to a 31.6 MHz frequency change, which is a readily measureable effect. The two basic methods for measuring this frequency shift will now be presented.

Signal Analysis Using Optical Mixing Spectroscopy

One method for determining the small relative Doppler frequency shift in the light scattered from a moving droplet is the use of optical mixing spectroscopy. In optical mixing spectroscopy the scattered light beam is optically mixed with the incident light beam and passed into a square law photodetector [101], [102] as shown in Figure 58. The output of the square law detector is a beat frequency which is equal to the sum and difference of the incoming signal frequencies (the high frequency component is discarded due to photodetector response or electronic filtering). Thus, the measurement of the Doppler frequency difference is obtained directly, which eliminates the need for an absolute frequency measurement. LDV arrangements employing this method of Doppler frequency shift detection are commonly termed as heterodyne techniques, after the super-heterodyne techniques employed in radio frequency and microwave communications.

Three of the most common heterodyne LDV optical arrangements are shown in Figure 59. The first arrangement (Figure 59(a)) is the local oscillator (reference beam) heterodyne system, in which the incident light beam is mixed with the scattered light for beat frequency analysis. The second arrangement (Figure 59(b)) is termed the differential (dual beam) heterodyne system, and the third arrangement (Figure 59(c)) is called the symmetric (single beam) heterodyne LDV. These two LDV arrangements are very similar in that they optically mix the light scattered in two different directions. The result is that the

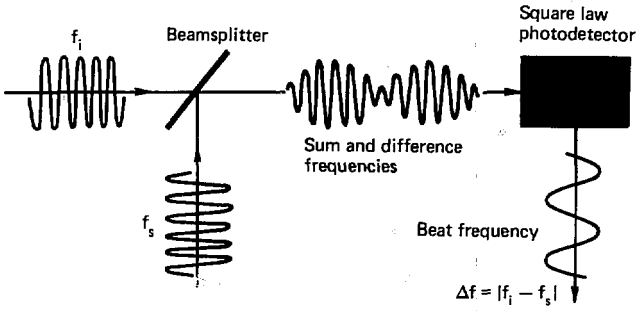

Figure 58. – Schematic representation of the mixing of the scattered and unscattered light beams for an optical mixing spectroscopy (heterodyne) LDV arrangement. Note the high (sum) and low (difference) frequency components of the mixed light beam.

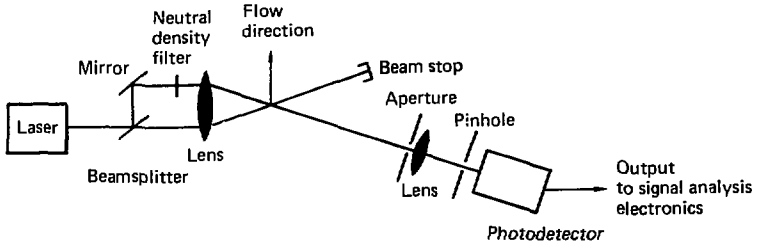

(a) Local oscillator (reference beam) heterodyne

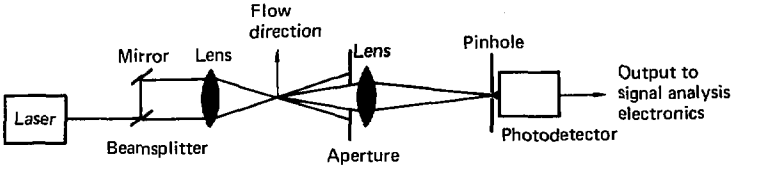

(b) Differential (dual beam) heterodyne

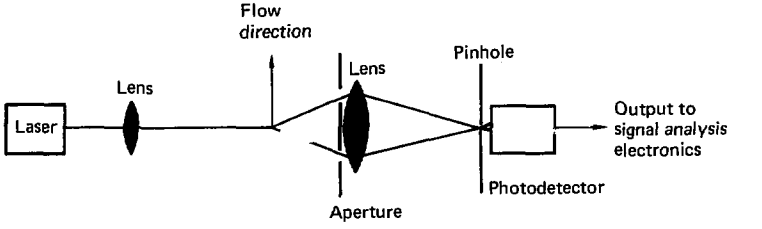

(c) Symmetric (single beam) heterodyne

Figure 58. - Schematic representations of three of the most common heterodyne LDV arrangements.

light scattered in one direction is positively shifted in frequency, and the light scattered in the other direction is negatively shifted in frequency. This scattered light is mixed and the beat frequency results with a measure of the total Doppler frequency shift.

The simplest method used to determine the Doppler frequency shift for a heterodyne LDV arrangement is to analyze the photodetector output with a spectrum analyzer. The frequency corresponding to the peak of the spectrum determines the mean particle velocity, and the half width at half maximum yields the root-mean-square of the velocity fluctuation. Other photodetector signal processors that are commonly used include the Doppler burst counter, the frequency tracker and the photon correlator (for very low scattered light levels). Typically, the maximum Doppler frequency shift that can be determined in a heterodyne arrangement is near 100 MHz. This upper frequency limit is controlled by the photodetector and signal analysis electronics portion of the system.

Direct Optical Signal Analysis

In discussing the Doppler frequency shift determination, it was mentioned that it would be difficult for the best spectroscopic system to accurately resolve the small relative Doppler frequency shift. There is, however, an optical instrument that allows an accurate determination of the wavelength of a beam of light. This instrument is known as the spherical mirror Fabry-Perot interferometer (FPI) [103]. LDV systems generally incorporate the use of a scanning FPI for a relative, rather

than absolute, determination of the Doppler frequency shift, i. e., the frequency (or wavelength) difference between the frequency shifted scattered light and a known light frequency standard is measured. This provides a direct optical measurement of the Doppler frequency difference.

In a typical application, the LDV-FPI optical arrangement is that of the reference beam mode in which both the scattered and unscattered light beams are mixed for frequency analysis using a confocal scanning FPI (see references [104] - [108]). However, several authors [8] and [109] - [112] have found that the single beam LDV arrangement also works well when using a Fabry-Perot interferometer for the Doppler frequency shift analysis. The reference beam LDV-FPI arrangement is shown schematically in Figure 60(a). As the distance between the confocal mirrors of the interferometer is piezoelectrically scanned, a changing interference pattern can be observed (see Figure 60(b)). The central fringe will become alternately bright and dark, depending upon whether the mirror spacing corresponds to an integral number of wavelengths (maximum intensity) or a half integral number of wavelengths (minimum intensity). For reference beam LDV-FPI operation, there will be a bright fringe corresponding to the wavelengths (frequencies) of both the scattered and unscattered light beams. These bright fringes will occur at different mirror spacings. The output of a photodetector monitoring these bright fringes is displayed by an oscilloscope as a function of the FPI mirror spacing for the subsequent determination of the frequency difference. This frequency difference is the Doppler frequency shift

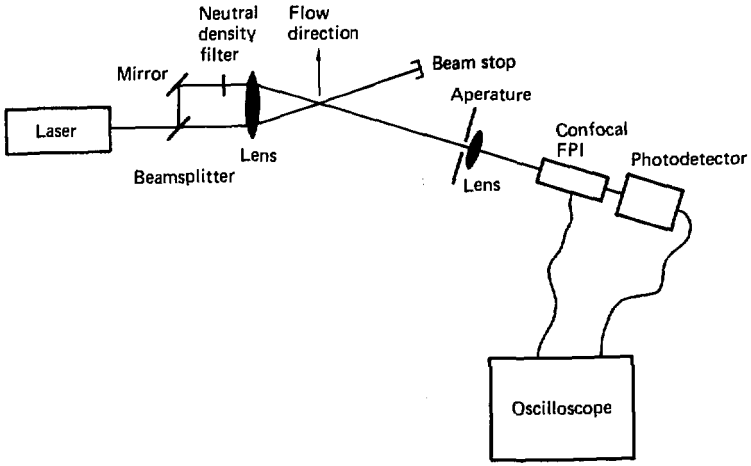

(a) Reference beam LDV-FPI system

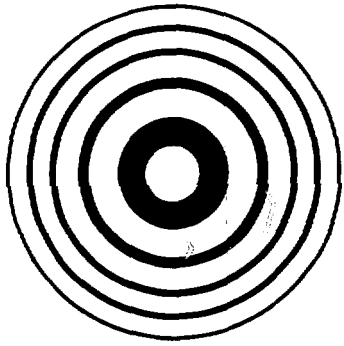

(b) FPI interference pattern

Figure 60. - Schematic representations of the reference beam LDV-FPI arrangement (part (a)) and the interference pattern generated by the confocal scanning Fabry-Perot interferometer (part (b)).

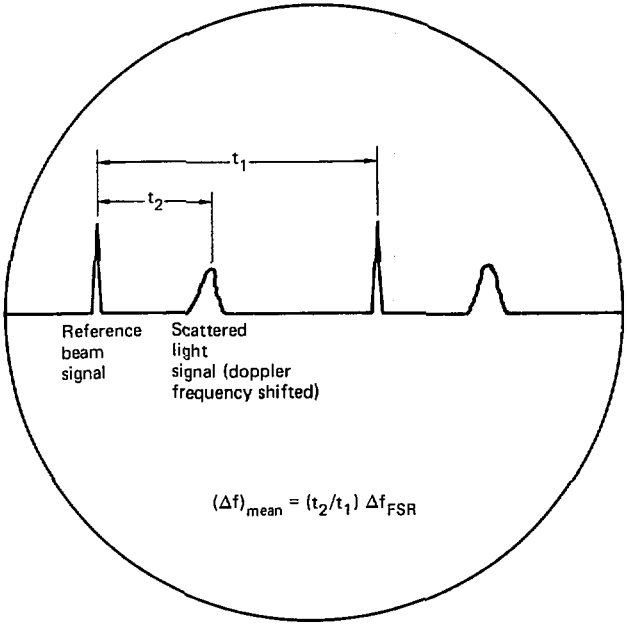

Figure 61. - Schematic of an oscilloscope trace for a reference beam LDV-FPI arrangement showing the method for determining the Doppler frequency shift.

and can be determined by a direct comparison with the known maximum frequency range (free spectral range, or FSR) of the FPI. This process is shown schematically in Figure 61.

The free spectral range of the confocal FPI corresponds to the mirror separation necessary to change the intensity of the bright central fringe between successive maxima, and is expressed in terms of the mirror radius, r, and the speed of light, c, as

$$\Delta f_{FSR} = \frac{c}{4r} \tag{56}$$

A measure of the FPI's capability to resolve different wavelengths is called the resolving power, P_R, and is given by

$$P_R = \frac{\lambda}{\Delta\lambda} \tag{57}$$

where $\Delta\lambda$ is the smallest wavelength change that can be resolved and depends upon the width of a fringe. Generally, the resolution of the confocal FPI is expressed in terms of the finesse F. For a mirror reflectivity, R, near unity, the finesse can be written as

$$F = \frac{\lambda P_R}{4r} \approx \frac{\pi}{2(1 - R)} \tag{58}$$

The finesse is improved by increasing the reflectivity of the mirrors and the accuracy of the mirror contours. However, as the mirror reflectivity is increased, the light transmission decreases, resulting in the necessity of a proper design for optimum use. The light transmission, T, of the FPI is given by the equation

$$T = \frac{1}{2(1 + a_l/t)^2} \tag{59}$$

where a_l is the combined mirror absorption and scatter loss and t is the mirror transmissivity. The frequency resolution, Δf_{FPI}, of the confocal FPI is

$$\Delta f_{FPI} \simeq \frac{c}{\lambda P_R} = \frac{\Delta f_{FSR}}{F} \tag{60}$$

Standard commercial instruments with free spectral ranges between 1.5 and 2.0 GHz generally have a finesse > 200. These values yield a frequency resolution better than 10 MHz.

LDV CONSIDERATIONS FOR HIGH-VELOCITY, LIQUID-DOMINATED NOZZLE FLOW MEASUREMENTS

Doppler Frequency Shift and Measurement Volume Size

Measurement of the mean droplet velocity in high-velocity, high droplet concentration nozzle flows using LDV techniques requires a consideration of several important system parameters, e. g., the maximum Doppler frequency shift, the measuring volume size, the laser power requirements and the configuration and alignment of the optical components. The maximum Doppler frequency shift and the measuring volume size are directly related to the beam separation and sending lens focal length for a dual beam LDV arrangement (see Figure 59(b)). The application of equation (55), to the LDV arrangements of Figure 59, leads to the following relation for the Doppler frequency shift in terms

of the beam intersection half angle, φ, the particle velocity, u_d, and the light wavelength, λ, [101], [102]:

$$\Delta f = \frac{2\, u_d \sin \varphi}{\lambda} \tag{61}$$

From this result, the Doppler frequency shift is seen to increase with an increase in the droplet velocity or an increase in the beam intersection angle for a given light wavelength. For high-velocity flows, this frequency can easily be greater than the 100 MHz limit of the photodetector and electronics signal analysis equipment for a heterodyne LDV arrangement. This problem can be resolved by either reducing the beam intersection angle (e. g., at a droplet velocity of 1000 m/sec and a wavelength of 514.5 nm a beam intersection half angle of $\leq$1.5 degrees is required for the $\leq$100 MHz frequency limit), or a scanning confocal Fabry-Perot interferometer can be used for the resulting high frequency shift measurement.

Doppler frequency shift reduction for high velocity flows by a reduction of the beam intersection angle results in an increase in the measuring volume. The effective diameter of the beam intersection region is given as [102]

$$d_{mv} = \frac{5\lambda F_t}{\pi\, D_b \cos \varphi} \tag{62}$$

Here F_t is the sending lens focal length, and D_b is the initial laser beam diameter where the intensity has dropped to $1/e^2$ times the center intensity. The length of the measuring volume is given as [102]

$$l_{mv} = \frac{5\lambda F_l}{\pi D_b \sin \varphi} \qquad (63)$$

Thus, for a 1.5 degree beam intersection angle, an initial beam diameter of 0.25 cm, a light wavelength of 514.5 nm and a lens focal length of 40 cm, the measuring volume effective diameter is 0.13 mm and its effective length is 5.01 mm.

The use of a measuring volume of this length in a thin, high-velocity, high particle concentration flow can result in several difficulties. The length of the measuring volume would completely span the thickness of the nozzle jet for nozzle numbers 2 - 5, resulting in no spatial resolution and the inclusion of velocity gradients due to the jet velocity profile within the measuring volume. Also, because of the high droplet concentration, there could be as many as 2600 droplets in the measuring volume (resulting in frequency analysis problems) for the nozzle exit conditions of Table 1 and 2 μm diameter droplets. The combination of these effects severely limits the usefulness of the heterodyne LDV techniques for the high-velocity, high droplet concentration nozzle flows. However, very small measuring volumes (resulting with very high Doppler frequency shifts) can be used with LDV-FPI systems operating in high-velocity flows, resulting in substantially improved spatial resolution and a significantly reduced number of droplets in the control volume. Because of these considerations, the LDV-FPI system became very attractive for use in this study.

Qualitative LDV Arrangement Comparisons for High Droplet Concentration Flows

To determine which LDV signal analysis technique, either the heterodyne method using a spectrum analyzer or the direct optical method using a scanning FPI, would be best suited for the high-velocity, high droplet number density nozzle jet flows, a series of comparative experiments were performed. These experiments were designed only to produce a qualitative comparison of the usefulness of these LDV techniques under severe test conditions representative of the two-phase, steam-water nozzle jet flows of interest. A small converging-diverging nozzle (0.318 cm thick rectangular nozzle exit) operating with an air-water, two-phase mixture that approximated the high droplet number density of the steam-water nozzle jet flow was used. The droplet velocity at the nozzle exit was measured to be near 300 m/s, which proved to be sufficiently high enough to allow a comparison between the different LDV signal analysis techniques.

Three different LDV arrangements were compared using the air-water, two-phase nozzle jet flow. These LDV techniques included the reference beam heterodyne (Figure 62(a)), the dual beam heterodyne (Figure 62(b)) and the reference beam scanning confocal FPI (Figure 62(c)). All the methods were operated in the forward scattering mode using a single frequency argon laser (λ = 514.5 nm).

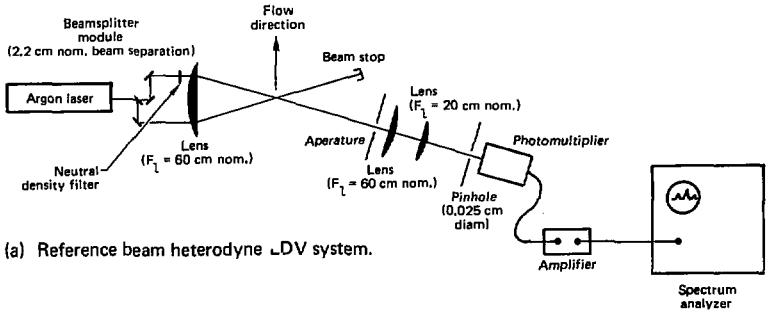

(a) Reference beam heterodyne LDV system.

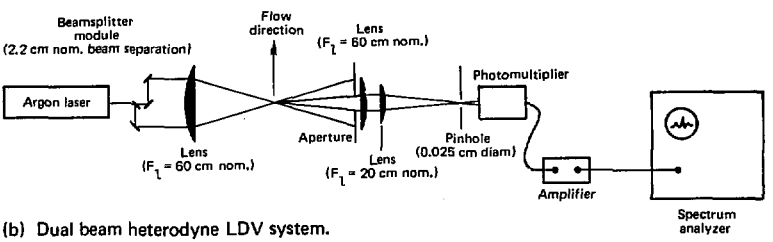

(b) Dual beam heterodyne LDV system.

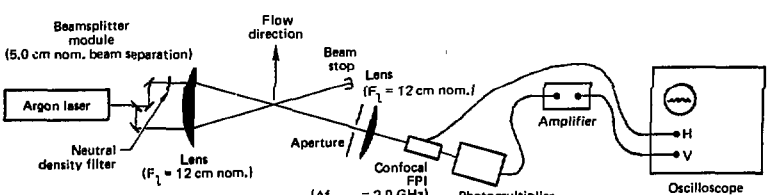

(c) Reference beam LDV-FPI system.

Figure 62. - Schematic representations of the different LDV arrangements compared for use for the high-velocity, liquid-dominated nozzle jet flow droplet velocity measurements.

Important results determined from these experimental comparisons were:

(1) At comparatively low droplet concentrations (light transmission > 70%), both the heterodyne arrangements required much less laser power (10 - 20 mW) than did the LDV-FPI arrangement (50 - 75 mW) for similar signal qualities.

(2) At moderate droplet concentrations (light transmission between 30% and 70%), the reference beam heterodyne system had a slightly better signal quality than did the dual beam heterodyne arrangement. However, the LDV-FPI system output signal was far superior in quality to either of the heterodyne techniques.

(3) At high droplet concentrations (light transmission < 30%), the Doppler frequency shift for both heterodyne techniques was completely obscured by noise. This noise was presumably caused by both the large velocity gradients and the large number of droplets within the measuring volume. This condition was virtually unaffected by changes in laser power. At this nozzle flow condition, the output signal of the LDV-FPI arrangement showed an increase in signal broadening (probably due to a wider droplet size spectrum and greater kinetic nonequilibrium effects). It was also more intense than those recorded previously. This indicated that there was more light available in the central bright fringe, probably due to the larger number of droplets scattering light to the interferometer.

Because of the favorable results obtained with the LDV-FPI arrangement for this series of qualitative experiments, a laser-Doppler velocimeter arrangement employing a scanning confocal Fabry-Perot interferometer was chosen to be used for the low-quality, steam-water nozzle jet flow measurements. The final LDV-FPI configuration utilized was not the reference beam arrangement previously described, but it was a modified dual beam backscatter optical system. This optical arrangement was chosen for its experimental simplicity in both measurement and alignment.

EXPERIMENTAL DUAL BEAM BACKSCATTER LDV-FPI SYSTEM

Experimental LDV System Optical Arrangement

Following the selection of the LDV-FPI arrangement as the system to be used for the droplet velocity measurements, it was determined that the forward scatter reference beam operational mode was too cumbersome for practical use at the nozzle test station. The unit for measuring forward scattered light required a critical alignment on each side of the nozzle exhaust chamber. This was difficult to achieve and maintain because of both the inaccessibility and the large environmental temperature excursions occuring during operation of the nozzle flow apparatus (10 C (50 F) to 100 C (212 F) environmental temperature range).

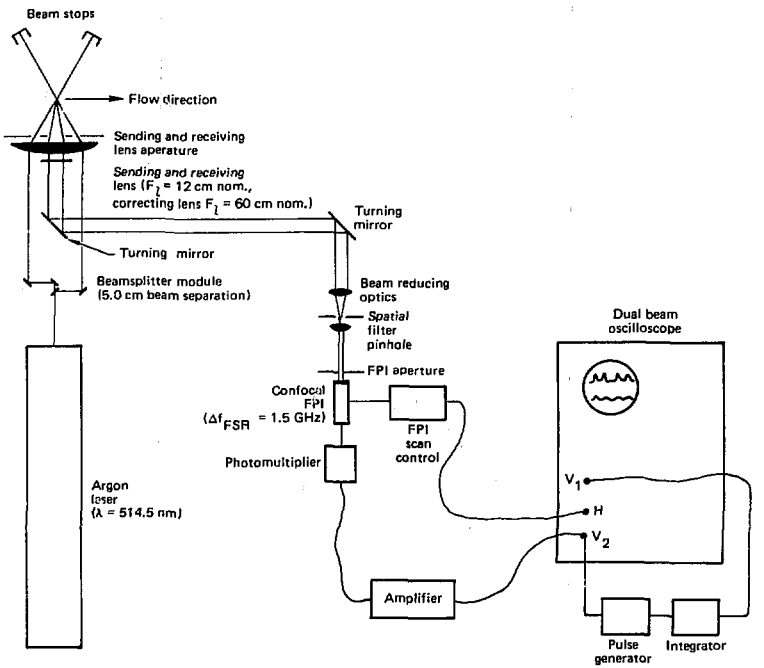

Figure 83. – Dual beam backscatter LDV–FPI optical and signal analysis arrangements used for the low-quality, steam-water nozzle jet flow measurements.

Because of these problems, a dual beam backscatter LDV optical arrangement using a scanning confocal FPI for signal analysis was developed. This optical arrangement, shown schematically in Figure 63, uses a sending optics arrangement identical to that of a dual beam heterodyne LDV system. The light beam from a single frequency argon laser (see references [113], [114]) is divided into two parallel identical beams, which are focused to an intersection point (measuring volume) in the flow. The light backscattered from droplets traveling through this intersection region is collected by the receiving lens and corrected for spherical aberrations by a second lens to collimate the light scattered from the measuring volume. This beam is then reduced in diameter and spatially filtered before being analyzed for the Doppler frequency shift using the confocal scanning FPI. The spatial filter pinhole in the backscattered light beam path can be used to insure that only radiation from the measuring volume is received. However, the spatial filter was not used for this work because it was found that through the proper adjustment of the spacing between the two lenses used for reducing the beam, the light scattered from flow locations other than the measuring volume could be caused to diverge, and an aperture located prior to the FPI entrance could be used to eliminate all but the nearly collimated light originating at the beam intersection region in the flow. This provided an optical arrangement that was very simple to align. The initial dual beam separation was 5.0 cm and the sending lens focal length was nominally 12.0 cm. This resulted in a beam crossing half angle of 12.65 degrees (this angle was accurately determined and

because of lens spherical aberrations it was different from that expected).

The dual beam backscatter LDV-FPI optical arrangement developed is unique in that a reference beam is not necessary to determine the Doppler frequency shift. This is because the dual beam LDV-FPI system utilizes light that has been scattered from two different beams at different angles with respect to the flow direction. The light scattered from one beam will have a higher frequency than that of the unscattered light, while the light scattered from the second beam will be lower in frequency. The difference in the frequency shifts between the two beams, when combined with the FSR characteristics of the FPI, provides all the necessary information for the Doppler frequency shift determination. The ease of alignment and the stability of this optical arrangement are greatly improved over those of other LDV-FPI optical arrangements because modular units can be readily utilized. Figure 64 is a photograph of the dual beam backscatter LDV-FPI unit showing the modular assembly, and Figure 65 is a photograph of it installed at the nozzle test station.

Theoretical Doppler Frequency Shift Analysis

The Doppler frequency shift of the light scattered from a moving particle can be analyzed for the dual beam backscatter LDV-FPI system using the beam intersection geometry shown in Figure 66. From equation (55), the Doppler frequency shift of the light scattered from

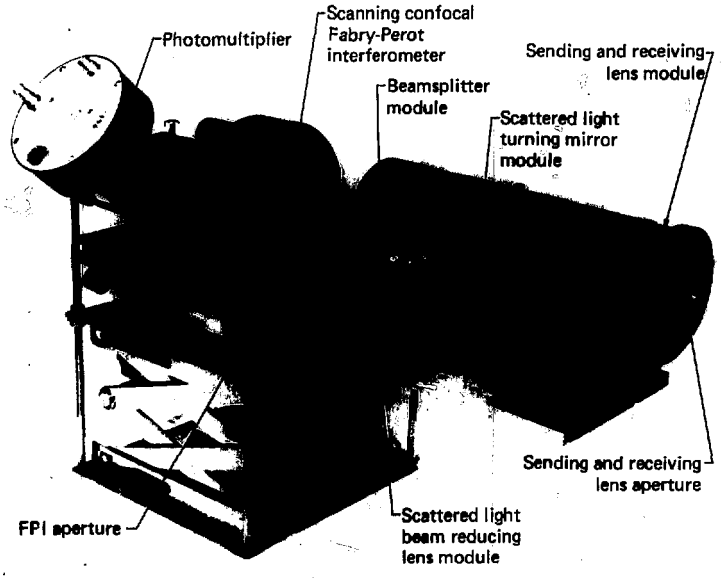

Figure 64. – Photograph of the dual beam backscatter LDV–FPI modular assembly.

Figure 65. - Photograph of the dual beam backscatter LDV-FPI unit installed at the nozzle test station.

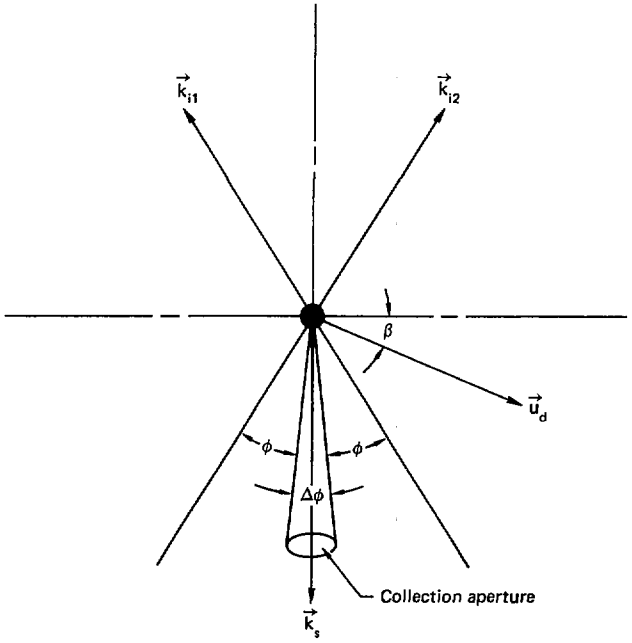

Figure 66. - Light scattering geometry for the dual beam backscatter LDV-FPI optical arrangement.

laser beam number 1 (incident from the forward direction) can be expressed in terms of the beam intersection and scattering geometry as

$$\Delta f_1 = \frac{u_d}{\lambda} [- \sin \beta \cos \varphi - \cos \beta \sin \varphi + \sin (\beta \pm \Delta\varphi)] \qquad (64)$$

Similarly, the Doppler frequency shift associated with the light scattered from beam number 2 (incident from the rearward direction) becomes

$$\Delta f_2 = \frac{u_d}{\lambda} [- \sin \beta \cos \varphi + \cos \beta \sin \varphi + \sin (\beta \pm \Delta\varphi)] \qquad (65)$$

Equations (64) and (65) each include a term that shows that the Doppler frequency shift in the light scattered from each beam can be broadened by the physical size of the scattered light receiving aperture. This measurement error is called aperture broadening and is due to the finite included angle, $\Delta\varphi$, of the receiving lens aperture. It can be seen that large aperture sizes (large $\Delta\varphi$) can introduce significant errors into the measured frequency of the light scattered from either of the incident laser beams.

Defining the total Doppler frequency shift of the dual beam FPI system as the difference between the Doppler frequency shift of the scattered light from each of the two focused laser beams results in the equation

$$\Delta f = \Delta f_2 - \Delta f_1 = \frac{2u_d}{\lambda} \sin \varphi \cos \beta \qquad (66)$$

This equation reduces to that presented for the forward scattering arrangements of Figure 59 (see equation (61)) when the optical system is

aligned perpendicular to the droplet velocity vector (β = 0 degrees). This equation is an important result in that it indicates that the mean droplet velocity can be obtained using a dual beam LDV-FPI system without the complication of a reference beam signal. This fact greatly simplifies the backscatter optical arrangement which enhances the optical alignment ease and stability. Also, equation (66) shows both that aperature broadening errors are nonexistant for this arrangement and that a reasonable amount of alignment error can be tolerated without significant measurement error (e. g., an error of < 1% is introduced for $\beta \leq 8$ degrees).

Experimental Doppler Frequency Shift Determination

The electronic signal obtained using the LDV-FPI optical arrangement was analyzed using two different methods, each yielding different information. The electronic signal analysis equipment used is shown schematically in Figure 63. The first method of signal analysis was to record the local photomultiplier signal amplitude as a function of FPI mirror spacing using an oscilloscope. The sawtooth voltage profile from the oscilloscope horizontal sweep was used to drive the piezoelectric crystals of the FPI. As shown by equation (31), the local photomultiplier voltage output is a function of the droplet diameter multiplied by the number of droplets scattering light per unit size range and integrated over all droplet sizes (for a constant scattering angle and light wavelength). Although it is not possible to separate droplet size and number density effects, the peak of the local

photomultiplier output voltage will occur at a droplet size greater than the maximum of the droplet size distribution.

The second method of LDV-FPI signal analysis used provided a display of the droplet number rate versus velocity. This was accomplished by converting each pulse from the photomultiplier, irrespective of its amplitude above a preset voltage, into a constant amplitude pulse using a pulse generator. This train of constant amplitude pulses from the pulse generator was then summed using an integrator prior to its display using an oscilloscope.

The combination of these two signal analysis techniques was used by Morse, et. al., [8], along with a numerical two-phase flow prediction method to determine particle size and velocity in two-phase rocket nozzle jet flows. As described previously, the local photomultiplier signal amplitude trace is proportional to both the droplet size and the droplet number in the measuring volume. The integrated pulse generator output is proportional only to the droplet number. Thus, from a comparison of the spatial location of the peaks in the two oscilloscope traces, a qualitative measure of the droplet size distribution function width can be obtained, i. e., the more horizontal separation between the peaks of the droplet number rate trace and and the photomultiplier voltage output trace, the greater the width (or multimodal nature) of the droplet size distribution function. These analyses cannot be combined to yield the droplet size directly, however, because of the

$$u_d = \left(\frac{t_2}{t_1}\right)\left(\frac{\Delta f_{FSR}\lambda}{2 \sin \phi}\right) = 600 \text{ m/s}$$

$\Delta f_{FSR} = 1.5$ GHz

$\lambda = 514.5$ nm

$\phi = 12.65$ degrees

Figure 67. - Photograph of a typical oscilloscope trace for the dual beam backscatter LDV-FPI system. The upper trace yields the mean droplet number rate velocity, and the lower trace yields the mean photomultiplier signal amplitude velocity.

many other experimental unknowns that influence this measurement (see the discussion presented by Morse, et. al. [8] concerning this subject).

A photograph of a typical dual beam oscilloscope trace using these two signal analysis methods is shown in Figure 67. The upper trace presents the local integrated pulse generator output and the lower trace shows the local photomultiplier voltage output. The horizontal spread or width of the curves is due to the fact that the droplets in the measuring volume have a velocity distribution. Note the near coincidence in the peak locations in the two different scans. This indicates that the droplet size distribution function is narrow.

The pulse rate counter (integrator) functions by accumulating the output pulses of the pulse generator on a capacitor which is continually discharged by a resistor. In this manner, the capacitor voltage is a measure of the pulse rate averaged over the integration time. Denoting τ_R as the response or integration time and R_D as the rate of detected signal pulses, the output voltage is proportional to $R_D\tau_R$, which has a statistical fluctuation with a standard deviation of $(R_D\tau_R)^{1/2}$ [110]. Since the relative standard deviation due to a finite count rate is proportional to $(R_D\tau_R)^{-1/2}$, τ_R should be made large. However, to avoid degradation in the velocity resolution the response time cannot exceed the time, T_{FSR}/F (T_{FSR} is the sweep period of the FPI and F is the finesse). For the conditions of Table 1 and for 2 μm diameter droplets, the count rate is near 2.5 X 10^7 counts/s. The finesse of the FPI used was near 100 and for a convenient FSR sweep rate of approximately 1 s,

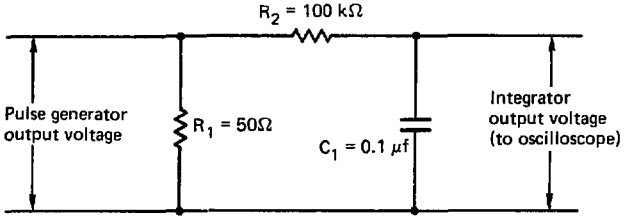

Figure 68. - Schematic of the circuit used for integrating the pulse train from the pulse generator.

the integration time, τ_R, was set at 10 ms. These values yield a standard deviation in the count rate of 0.2%. The integrator circuit used for this work is shown in Figure 68.

The FPI scan control unit of Figure 63 was constructed to provide better resolution of the Doppler frequency shift information. The oscilloscope sawtooth voltage was approximately 150 volts, but the FPI required only 40 volts per FSR scan. Thus, using the sawtooth voltage directly resulted with nearly four FSR scans per oscilloscope sweep. To reduce the voltage at the FPI for better data resolution while maintaining synchronization with the horizontal oscilloscope sweep resulted in the FPI scan control circuit shown in Figure 69. In this circuit, potentiometer number 1 controls the constant voltage bias applied to the FPI, and potentiometer number 2 regulates the voltage differential applied to the FPI per oscilloscope sweep. The use of this control regulates both the number of FSR's to be scanned per oscilloscope sweep and the oscilloscope sweep position where the FPI FSR scan is to begin.

EXPERIMENTAL TWO-PHASE NOZZLE JET FLOW DROPLET VELOCITY MEASUREMENTS

As discussed previously, calculations using 1D2FAZEQ and 1D2FAZNEQ indicated that droplet velocity differences in the nozzle jet flow due to droplet size changes were much too small for accurate determination of the droplet size through a comparison between the calculated and measured droplet velocities (see reference [58]). Because of this, the

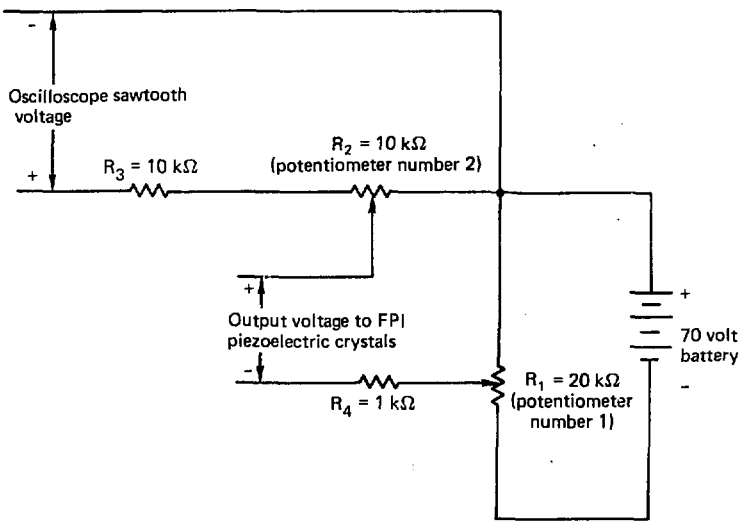

Figure 69. - Schematic of the FPI scan control circuit. Potentiometer number 1 controls the position of the FPI scan on the oscilloscope sweep, and potentiometer number 2 controls the number of FSR's to be scanned per oscilloscope sweep.

droplet velocity measurements obtained during this work were made to complement the light scattering droplet size distribution measurements.

During the initial experimental nozzle design, questions arose concerning the minimum nozzle thickness allowable while avoiding severe boundary layer effects. A very thin nozzle jet flow was necessary to obtain the required light transmission for the light scattering experiments. However, the conditions existing in large cross-section jet flows would yield information more representative of actual turbine nozzle operating conditions because of the smaller boundary layer and wall liquid film flow perturbations. To resolve this question concerning the nozzle operation and to demonstrate experimentally the spatial resolution of the dual beam LDV-FPI arrangement, droplet velocity profiles through the nozzle jet thickness were measured using nozzle number 3 at two different operating conditions. These velocity profiles are shown in Figure 70. The operating conditions at which these data were taken are listed in the figure. The velocities presented in this figure correspond to mean number rate droplet velocities, and thus, are the velocities corresponding to the greatest number of droplets in the flow. Droplet velocities determined from the photomultiplier voltage output differed from these velocities by about 5%, and were therefore not included. The small differences between these two velocities and the near coincidence of the peaks of the photomultiplier voltage output and the integrated pulse generator output on the oscilloscope traces (see example shown in Figure 67) confirms the narrow droplet size distribution functions presented previously.

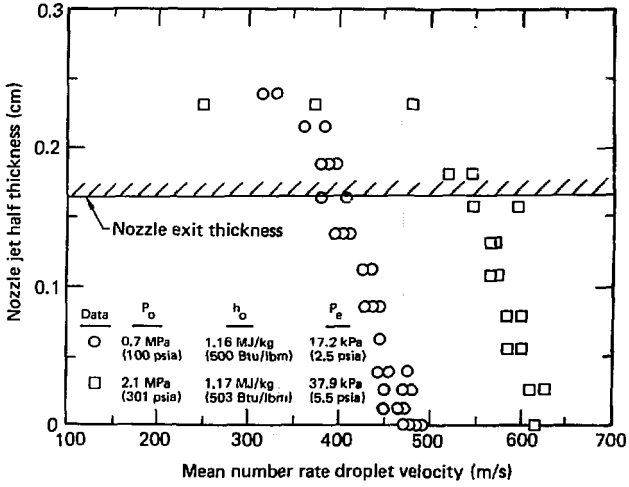

Figure 70. – Mean number rate velocity measurements across the jet flow half thickness.

A comparison of the velocity profiles of Figure 70 shows that there is little change in the basic profile due to the change in the inlet pressure. This indicates that the boundary layer effects are essentially the same in either case. A closer inspection of the two profiles shows a difference of approximately 100 m/s (328 ft/s) in the velocities of the two cases. However, a calculation based on isentropic, homogeneous flow indicates that the two velocities should be nearly the same (approximately 600 m/s (1969 ft/s)). An analysis of the pressure profiles for the two cases shows that for the velocity profile corresponding to the 2.1 MPa (300 psia) inlet pressure (exhaust pressure of 37.9 kPa (5.5 psia)) the nozzle was operating underexpanded, and for the velocity profile corresponding to the 0.7 MPa (100 psia) inlet pressure (exhaust pressure of 17.2 kPa (2.5 psia)) the nozzle was operating overexpanded. Overexpanded operation will cause an oblique shock to form in the nozzle jet flow. This could cause a velocity decrease before the fluid reached the measurement location 1.0 cm from the nozzle exit.

The maximum distance from the nozzle exit at which the oblique shocks would completely cross the jet flow (one shock originating at each sidewall) can be estimated. This estimation can be made because the velocity normal to an oblique shock wave must be greater than or equal to the local sonic velocity of the fluid. For a local two-phase sonic velocity of 230 m/s (755 ft/s) and a nozzle exhaust velocity of 600 m/s (1969 ft/s), the minimum angle that an oblique shock could form (at a sonic normal velocity) with respect to the nozzle axis is 22.5

degrees. Using this value indicates that the oblique shocks from each of the two nozzle sidewalls will intersect at a distance $\leq$ 0.4 cm from the nozzle exit (because of the 0.325 cm thick jet flow). Because this distance is less than the distance to the velocity measurement location and because the two-phase oblique shock calculations of Comfort [4] indicate that the velocity loss for similar oblique shock conditions was approximately 100 m/s (328 ft/s), the difference in velocities between the two measured velocity profiles of Figure 70 appears to be caused by overexpanded nozzle operation for the 0.7 MPa (100 psia) inlet pressure conditions. Further measurements determined that for underexpanded nozzle operation at an inlet pressure of 0.7 MPa (100 psia), exhaust velocities near 600 m/s (1969 ft/s) were obtained. Since this velocity is very near that calculated for the vapor velocity using 1D2FAZEQ, it confirms the small droplet sizes measured using the scattered light intensity profile matching technique presented previously. The large velocity difference obtained for the measurements of Figure 70 suggests that underexpanded nozzle operation should be maintained for velocity measurements in thin two-phase nozzle jet flows.

Although the velocity measurements of Figure 70 are for a 0.325 cm jet thickness, the LDV-FPI system was found to allow measurements in much thicker nozzle jet flows. Velocity measurements in two-phase, air-water nozzle jet flows with light transmission characteristics similar to the steam-water nozzle flows have shown that the dual beam backscatter LDV-FPI arrangement was capable of measuring droplet velocities at depths up to 0.6 cm into the flow. This capability will

allow free-stream velocity measurements to be obtained using large cross-section two-phase nozzles.

The mean number rate velocity variation as a function of the vertical distance from the nozzle jet centerline is shown for two different nozzle inlet pressures in Figure 71. The measurement location was maintained at the jet thickness centerline for all the measurements. The nozzle operating conditions at which these data were taken are listed on the figure. Again, because the nozzle was operated overexpanded during these tests, the measured velocities are consistantly low. Examination of this figure shows very little droplet velocity spatial variation. This indicates that the droplet size change over the jet height is small, which substantiates the assumption of a constant mean specific droplet cross section used previously to obtain the droplet volume fraction spatial variation shown in Figure 52.

There were several possible sources of error involved in the droplet velocity measurements, with the largest error resulting from the peak to peak distance (time) measurements from the oscilloscope traces. Inclusion of all the errors indicates that droplet velocity measurement accuracies of better than ±3% can routinely be expected. The accuracy and data rate capability of this LDV-FPI system could be substantially improved by electronically determining the peak to peak times directly from the oscilloscope input voltages.

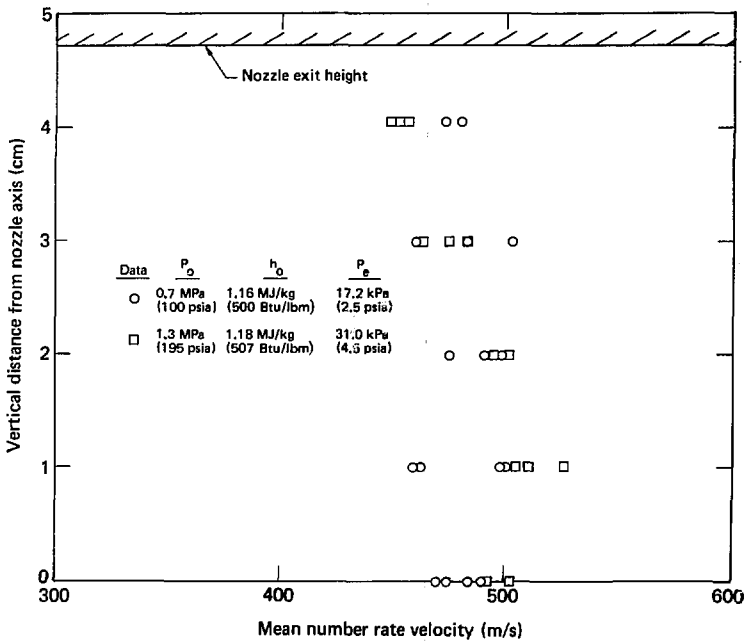

Figure 71. - Spatial variation of the droplet number rate velocity across the nozzle jet flow half height. The low velocities are a result of overexpanded nozzle operation.

SUMMARY AND CONCLUSIONS

1) A new method for the determination of small particle size distributions in a thin two-phase nozzle jet flow using a light scattering technique was developed. The experimental technique is based upon the simultaneous single scattering of light from many particles. The size distribution inversion method involves matching the measured scattered light intensity profile with a summation from the intensity contributions of a series of appropriately spaced narrow band size distribution functions. A numerical optimization procedure is used to determine the strengths of the individual bands which yield the best agreement with the measured scattered light intensity profile. The narrow band intensity contributions are calculated using exact Mie theory.

2) Numerical experiments indicated that the narrow band size distribution inversion method has the capability to invert a wide range of different size distribution functions. Examples are presented for the numerical inversion of a narrow monomodal size distribution function, a broad monomodal size distribution function and a broad bimodal size distribution function. This size distribution inversion method can be important for the understanding of two-phase nozzle flows because of its capability for determining the complex size distribution functions that may be present.

3) A scattered light collecting optics arrangement consisting of two 60 cm focal length lenses was utilized to avoid spherical aberrations for the larger scattering angles and the finite measuring volumes required for measurements of the small droplet sizes present in the two-phase nozzle jet flows. The use of this optical system (including the film calibration and analysis procedure) for scattered light measurements was demonstrated using a glass beads-in-water polydispersion.

4) Experimental measurements of the droplet size distribution in liquid-dominated, steam-water nozzle jet flows were accomplished for nozzles operating at a constant inlet enthalpy of 1.16 MJ/kg (500 Btu/lbm) and inlet pressures between 0.7 MPa (100 psia) and 1.4 MPa (200 psia). The effect of variations in the nozzle throat geometry (i. e., throat radii of curvature of 0.051 cm, 0.318 cm and 2.540 cm and throat heights of 0.318 cm and 0.635 cm) and inlet pressure upon the droplet size distribution in the nozzle jet flow was investigated. For the nozzle geometry and inlet conditions tested, the nominal modal droplet diameter was 0.5 μm, the nominal Sauter mean droplet diameter was 1.7 μm and the nominal mass mean droplet diameter was 2.4 μm. These measured mean droplet diameters were significantly smaller than those calculated using either the thermal equilibrium or the thermal nonequilibrium numerical models (i. e., predicted diameters consistantly near 7.5 μm), which indicates a need for a better understanding of droplet breakup mechanisms. No measureable change in the nozzle jet flow droplet size distribution was observed for either the nozzle throat

geometry or the inlet condition variations tested. This indicates that neither type of variation has a significant influence on the nozzle exit droplet size for the small measured droplet diameters present (droplet diameter changes less than approximately ±20% (±0.4 μm for a 2.0 μm diameter droplet) could not be detected for these small droplet sizes because of experimental errors).

5) Numerical predictions of the nozzle flow using; 1) a one-dimensional thermal equilibrium model (1D2FAZEQ) and 2) the same computer program modified to include thermal nonequilibrium effects (1D2FAZNEQ) consistantly yielded nozzle exit droplet diameters near 7.5 μm. Variations in nozzle throat geometry (i. e., throat radii of curvature of 2.540 cm, 1.270 cm and 0.318 cm and throat heights of 0.635 cm and 0.318 cm) yielded predicted nozzle exit droplet diameter changes near ±0.9 μm (see Figure 8 for the nozzle operating conditions and the predicted droplet diameter results). Experimental measurements determined that the nominal nozzle exit droplet diameter was significantly smaller than the near 7.5 μm predicted droplet diameter (i. e., the measured nominal mass mean droplet diameter was near 2.4 μm). However, from the droplet size distribution measurements, the predicted droplet diameter was seen to be reasonably consistant with the maximum stable droplet diameter existing in the nozzle jet flow. These results suggest that an appropriate critical Weber number (using 1D2FAZEQ) for this flow should be near 1.0, rather than the value of 6.0 currently in use. The inclusion of this value into the calculational

model allows the entire droplet phase characteristics to be calculated more accurately throughout the entire nozzle flow.

6) Flow separation occurred in the nozzle incorporating the smallest throat radius of curvature and throat height combination, nozzle number 5 ($R^* = 0.051$ cm and $y^* = 0.318$ cm), at a location near the nozzle throat. This conclusion is based upon the observed shift in the measured nondimensional pressure versus area profile. The flow separation region was very small and was probably due to the small throat radius of curvature and the large expansion angle combination. The effect of the flow separation was such that it could only be detected when using the very small throat height nozzle number 5 (the flow separation region was too small for its effect to be noticed during the operation of nozzle number 2 ($R^* = 0.051$ cm and $y^* = 0.635$ cm) because of its much larger throat height). This result suggests that for applications using two-phase nozzles the throat radius of curvature should be maintained greater than 0.051 cm to avoid nozzle performance degradation due to flow separation.

7) The spatial variation of the droplet volume fraction across the height of the nozzle jet flow was determined using light transmission measurements in combination with spatial uniformity results from the droplet size distribution and droplet velocity measurements. These measurements indicate that the droplet volume fraction is a factor of 1.1 greater than the predicted one-dimensional, homogeneous droplet volume fraction at the jet flow centerline. Furthermore, the profile is

constant at this value until a vertical location greater than one half the distance from the jet centerline to the top of the jet is reached. Beyond this point, the relative droplet volume fraction decreases until a ratio near 0.7 is reached at the top edge of the jet flow. The droplet phase is much more uniformly distributed in this flow than the particulate phase was found to be distributed in gas-particle nozzle flows, but it is consistant with the droplet phase spatial distrioutions measured in high-quality nozzle flows.

8) The light transmission measurements were also utilized to confirm the Sauter mean droplet diameter measured using the scattered light intensity profile matching method. The Sauter mean diameter obtained from light transmission measurements was near 2.0 μm. This is very near the average Sauter mean droplet diameter of 1.7 μm (18% difference) that was obtained from an integration of the measured droplet size distribution.

9) A pulsed ruby laser shadowgraph arrangement was used to obtain near stop-action photographs of the spatial variation of the droplet phase within the complete nozzle flowfield using transparent sidewalled nozzles. The system was used to photograph the flow patterns in the nozzle inlet and throat regions, the droplet flow channeling throughout the entire nozzle and the two-phase boundary layer separation and shock wave flow phenomena. From photographs of the nozzle inlet and throat regions, it was concluded that the large particle flow channeling could be eliminated and the droplet size reduced in general by a phase

separation before the nozzle inlet and a proper phase remix arrangement near the nozzle throat. This could enhance droplet phase spatial uniformity and create high relative phase velocity and temperature differences conducive to droplet breakup.

10) A new laser-Doppler velocimeter arrangement was developed to determine the droplet velocity in high-velocity, high droplet concentration, two-phase nozzle jet flows. Several different LDV arrangements were investigated, but the methods employing direct optical signal analysis (using a scanning confocal Fabry-Perot interferometer) of the Doppler frequency shift were found to be the most useful. The optical arrangement developed for this study was that of a dual beam backscatter LDV-FPI, for which the difference in frequency between the light scattered from each laser beam provides the Doppler frequency shift information. In this manner, a reference beam signal is not required, and the optical alignment ease and stability is enhanced over other LDV-FPI arrangements because modular optical assembly can be readily utilized.

11) The dual beam backscatter LDV-FPI arrangement was utilized to measure droplet velocities in the two-phase, steam-water nozzle jet flows. Velocity profiles were measured across the thickness of the nozzle jet flow. These measurements demonstrated the spatial resolution of the LDV-FPI arrangement, and they also determined that the boundary layer effects for the thin cross-section nozzle flows were not sufficient to modify the maximum velocity at the nozzle exit. Maximum

velocities near 600 m/s (1969 ft/s) were measured at the nozzle exit, corresponding very closely to the vapor exhaust velocity calculated using both 1D2FAZEQ and 1D2FAZNEQ. This confirms the droplet size measurements in that the droplet sizes must be ≤ 4 μm in diameter for such small relative velocities to occur.

12) Thin two-phase nozzles must be operated underexpanded when measuring droplet velocities in the nozzle exhaust flow to avoid velocity measurement errors due to oblique shocks at the exit. Another method for avoiding oblique shock measurement errors is to determine the droplet velocity directly in large cross-section two-phase nozzles. This avoids velocity measurement errors by allowing the LDV measurement volume to be positioned in the flow ahead of the oblique shock. Measurements in two-phase, air-water nozzle jet flows with similar light transmission characteristics as the steam-water nozzle flows demonstrated that velocity measurements could be obtained (using the dual beam backscatter LDV-FPI arrangement) at a depth up to 0.6 cm into the flow. This is sufficient to allow free-stream droplet velocity measurements in large cross-section nozzles while avoiding oblique shock induced measurement errors.

13) The measured spatial variation in the droplet phase velocity across the nozzle jet height was small. This indicates that the spatial variation of the droplet size is small, and it supports the small variations in the droplet volume fraction that were determined from the light transmission measurements.

14) In general, the measured droplet size in the nozzle jet flow (measured nominal mass mean droplet diameter of 2.4 μm) was not less than the 2.2 μm maximum droplet diameter necessary for a turbine performance increase with the experimental impulse blading geometry of reference [4] (see Figure 1). This result confirms the conclusion presented in reference [4] that the nozzle exit droplet diameter was greater than 2.2 μm for the impulse turbine experiments. However, with the measured droplet size distribution function information obtained for this study and the calculational technique of reference [4], it should be possible to achieve a significant increase in turbine performance by the design of a wheel with longer chord blades for wider blade spacing (see Figure 2).

RECOMMENDATIONS FOR FUTURE WORK

Because of the strong dependence of two-phase impulse turbine efficiency on nozzle exit droplet size, it is essential that further work on both the mechanisms governing and the methods for predicting droplet breakup in single-component, two-phase nozzle flows be undertaken. The proposal for a controlled phase remixing in the nozzle throat region to increase the kinetic and thermal nonequilibrium effects and to eliminate droplet channeling and droplet impact on the nozzle converging walls, both for increased droplet breakup, should be pursued. Measurements of the droplet phase characteristics throughout the entire nozzle, and especially in the nozzle throat region, should be made. These measurements would provide valuable information about the droplet breakup mechanisms within this type of flow. Droplet characteristics measurements as a function of the liquid phase fraction, with application to very low-quality turbine inlet conditions, should also be made. This would yield information pertinent to waste and solar heat energy conversion processes. Further research concerning the basic droplet breakup mechanisms, i. e., whether kinetic or thermal nonequilibrium breakup dominates, should also be considered. In these studies, measurements of the effect of a high interphase mass transfer rate on the droplet surface tension should be included.

Further development of the droplet phase characteristics measurement techniques is also needed. Studies of the effects of multiple scattering on the scattered light intensity profile from small

particle dispersions would be desireable. A method is needed for droplet size measurements in large cross-section nozzle flows with comparable or higher droplet concentrations. Refinements in both the light scattering droplet size distribution measurement and the LDV droplet velocity measurement methods should be accomplished to increase their speed and accuracy. A magnetic tape - minicomputer arrangement could be interfaced with a photosensor array to provide on-line droplet size distribution information. This arrangement would allow many tests to be accomplished in a short period of time and could possibly be used for time resolved measurements. Similarly, the output from the LDV system could be analyzed using a minicomputer system to provide on-line information and to increase the data rate and the measurement accuracy.

The design of advanced two-phase impulse turbines (nozzle and blade contours) requires the development of improved calculational models. Multi-dimensional, two-phase calculational methods which include experimentally derived droplet breakup information should be developed. Information concerning two-phase boundary layer behavior and two-phase shock phenomena is also of importance to advance the design and calculational methods. The behavior of these complex flow situations is virtually unknown at the present time.

REFERENCES

[1] - Austin, A. L., Higgins, G. H., and Howard, J. H., "The Total Flow Concept for Recovery of Energy from Geothermal Hot Brine Deposits", UCRL-51366, Lawrence Livermore Laboratory, Livermore, California, Apr. 1973.

[2] - Austin, A. L. and Lundberg, A. W., "A Comparison of Methods for Electric Power Generation from Geothermal Hot Water Deposits", ASME Paper No. 74-WA/ENER-10, Nov. 1974.

[3] - Austin, A. L., "Prospects for Advances in Energy Conversion Technologies for Geothermal Energy Development", Proceedings of the Second United Nations Symposium on the Development and Use of Geothermal Resources, Vol. 3, May 1975.

[4] - Comfort, W. J., "The Design and Evaluation of a Two-Phase Turbine for Low-Quality Steam-Water Mixtures", D. Eng. Thesis, University of California at Davis, Davis, California, May 1977.

[5] - Hoglund, R. F., "Recent Advances in Gas-Particle Nozzle Flows", ARS Journ., Vol. 32, No. 5, May 1962.

[6] - Gilbert, M., Allport, J., and Dunlap, R., "Dynamics of Two-Phase Flow in Rocket Nozzles", ARS Journ., Vol. 32, No. 12, Dec. 1962.

[7] - United Technology Center, "Dynamics of Two-Phase Flow in Rocket Nozzles", Final Report, Contract No. NOw-64-0506-c, UTC-2102-FR, Sept. 1965.

[8] - Morse, H. L., Tullis, B. J., Seifert, H. S., and Babcock, W., "Development of a Laser-Doppler Particle Sensor for the Measurement of Velocities in Rocket Exhausts", Journ. of Spacecraft and Rockets, Vol. 6, No. 3, Mar. 1969.

[9] - Warda, H. A., Mobbs, F. R., and Cole, B. N., "Gas-Solids Flow in Supersonic Nozzles", ASME Paper No. 75-WA/HT-35, Dec. 1975.

[10] - Hoffman, J. D., "An Analysis of the Effects of Gas-Particle Mixtures on the Performance of Rocket Nozzles", Jet Propulsion Center Report No. TM-63-1, JPC-348, Purdue University, Lafayette, Ind., Jan. 1963.

[11] - Hoffman, J. D. and Lorenc, S. A., "A Parametric Study of Gas-Particle Flows in Conical Nozzles", AIAA Journ., Vol. 3, No. 1, Jan. 1965.

[12] - Marble, F. E., "Nozzle Contours for Minimum Particle-Lag Loss", AIAA Journ., Vol. 1, No. 12, Dec. 1963.

[13] - Hoffman, J. D. and Thompson, H. D., "Optimum Thrust-Nozzle Contours for Gas-Particle Flows", AIAA Journ., Vol. 5, No. 10, Oct. 1967.

[14] - Hoffman, J. D. and Thompson, H. D., "A General Method for Determining Optimum Thrust Nozzle Contours for Gas-Particle Flows", AIAA Paper No. 66-536, June 1966.

[15] - Elliott, D. G. and Weinberg, E., "Acceleration of Liquids in Two-Phase Nozzles", NASA TR-32-987, July 1968.

[16] - Wallis, G. B. and Sullivan, D. A., "Two-Phase Air-Water Nozzle Flow", ASME Journ. Basic Eng., Dec. 1972.

[17] - Carofano, G. C., "An Analytical and Experimental Study of the Flow of Air-Water and Steam-Water Mixtures in a Converging-Diverging Nozzle", Ph. D. Thesis, Cornell University, Ithaca, New York, June 1968.

[18] - Cunningham, R. G., "Gas Compression with the Liquid Jet Pump", ASME Journ. Fluids Eng., Sept. 1974.

[19] - Pchelkin, I. M., Kalakutskaya, N. A., and Parfent'eva, I. F., "Effect of the Length and Geometry of a Laval Nozzle on the Expansion of a Water-Air Mixture", Heat Transf. Sov. Res., Vol. 4, No. 5, Sept. - Oct. 1972.

[20] - Elliott, D. G., "Investigation of a Gas-Driven Jet Pump for Rocket Engines", Progress in Astronautics and Rocketry, Vol. 2, L. E. Bollinger, M. Goldsmith, and A. W. Lemmon Ed., Academic Press, New York, 1960.

[21] - Netzer, D. W., "Calculations of Flow Characteristics for Two-Phase Flow in Annular Converging-Diverging Nozzles", Jet Propulsion Center Report No. TM-62-3, JPC-305, Purdue University, Lafayette, Indiana, June 1962.

[22] - Chigier, N. A., "The Atomization and Burning of Liquid Fuel Sprays", Prog. Energy Combust. Sci., Vol. 2, No. 2, 1976.

[23] - Rizkalla, A. A. and Lefevbre, A. H., "The Influence of Air and Liquid Properties on Airblast Atomization", ASME Journ. Fluids Eng., Sept. 1975.

[24] - Buschulte, W., "Liquid Propellant Atomization by Injector Elements and its Effect on Combustion Chamber Efficiency", Israel Journ. Tech., Vol. 12, No. 1, 1974.

[25] - Maxwell, T. T., Maples, G., and Dyer, D. F., "Thrust of an Air-Augmented Waterjet with a Converging-Diverging Nozzle", Journ. Hydronautics, Vol. 9, No. 4, Oct. 1975.

[26] - Yellott, J. I., "Supersaturated Steam", Trans. ASME, Vol. 56, 1934.

[27] - Yellott, J. I. and Holland, C. K., "The Condensation of Flowing Steam; Part I - Condensation in Diverging Nozzles", Trans. ASME, Vol. 59, 1937.

[28] - Lee, Y. J., Fourney, M. E., and Moulton, R. W., "Determination of Slip Ratios in Air-Water Two-Phase Critical Flow at High Quality Levels Utilizing Holographic Techniques", AIChE Journ., Vol. 20, No. 2, Mar. 1974.

[29] - Moore, M. J. and Sieverding, C. H., Two-Phase Steam Flow in Turbines and Separators, Hemisphere Publishing Corp., Washington, 1976.

[30] - "Condensation in High-Speed Flows", A. A. Pouring Ed., American Society of Mechanical Engineers, New York, 1977.

[31] - Gadbois, S. E., "Droplet Studies in Supersonic Two-Phase Steam Flow with Normal Shocks", Ph. D. Thesis, University of Connecticut, Storrs, Connecticut, 1965.

[32] - Deich, M. E., Tsiklauri, G. V., Shanin, V. K., and Danilin, V. S., "Investigation of Flows of Wet Steam in Nozzles", High Temp., Vol. 10, No. 1, Jan. - Feb. 1972.

[33] - Deich, M. E., Danilin, V. S., Shanin, V. N., and Tsiklauri, G. V., "Critical Conditions in Laval Nozzles Operating in a Two-Phase Medium", Thermal Eng., Vol. 16, No. 6, 1969.

[34] - Starkman, E. S., Schrock, V. E., Neusen, K. F., and Maneely, D. J., "Expansion of a Very Low Quality Two-Phase Fluid Through a Convergent-Divergent Nozzle", ASME Journ. Basic Eng., June 1964.

[35] - Henry, R. E. and Fauske, H. K., "The Two-Phase Critical Flow of One-Component Mixtures in Nozzles, Orifices, and Short Tubes", ASME Journ. Heat Transf., May 1971.

[36] - Henry, R. E., "A Study of One- and Two-Component, Two-Phase Critical Flows at Low Qualities", ANL-7430, Argonne National Laboratory, Chicago, Illinois, Mar. 1968.

[37] - Deich, M. E., Danilin, V. S., Tsiklauri, G. V., and Shanin, V. K., "Investigation of the Flow of Wet Steam in Axisymmetric Laval Nozzles over a Wide Range of Moisture Content", High Temp., Vol. 7, No. 2, Mar. - Apr. 1969.

[38] - Teplov, S. V., Vartazarov, I. S., Dzhamardzhashvili, V. A., Zheltova, G. M., Mukhin, V. A., and Pakhorskii, V. A., "Results of Testing Laval Nozzles of Differing Flow-Section Length with a Vapor-Water Mixture", Heat Transf. Sov. Res., Vol. 4, No. 5, Sept. - Oct. 1972.

[39] - Adachi, H. and Yamamoto, N., "High Speed Two-Phase Flow, (II) Flashing Flow Through a Converging-Diverging Nozzle", Heat Transf. *Japanese Res.*, Vol. 3, No. 4, 1974.

[40] - Alger, T. W., "Performance of Two-Phase Nozzles for Total Flow Geothermal Impulse Turbines", Proceedings of the Second United Nations Symposium on the Development and Use of Geothermal Resources, Vol. 3, May 1975.

[41] - Hewitt, G. F. and Boure', J. A., "Some Recent Results and Developments in Gas-Liquid Flow : A Review", Int. Journ. Multiphase Flow, Vol. 1, No. 1, Oct. 1973.

[42] - Jones, O. C. and Delhaye, J. M., "Transient and Statistical Measurement Techniques for Two-Phase Flows : A Critical Review", Int. Journ. Multiphase Flow, Vol. 3, No. 2, Dec. 1976.

[43] - Comfort, W. J., Alger, T. W., Giedt, W. H., and Crowe, C. T., "Calculation of Two-Phase Dispersed Droplet-in-Vapor Flows Including Normal Shock Waves", ASME Paper No. 76-WA/FE-31, Dec. 1976.

[44] - Crowe, C. T. and Comfort, W. J., "Atomization Mechanisms in Single-Component, Two-Phase, Nozzle Flows", Proceedings of the First International Conference on Liquid Atomization and Spray Systems, Aug. 1978.

[45] - Mie, G., "Contributions to the Optics of a Turbid Media, Especially Colloidal Metal Solutions", Ann. Physik., Vol. 25, No. 3, 1908.

[46] - Asano, S. and Yamamoto, G., "Light Scattering by a Spheroidal Particle", Applied Optics, Vol. 14, No. 1, Jan. 1975.

[47] - Dobbins, R. A., Crocco, L., and Glassman, I., "Measurement of Mean Particle Sizes of Sprays from Diffractively Scattered Light", AIAA Journ., Vol. 1, No. 8, Aug. 1963.

[48] - Graber, M. and Cohen, A., "Multiple Scattering: Theoretical Calculations Compared with Experimental Dye-Laser Measurements", Journ. Opt. Soc. Am., Vol. 65, No. 11, Nov. 1975.

[49] - van de Hulst, H. C., Light Scattering by Small Particles, Second Ed., Wiley, New York, 1957.

[50] - Hinze, J, O., "Fundamentals of the Hydrodynamic Mechanism of Splitting in Dispersion Processes", AIChE Journ., Vol. 1, No. 3, Sept. 1955.

[51] - Lane, W. R., "Shatter of Drops in Streams of Air", Ind. Eng. Chem., Vol. 43, June 1951.

[52] - Rabin, E., Schallenmuller, A. R., and Lawhead, R. B., "Displacement and Shattering of Propellant Droplets", Air Force Office of Scientific Research, TR-60-75, R-2431, Mar. 1960.

[53] - Peskin, R. L. and Lawler, J. P., "Theoretical Studies of Mechanisms in Atomization of Liquids", Trans. Am. Soc. Htg. Air Cond. Eng., Vol. 69, 1963.

[54] - Loparev, V. P., "Experimental Investigation of the Atomization of Drops of Liquid Under Conditions of a Gradual Rise in the External Forces", Fluid Mech. Sov. Res., Vol. 10, No. 3, May - June 1975.

[55] - Sevik, M. and Park, S. H., "The Splitting of Drops and Bubbles by Turbulent Fluid Flow", ASME Journ. Fluids Eng., Mar. 1973.

[56] - MacCormack, R. W., "The Effect of Viscosity in Hypervelocity Impact Cratering", AIAA Paper No. 69-354, 1969.

[57] - McClintock, R. B. and Silvestri, G. J., Calculation of Properties of Steam, American Society of Mechanical Engineers, New York, 1968.

[58] - Yanta, W. J., "Measurements of Aerosol Size Distributions with a Laser Doppler Velocimeter (LDV)", AIAA Paper No. 73-705, July 1973.

[59] - Weiss, H. and Shaw, G., "Geothermal Two-Phase-Flow Test Facility", Proceedings of the Second United Nations Symposium on the Development and Use of Geothermal Resources, Vol. 3, May 1975.

[60] - Crowe, C. T., Two-Phase Boundary Layer Code, Lawrence Livermore Laboratory Internal Memorandum, Livermore, California, Nov. 9, 1977.

[61] - Kerker, M., The Scattering of Light and Other Electromagnetic Radiation, Academic Press, New York, 1969.

[62] - Hodkinson, J. R., "The Optical Measurement of Aerosols", in Aerosol Science, C. N. Davies Ed., Academic Press, New York, 1966.

[63] - Fine Particles: Aerosol Generation, Measurement, Sampling, and Analysis, B. Y. H. Liu Ed., Academic Press, New York, 1976.

[64] - Chin, J. H., Sliepcevich, C. M., and Tribus, M., "Particle Size Distribution from Angular Variation of Intensity of Forward-Scattered Light at Very Small Angles", Journ. Phys. Chem., Vol. 59, No. 9, Sept. 1955.

[65] - Titchmarsh, E. C., "Extensions of Fourier's Integral Formula Involving Bessel Functions", Proc. London Math. Soc., Vol. 23, Series 2, Jan. 1924.

[66] - Chin, J. H., Sliepcevich, C. M., and Tribus, M., "Determination of Particle Size Distributions in Polydisperse Systems by Means of Measurements of Angular Variation of Intensity of Forward Scattered Light at Very Small Angles", Journ. Phys. Chem., Vol. 59, No. 9, Sept. 1955.

[67] - Shifrin, K. S. and Kolmakov, I. B., "Effect of Limitation of the Range of Measurement of the Indicatrix on the Accuracy of the Small-Angle Method", Atm. Oceanic Phys., Vol. 2, No. 8, Aug. 1966.

[68] - Shifrin, K. S., "The Essential Range of Scattering Angles in Measuring Particle-Size Distribution by the Small-Angle Method", Atm. Oceanic Phys., Vol. 2, No. 9, Sept. 1966.

[69] - Shifrin, K. S. and Kolmakov, I. B., "Calculation of Particle Size Spectrum from Direct and Integral Values of the Indicatrix in the Small-Angle Region", Atm. Oceanic Phys., Vol. 3, No. 12, Dec. 1967.

[70] - Swithenbank, J., Beer, J. M., Taylor, D. S., Abbot, D., and McCreath,G. C., "A Laser Diagnostic Technique for the Measurement of Droplet and Particle Size Distribution", AIAA Paper No. 76-69, Jan. 1976.

[71] - Pozharnov, V. A., "Measurement of Droplet Size Spectrum in Two-Phase Flows from Low-Angle Light Scattering", Fluid Mech. Sov. Res., Vol. 4, No. 5, Sept. - Oct. 1975.

[72] - Aref'yev, N. V., Bazin, V. A., and Pokhil'ko, A. F., "A Technique for Determining the Size Distribution of Cavitation Nuclei in Liquid Flows", Fluid Mech. Sov. Res., Vol. 5, No. 3, May - June 1976.

[73] - Kerker, M., Matijevic, E., Epenscheid, W. F., Farone, W. A., and Kitani, S., "Aerosol Studies by Light Scattering. 1. Particle Size Distribution by Polarization-Ratio Method", Journ. Colloid Sci., Vol. 19, No. 3, Mar. 1964.

[74] - Stevensen, A. F., Heller, W., and Wallach, M. L., "Theoretical Investigations of the Light Scattering of Colloidal *Spheres. XI. Determination of Size Distribution from Spectra of the* Scattering Ratio or from Depolarization Spectra", Journ. Chem. Phys., Vol. 34, No. 5, May 1961.

[75] - Heller, W. and Wallach, M. L., "Experimental Investigations of the Light Scattering of Colloidal Spheres. V. Determination of Size Distribution Curves by Means of Spectra of the Scattering Ratio", Journ. Phys. Chem., Vol. 67, No. 12, Dec. 1963.

[76] - Wallach, M. L., Heller, W., and Stevenson, A. F., "Theoretical Investigations of the Light Scattering of Colloidal Spheres. XII. The Determination of the Size Distribution Curves from Turbidity Spectra", Journ. Chem. Phys., Vol. 34, No. 5, May 1961.

[77] - Wallach, M. L. and Heller, W., "Experimental Investigations of the Light Scattering of Colloidal Spheres. VI. Determination of Size Distribution Curves by Means of Turbidity Spectra", Journ. Phys. Chem., Vol. 68, No. 4, April 1964.

[78] - Shifrin, K. S. and Perel'man, A. Y., "The Determination of the Spectrum of Particles in a Dispersed System from Data on its Transparency: I. The Fundamental Equation for Determination of the Spectrum of the Particles", Optics and Spectroscopy, Vol. 15, No. 4, Oct. 1963.

[79] - Phillips, D. L., "A Technique for the Numerical Solution of Certain Integral Equations of the First Kind", Assoc. Comp. Mach., Vol. 9, No. 1, Jan. 1962.

[80] - Hanson, R. J., "A Numerical Method for Solving Fredholm Integral Equations of the First Kind Using Singular Values", SIAM Journ. Num. Anal., Vol. 8, No. 3, Sept. 1971.

[81] - Turchin, V. F. and Nozik, V. Z., "Statistical Regularization of the Solution of Incorrectly Posed Problems", Atm. Oceanic Phys., Vol. 5, No. 1, Jan. 1969.

[82] - Shifrin, K. S., Turchin, V. F., Turovtseva, L. S., and Gashko, V. A., "Reconstruction of Particle Size Distribution by Statistical Regularization of the Scattering Function", Atm. Oceanic Phys., Vol. 8, No. 12, Dec. 1972.

[83] - Powell, M. J. D., "A Method for Minimizing a Sum of Squares of Non-Linear Functions withou. Calculating Derivatives", Computer Journ., Vol. 7, No. 4, Jan. 1965.

[84] - Mugele, R. A. and Evans, H. D., "Droplet Size Distribution in Sprays", Ind. Eng. Chem., Vol. 43, NO. 6, June 1951.

[85] - Dobbins, R. A. and Strand, L. D., "A Comparison of Two Methods of Measuring Particle Size of Al_2O_3 Produced by a Small Rocket Motor", AIAA Journ., Vol. 8, No. 9, Sept. 1970.

[86] - Weaver, J. F., Sommargren, G. E., and Bliss, E. S., "Self-Calibration and Analysis of Image Formation in the Sub-Nanosecond Domain", Proceedings of SPIE 18th Annual Technical Meeting, Aug. 1974.

[87] - Hanson, A. R., Domich, E. G., and Adams, H. S., "Shock Tube Investigation of the Breakup of Drops by Air Blasts", Phys. of Fluids, Vol. 6, No. 8, Aug. 1963.

[88] - Aeschliman, D. P., "An Experimental Study of the Response of Water Droplets to Flows Behind Plane Shock Waves", SC-RR-71-0540, Sandia Laboratories, Albuquerque, New Mexico, Oct. 1971.

[89] - Reichman, J. M., "A Study of the Motion, Deformation, and Breakup of Acceleratinng Water Droplets", Ph. D. Thesis, Rutgers University, New Brunswick, New Jersey, June 1973.

[90] - Stadtke, H., "Theoretical Investigation of Non-Equilibrium Flow of Vaporizing Potassium Through a Convergent-Divergent Nozzle", Progress in Heat and Mass Transfer, Vol. 7: Heat Transfer in Liquid Metals, O. E. Dwyer Ed., Pergamon Press, New York, 1973.

[91] - Dobbins, R. A. and Jizmagian, G. S., "Optical Scattering Cross-Sections for Polydispersions of Dielectric Spheres", J. Opt. Soc. Am., Vol. 56, No. 10, Oct. 1966.

[92] - Walters, P. T., "Optical Measurement of Water Droplets in Wet Steam Flows", Instn. Mech. Engrs., Paper C32/73, Conf. Pub. 3, Apr. 1973.

[93] - Durbin, E. J., "Optical Methods Involving Light Scattering for Measuring Size and Concentration of Condensation Particles in Supercooled Hypersonic Flow", NACA-TN-2441, Aug. 1951.

[94] - Carlon, H. R., Milham, M. E., and Frickel, R. H., "Determination of Aerosol Droplet Size and Concentration from Simple Transmission Measurements", Applied Optics, Vol. 15, No. 10, Oct. 1976.

[95] - Walstra, P., "Discussion of Errors in Turbidimetry", Brit. J. Appl. Phys., Vol. 16, No 8, Aug. 1965.

[96] - Spankuch, D., "Information Content of Extinction and Scattered-Light Measurements for the Determination of the Size Distribution of Scattering Particles", Applied Optics, Vol. 11, No. 12, Dec. 1972.

[97] - Fenton, D. L. and Stukel, J. J., "Measurement of the Local Particle Concentration in Fully Developed Turbulent Dust Flow", Int. J. Multiphase Flow, Vol. 3, No. 2, Dec. 1976.

[98] - Gumprecht, R. O. and Sliepcevich, C. M., "Scattering of Light by Large Spherical Particles", J. Phys. Chem., Vol. 57, No.1, Jan. 1953.

[99] - Trolinger, J. D., "Laser Instrumentation for Flow Field Diagnostics", NATO Advisory Group for Aerospace Research and Development, AGARD-AG-186, Mar. 1974.

[100] - Pchelkin, I. M., Kalakutskaya, N. A., and Parfent'yeva, I. F., "Local Characteristics of Two-Phase Flows at Nozzle Discharges", Fluid Mech. Sov. Res., Vol. 4, No. 4, July - Aug. 1975.

[101] - Watrasiewicz, B. M. and Rudd, M. J., Laser Doppler Measurements, Butterworths, London, 1976.

[102] - Durst, F., Melling, A., and Whitelaw, J. H., Principles and Practice of Laser-Doppler Anemometry, Academic Press, New York, 1976.

[103] - Hercher, M., "The Spherical Mirror Fabry-Perot Interferometer", Applied Optics, Vol. 7, No. 5, May 1968.

[104] - Jackson, D. A. and Paul,D. M., "Measurement of Hypersonic Velocities and Turbulence by Direct Spectral Analysis of Doppler Shifted Laser Light", Phys. Letters, Vol. 32A, No. 2, June 1970.

[105] - Jackson, D. A. and Paul, D. M., "Measurement of Supersonic Velocity and Turbulence by Laser Anemometry", Journ. Phys. E: Scientific Instruments, Vol. 4, Mar. 1971.

[106] - Paul, D. M. and Jackson, D. A., "Rapid Velocity Sensor Using a Static Confocal Fabry-Perot and a Single Frequency Argon Laser", Journ. Phys. E: Scientific Instruments, Vol. 4, Mar. 1971.

[107] - Eggins, P. L., Jackson, D. A., and Paul, D. M., "Measurement of Mean Velocity and Turbulence in Supersonic Boundary Layers, Shock Waves and Free Jets by Laser Anemometry", Opto-electronics, Vol. 5, No. 1, Jan. 1973.

[108] - Avidor, J. M., "Novel Instantaneous Laser Dopplet Velocimeter", Applied Optics, Vol. 13, No. 2, Feb. 1974.

[109] - James, R. N., Babcock, W. R., and Seifert, H. S.,"A Laser-Doppler Technique for the Measurement of Particle Velocity", AIAA Journ.,Vol. 6, No. 1, Jan. 1968.

[110] - Self, S. A., "Laser Doppler Anemometer for Boundary Layer Measurements in High Velocity, High Temperature MHD Channel Flows", Proc. of the Second International Workshop on Laser Velocimetry, Vol. 2, Mar. 1974.

[111] - Daily, J. W., Kruger, C. H , Self, S. A., and Eustis, R. H., "Boundary-Layer Profile Measurements in a Combustion Driven MHD Generator", AIAA Journ., Vol. 14, No. 8, Aug. 1976.

[112] - Self, S. A. and Kruger, C. H., "Diagnostic Methods in Combustion MHD Flows", Journ. of Energy, Vol. 1, No. 1, Jan. - Feb. 1977.

[113] - Jackson, D. A. and Paul, D. M., "Assessment of the argon laser as a suitable source for low-frequency heterodyne anemometry experiments", Journ. Phys. E: Scientific Instruments, Vol. 2, Series 2, Dec. 1969.

[114] - Hercher, M., "Tunable Single Mode Operation of Gas Lasers Using Intracavity Tilted Etalons", Applied Optics, Vol. 8, No. 6, June 1969.

APPENDIX A

MIE THEORY LIGHT SCATTERING RELATIONS

The theoretical relationship for the angular distribution of the intensity of light scattered by a single spherical particle of arbitrary size was developed by Mie [45]. This result was presented in equation (27), with the exception of the definition of the Mie scattering function, $i(\theta,\alpha,m)$. The numerical value of the Mie scattering function depends upon the scattering angle, θ, the incident light wavelength, λ, the particle diameter, D, the particle index of refraction relative to that of the surrounding medium, m, and the incident light polarization. The Mie scattering function for vertically polarized light can be expressed as [49]

$$i(\theta,\alpha,m)_{VP} = i_1 = |G_1(\theta)|^2 \tag{A.1}$$

where

$$G_1(\theta) = \sum_{n=1}^{\infty} \frac{(2n+1)}{n(n+1)} [a_n \pi_n(\cos\theta) + b_n \tau_n(\cos\theta)] \tag{A.2}$$

Similarly, the Mie scattering function for horizontally polarized light can be written as

$$i(\theta,\alpha,m)_{HP} = i_2 = |G_2(\theta)|^2 \tag{A.3}$$

where

$$G_2(\theta) = \sum_{n=1}^{\infty} \frac{(2n+1)}{n(n+1)} [b_n \pi_n(\cos\theta) + a_n \tau_n(\cos\theta)] \qquad (A.4)$$

For incident natural light, the Mie scattering function can be expressed as a combination of the vertical and horizontal polarization scattering functions by the equation

$$i(\theta,\alpha,m)_{NL} = (i_1 + i_2)/2 \qquad (A.5)$$

In these equations, a_n and b_n are the scattering coefficients (functions of α and m only) and can be written as

$$a_n = \frac{S_n'(\alpha m)S_n(\alpha) - mS_n'(\alpha)S_n(\alpha m)}{S_n'(\alpha m)\varphi_n(\alpha) - m\varphi_n'(\alpha)S_n(\alpha m)} \qquad (A.6)$$

and

$$b_n = \frac{mS_n'(\alpha m)S_n(\alpha) - S_n'(\alpha)S_n(\alpha m)}{mS_n'(\alpha m)\varphi_n(\alpha) - \varphi_n'(\alpha)S_n(\alpha m)} \qquad (A.7)$$

where

$$S_n(z) = \left(\frac{\pi z}{2}\right)^{1/2} J_{n+1/2}(z) \qquad (A.8)$$

$$C_n(z) = (-1)^n \left(\frac{\pi z}{2}\right)^{1/2} J_{-(n+1/2)}(z) \qquad (A.9)$$

and

$$\varphi_n(z) = S_n(z) + i\, C_n(z) \qquad (A.10)$$

In equations (A.8) - (A.10), the arguement, z, can assume the value of either α or αm. The primes denote a partial derivative with respect to the arguement, $i = (-1)^{1/2}$ and J is the half order ordinary Bessel

function. The angular functions $\pi_n(\cos\theta)$ and $\tau_n(\cos\theta)$ are Legendre polynomial functions, given by

$$\pi_n(\cos\theta) = \frac{P_n^1(\cos\theta)}{\sin\theta} \tag{A.11}$$

and

$$\tau_n(\cos\theta) = \frac{d}{d\theta}[P_n^1(\cos\theta)] \tag{A.12}$$

where the function $P_n^1(\cos\theta)$ is a Legendre polynomial in terms of $\cos\theta$.

An additional important result of the Mie scattering equations is the formulation of the scattering efficiency factor, Q_{ext}. The scattering efficiency factor is expressed using equations (A.2) and (A.4) applied at $\theta = 0$ degrees, to obtain $(G_1(0) = G_2(0) = G(0))$ [49]

$$Q_{ext} = \frac{4}{\alpha^2} \mathrm{Re}\{G(0)\} \tag{A.13}$$

where the amplitude function G(0) is given by

$$G(0) = \frac{1}{2} \sum_{n=1}^{\infty} (2n + 1)(a_n + b_n) \tag{A.14}$$

Thus, the scattering efficiency factor becomes

$$Q_{ext} = \frac{2}{\alpha^2} \sum_{n=1}^{\infty} (2n + 1)\ \mathrm{Re}(a_n + b_n) \tag{A.15}$$

With this system of equations, the amplitude functions, $G_1(\theta)$ and $G_2(\theta)$, can be calculated to yield the required Mie scattering function, $i(\theta,\alpha,m)$, for the droplet size distribution inversions, and the scattering efficiency factor, Q_{ext}, can be calculated for the light transmission measurements. These equations were solved for this study

using the general scheme developed by Gucker and Cohn [A1] and presented in detail by Erickson [A2]. The Legendre functions were determined using a modification of the computer formulation presented by Hancock and Livingston [A3]. Since the calculations were made using a CDC-7600 (60 bit word size), double precision arithmetic was found to be unnecessary, even for very large particle sizes. Convergence of the infinite series was assumed to be satisfactory when the normalized difference between the partial sums was less than a specified tolerance (typically 10^{-4} to 10^{-6}). Numerical values for the calculated Mie scattering functions, i_1 and i_2, were compared with those presented by several authors (see references [98] and [A1] - [A4]) to verify the computer subprogram before proceeding with the work presented in this report.

References for Appendix A

[A1] - Gucker F. T. and Cohn, S. H., "Numerical Evaluation of the Mie Scattering Functions; Table of Angular Functions π_n and τ_n of Order 1 to 32, at 2.5° Intervals", Journ. Colloid. Sci., Vol. 8, No. 6, Dec. 1953.

[A2] - Erickson, W. D., "Light Scattering; A Technique for Studying Soot in Flames", Sc. D. Thesis, Massachusetts Institute of Technology, Cambridge, Mass., Dec. 1961.

[A3] - Hancock, J. H. and Livingston, P. M., "Program for Calculating Mie Scattering for Spheres, Using Kerker's Formulation, Over a Specified Particle-Size Distribution", NRL Report 7808, Naval Research Laboratory, Washington, D. C., Nov. 1974.

[A4] - Kerker, M. and Matijevic, E., "Mie Scattering Functions for Refractive Index of 2.105", Journ. Opt. Soc. Am., Vol. 51, No. 1, Jan. 1961.

APPENDIX B

DIFFRACTION THEORY LIGHT SCATTERING RELATIONS

When considering the light scattered by a polydispersion of particles that are large when compared to the incident light wavelength ($\alpha > 20$), the exact Mie theory scattering function, $i(\theta,\alpha,m)$, can be approximated by the much simpler diffraction theory scattering function, $i_d(\theta,\alpha)$. This function was presented by equation (32) for small angle scattering ($\theta \approx \sin\theta$). Substitution of this function into equation (31) yields the scattered light intensity as

$$J(\theta) = K \int_0^\infty \left[\frac{\alpha J_1(\alpha\theta)}{\theta}\right]^2 f(\alpha)d\alpha \qquad (B.1)$$

The importance of using this equation only for large particle dispersions is shown by Figure B1. In this figure, comparisons of the relative scattered light intensity profiles calculated using both Mie theory (equation (31) for horizontal polarization) and diffraction theory (equation (B.1)) are presented for two different size distribution functions. The larger particle size distribution function was formed using a ULDF with $\bar{\alpha} = 50.0$, $Q_{ULDF} = 0.75$ and $\alpha_\infty = 80.0$, and the smaller particle size distribution function was formed using a ULDF with $\bar{\alpha} = 10.0$, $Q_{ULDF} = 0.75$ and $\alpha_\infty = 20.0$. It can be seen that much better agreement between the Mie theory calculations and the diffraction theory calculations is obtained for the larger particle size distribution function. This agreement becomes better as the particle size is increased.

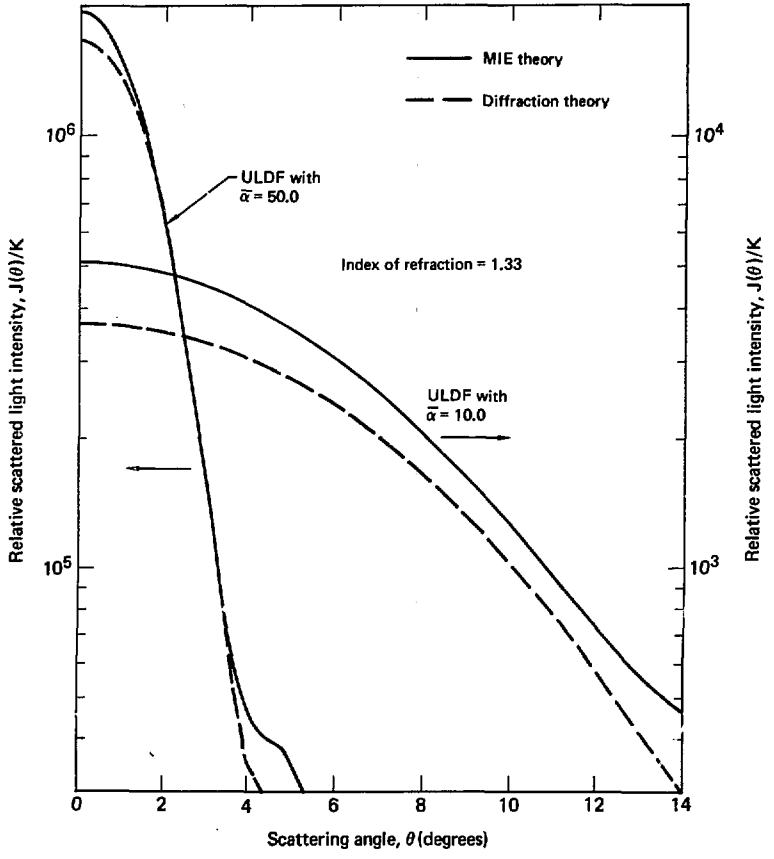

Figure B1. – A comparison of relative scattered light intensity profiles calculated using both Mie theory and diffraction theory for two different particle size distributions.

Equation (B.1) can be analytically inverted to yield an explicit relationship between the particle size distribution function, $f(\alpha)$, and the scattered light intensity variation, $J(\theta)$, as (see equation (33)) [64], [65]

$$f(\alpha) = -2\pi\left(\frac{2\pi}{\lambda}\right)^2 \int_0^\infty \frac{dg(\theta)}{d\theta}\left(\frac{\theta}{\alpha}\right) J_1(\alpha\theta) Y_1(\alpha\theta) d\theta \qquad (B.2)$$

where

$$g(\theta) = \left[\frac{\theta^3 J(\theta)}{I_o}\right] \qquad (B.3)$$

The use of equation (B.2) to determine the size distribution function for a large particle polydispersion requires a differentiation of the experimental scattered light intensity profile†. This requires precise experimental data and extreme care in the differentiation process to yield accurate size distribution function inversions. Figure B2 presents the variation of this derivative term, $(2\pi/\lambda)^2 dg(\theta)/d\theta$, as a function of the scattering angle for the relative scattered light intensity profiles of Figure B1. Comparisons between the Mie theory and the diffraction theory results indicate much better agreement is again obtained for the larger particle polydispersion.

To avoid the problems inherant in the differentiation of experimental data, Shifrin and Kolmakov [69] expanded equation (B.2) to an equation involving only an integration of the experimental data.

† – Equation (B.2) was used directly to determine the glass beads-in-water particle size distributions presented in Figure 37. It was found that a graphical differentiation, combined with minor smoothing of the differentiated scattered light intensity data, yielded accurate large particle size distribution function inversions.

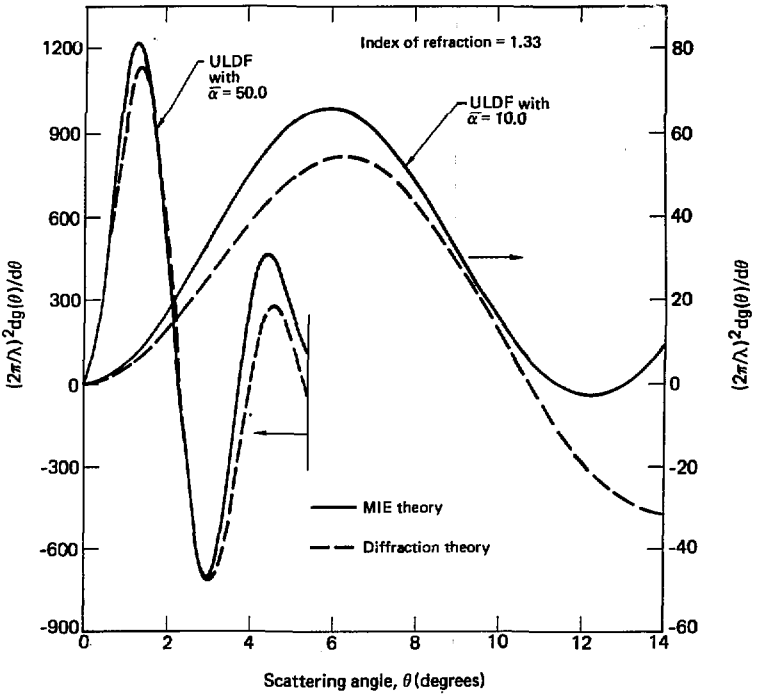

Figure B2. – A comparison of the derivative term, $(2\pi/\lambda)^2 dg(\theta)/d\theta$, of equation (B.2) calculated for the relative scattered light intensity profiles of Figure B1.

This development proceeded by substituting equation (B.1) into equation (B.3) to obtain $g(\theta)$ as

$$g(\theta) = \left(\frac{\lambda}{2\pi}\right)^2 \int_0^\infty \alpha f(\alpha)[(\alpha\theta)J_1^2(\alpha\theta)]d\theta \tag{B.4}$$

A new variable, $T(\theta)$, was defined as

$$T(\theta) = g(\theta) - g(\infty) \tag{B.5}$$

such that in the limit as $\theta \to \infty$, $g(\infty)$ becomes the constant

$$g(\infty) = \left(\frac{\lambda}{2\pi}\right)^2 \int_0^\infty \left[\frac{\alpha f(\alpha)}{\pi}\right]d\theta \tag{B.6}$$

By defining

$$M(\theta) = \int_0^\theta T(\tau)d\tau \tag{B.7}$$

Integrating equation (B.2) by parts twice and incorporating equations (B.3) - (B.7), yields the particle size distribution function as

$$f(\alpha) = -2\pi\left(\frac{2\pi}{\lambda}\right)^2 \int_0^\infty M(\theta)\frac{d^2}{d\theta^2}[(\theta/\alpha)J_1(\alpha\theta)Y_1(\alpha\theta)]d\theta \tag{B.8}$$

From an inspection of the preceeding development, it can be seen that the particle size distribution function can be determined for a large particle polydispersion from the experimental measurement of $g(\theta)$ and the use of equations (B.5), (B.7) and (B.8). Equation (B.5) involves the determination of $g(\infty)$ at large angles where $g(\theta)$ is essentially constant (see equation (B.6)). The determination of this constant is critical, and its requirement severely limits the smallest particle sizes that can be measured.

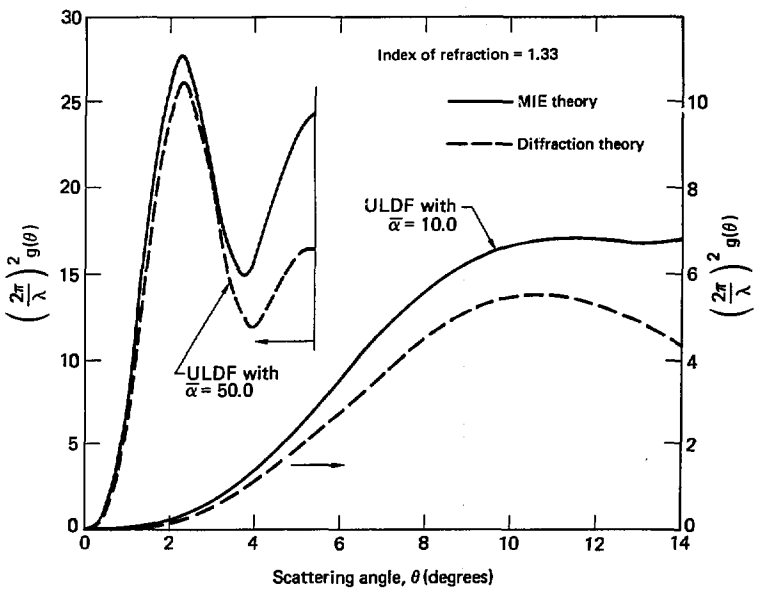

Figure B3. – A comparison of the term, $(2\pi/\lambda)^2 g(\theta)$, of equation (B.2) calculated for the relative scattered light intensity profiles of Figure B1.

Figure B3 presents the quantity, $(2\pi/\lambda)^2 g(\theta)$, as a function of the scattering half angle for the scattered light intensity profiles presented in Figure B1. This is the same function that was differentiated to obtain the information shown in Figure B2. It can be seen from this figure that because of the oscillations in $g(\theta)$, the experimental determination of $g(\infty)$ requires relatively large angle measurements. Also, because of the deviation between the exact Mie theory calculations and the approximate diffraction theory calculations, it appears that the accurate determination of $g(\infty)$ will require that only very large particle size distribution functions can be inverted accurately with this integral formulation.

APPENDIX C

FILM CALIBRATION AND DATA ANALYSIS PROCEDURE

Film Calibration and Scattered Light Data Recording

The recording of the film calibration and scattered light intensity data, shown schematically in Figure 34, occurred in two separate and distinct steps. First, the optical system was aligned to bypass the film calibration mirror pair. In this arrangement, the data corresponding to the different scattered light intensity profiles were recorded on individual pieces of film. Then, following this sequence of photographs, the optical system was realigned to bypass the light scattering optics, and each piece of film was exposed to the light beams from the calibration mirror pair.

The calibration mirror pair was designed to provide a series of exposures with a differing, but known relative energy density associated with each beam. A schematic of the partially transmitting film calibration mirror pair is shown in Figure C1. It can be seen that for an initial light beam energy density, E_0, incident upon the left side of the mirror pair, the first transmitted beam output on the right side of the mirrors has an energy density equal to $(1 - R_1)(1 - R_2)E_0$. Designating this quantity as E_1 yields the energy density of each of the succeeding transmitted beams on the right side of the mirror pair equal to the quantity $(R_1R_2)^{n-1}E_1$, where n is the light beam number. A similar relationship can be seen to exist for the reflected light beams

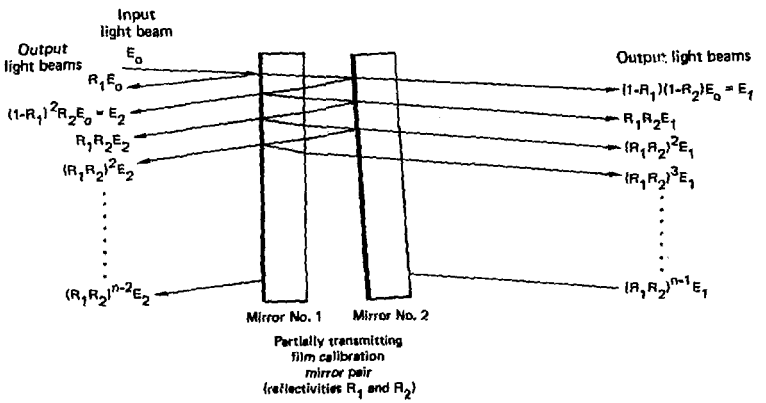

Figure C1. - Schematic of the tilted calibration mirror pair showing the light transmission and reflection interaction that results in the multiple calibration light beams.

leaving the left side of the mirror pair, provided that the first reflected light beam is not included. For this work, the mirror reflectivities were specified to be near 70% (they were measured at 0.701 and 0.728 at λ = 632.8 nm) so that the relative energy density change, R_1R_2, would be near 50%.

An exposure of the film to this series of light beams, in conjunction with a microdensitometric scan of the film, provides a relationship between the incident light energy density and the resulting film density. Each individual piece of film was calibrated in this manner to assure high accuracy. This was necessary because of possible variations in the film development process, or due to variations in the film emulsion. This film calibration method can be extended to provide an absolute calibration by including a calorimetric measurement of the energy density in the initial light beam.

Film Density Digitization Procedure

The calibration exposure and scattered light film density information that was recorded on each piece of film was digitized using a computer controlled microdensitometer. The microdensitometer was used to scan the film to provide a high accuracy measurement of the film density and its spatial location on the film. For this work, a microdensitometer slit size of 57 X 57 μm was used in conjunction with a spatial step size between 50 and 200 μm. The step size was dependent upon the size of the exposure to be scanned and limited only by the

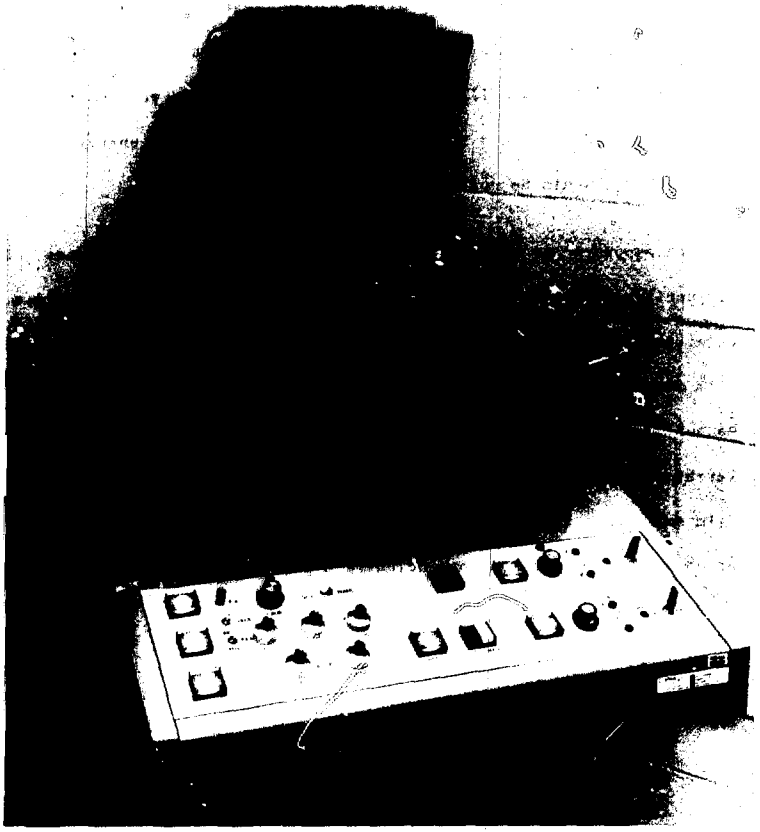

Figure C2. – Photograph of the scanning microdensitometer.

Figure C3. - Photograph of the microdensitometer computer control and magnetic tape recorder system.

maximum array size allowed by the data analysis computer program. The digitized film density data was stored on a magnetic tape prior to its transfer to a disc file on the main computer system (CDC-7600's). Photographs of the microdensitometer and its associated computer controls and tape recording system are shown in Figures C2 and C3, respectively.

Film Density to Energy Density Conversion

Since the light scattering droplet size distribution measurement technique requires a determination of the scattered light intensity profile†, the digitized film density information contained in the computer disc file must be converted to this form. This conversion process was accomplished through the use of the computer program developed by Weaver, et. al. [86]. The computer calculations involve an analysis of the film density information from a line scan directly through the center of each of the calibration exposures. The film density of each of these exposures that is used in the film calibration analysis is determined at the spatial coordinate corresponding to the center of the full width at the half maximum density point. A plot of a typical calibration exposure line scan is shown in Figure C4. The vertical lines near the peak of each exposure corresponds to the film density chosen for the subsequent film calibration analysis.

† - A relationship between the film energy density and the scattered light intensity is derived in Appendix D. It is shown that the two are identical, except for a constant multiplier.

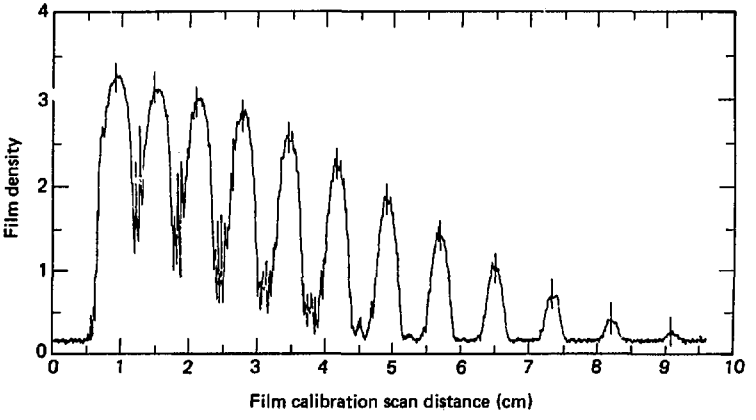

Figure C4. - Plot of a typical microdensitometric calibration exposure scan.

By combining the film density information for each of the calibration exposures with the known relative energy density of the corresponding light beams (due to the $(R_1R_2)^{n-1}E_1$ relationship), a relationship between the film density and its associated energy density can be determined. Figure C5 presents such a relationship for the calibration exposures of Figure C4. The X's represent the peak film density points shown in Figure C4, and the solid line is a polynomial curve fit to these data points. This curve fit is used to provide the continuous film density - energy density relationship required to convert the scattered light film density to energy density for use in the droplet size distribution inversion procedure.

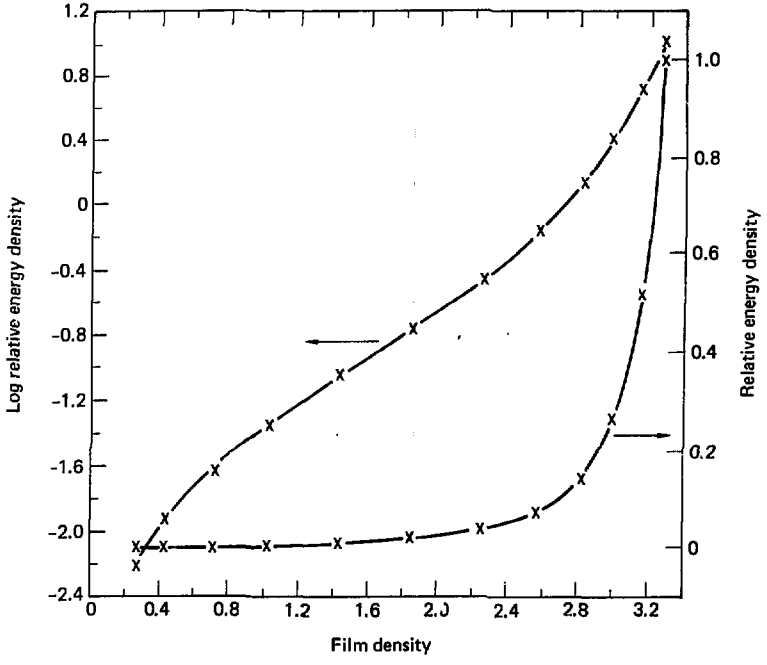

Figure C5. - Film density versus energy density relationship for the calibration exposure scan of Figure C4.

APPENDIX D

SCATTERED LIGHT RECEIVING LENS DESIGN AND INTENSITY ANALYSIS

Ideal Thin Lens Design

The determination of the droplet size distribution by light scattering requires an optical arrangement that can distinguish the angular variation of the scattered light intensity. One such optical arrangement, developed by Chin, et. al. [64] for scattered light intensity measurements, is shown in Figure D1. From the thin lens relationship, it can be written that

$$\frac{1}{s} + \frac{1}{s'} = \frac{1}{F_l} \tag{D.1}$$

where F_l is the focal length of the lens, s is the object distance of the scattering particle and s' is the image distance. From similar triangles, it can be written that

$$\frac{r}{s' - F_l} = \frac{H}{s'} \tag{D.2}$$

where r is the radius to the scattered light intersection point at the focal plane, and H is the radius to the scattered light intersection with the receiving lens. Combining equations (D.1) and (D.2) yields

$$\frac{1}{s} = \frac{1}{F_l} - \frac{1}{s'} = \frac{s' - F_l}{s'F_l} = \frac{r}{HF_l} \tag{D.3}$$

Rearranging equation (D.3) and assuming small scattering angles results

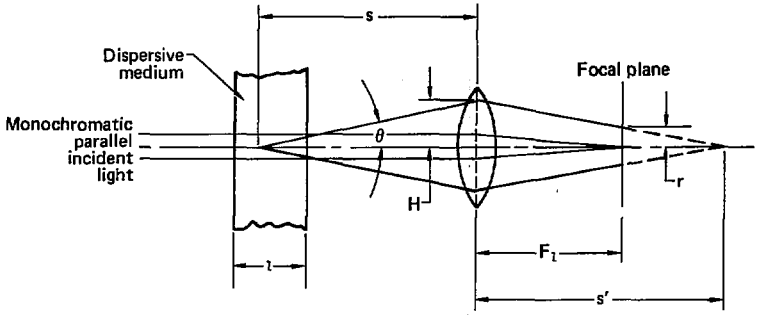

Figure D1. – Scattered light collecting lens geometry.

with

$$\frac{H}{s} = \frac{r}{F_l} = \tan \theta \approx \theta \qquad (D.4)$$

Thus, it can be seen that for single particle scattering, the scattering half angle, θ, is independent of the position of the particle in the light beam, and it is characterized by the radius at the focal plane and the lens focal length.

Real Lens Design

It can be shown from ray tracing calculations that equation (D.4) is very accurate for determining the scattering half angle, θ, as long as the lens focal length is large and the scattering half angle is small. The reason that scattering angle measurement errors occur when these conditions are not satisfied is because of a defocusing phenomena known as lens spherical aberrations.

Jenkins and White [D1] present a third order thin lens equation that shows that the magnitude of the focal length deviation due to spherical aberrations is proportional to the square of the lens radius at the scattered light intersection point divided by the lens focal length (S.A. $\propto H^2/F_l^3$). Thus, by minimizing this quantity for a given light scattering arrangement, the scattering half angle measurement error can also be minimized. It should also be noted that finite measurement volume sizes can introduce spherical aberration errors because of the different lens intersection radii that can occur for

scattered light rays with identical scattering angles but different spatial origins. For this reason, it is especially advantageous to use minimum thickness dispersions whenever possible.

The receiving lens pair used for this study was designed to allow the large scattering half angle measurements (14 degrees maximum) necessary to obtain the small droplet size information, while essentially eliminating errors due to lens spherical aberrations. To minimize the spherical aberrations, two 60 cm focal length plano-convex lenses (apertured at a 5.1 cm diameter) were aligned in series to form the receiving optics. This lens pair was then located a distance of 10 cm from the nozzle jet†. The combination of these two changes minimized the quantity H^2/F_i^3 and the subsequent spherical aberration errors for the light scattering measurements of the droplet size distribution in the nozzle jet flow. Also, the scattering volume was limited to the He-Ne laser beam diameter and the nozzle jet thickness of 0.325 cm to minimize errors due to the measurement volume size. This optical geometry was checked using ray tracing calculations and found to yield a minimum scattering half angle resolution (scattered light overlap at the film plane for the maximum scattering angle of 14 degrees) of better than 0.01 degree.

† - This location provided the shortest possible distance between the lens pair and the nozzle jet.

Film Plane Alignment

The film plane was aligned with the lens pair in a manner that was simple, but yet it afforded an alignment accuracy of better than 0.1 cm in 30.0 cm. The alignment was accomplished by passing two parallel laser beams (separated by approximately 1.1 cm) through the lens on a diameter with each beam at an equal distance from the lens center. The two beams were subsequently focused to an intersection point at the focal length of the lens pair. The film plane was then precisely located at this beam intersection point using the film positioning arrangement shown in Figure 36.

Calibrated Film Energy Density - Scattered Light Intensity Relationship

The scattered light information that was recorded on the calibrated film was converted to relative energy density as a function of the scattering half angle through the use of the film calibration and optical arrangement information. However, the light scattering integral equation (equation (31)) inversion requires a measurement of the scattered light intensity, $J(\theta)$. To determine the relationship between the recorded energy density and the scattered light intensity, the light scattering integral equation

$$J(\theta) = K \int_0^\infty i(\theta,\alpha,m) f(\alpha) d\alpha \qquad (31)$$

must be considered. The units of $J(\theta)$ are power (watts) per unit solid

angle. Thus, the amount of power scattered in an angle γ in the forward direction is given by

$$P(\gamma) = \int_{\omega} J(\theta)d\omega = 2\pi \int_{0}^{\gamma} J(\theta)(\sin\theta)d\theta \qquad (D.5)$$

where ω is the included solid angle. Similarly, an integration of the energy density measured at the film plane over a radius, R, corresponding to the included scattering angle, γ, yields

$$P(\gamma) = \frac{2\pi}{t} \int_{0}^{R} E(\theta)rdr \qquad (D.6)$$

where t is the exposure time, and r is the radius from the image center on the film. Now, writing equation (D.4) in a form to include the multiplier $h(\theta)$ to account for possible deviation from ideal thin lens theory (*e. g., spherical aberrations*) *yields*

$$\frac{r}{F_i} = h(\theta)\tan\theta \qquad (D.7)$$

such that

$$rdr = F_i^2 h(\theta)[h(\theta)/\cos^2\theta + h'(\theta)\tan\theta](\tan\theta)d\theta \qquad (D.8)$$

where the prime denotes a derivative with respect to the angle θ. Substitution of equation (D.8) into equation (D.6) results with

$$P(\gamma) = \frac{2\pi F_i^2}{t} \int_{0}^{\gamma} E(\theta)\{h(\theta)[h(\theta)/\cos^2\theta + h'(\theta)\tan\theta]\}(\tan\theta)d\theta \qquad (D.9)$$

Now, by a direct comparison of equations (D.5) and (D.9), it can be seen that

$$J(\theta) = \frac{F_l^2 E(\theta)}{t(\cos\ \theta)}\{h(\theta)[h(\theta)/\cos^2\theta + h'(\theta)\tan\ \theta]\} \qquad (D.10)$$

In the ideal thin lens approximation and for small scattering angles, $h(\theta) = 1.0$, $\sin\ \theta \approx \tan\ \theta \approx \theta$ and $\cos\ \theta \approx 1.0$, so that equation (D.10) reduces to the simple relation

$$J(\theta) = \frac{F_l^2 E(\theta)}{t} \qquad (D.11)$$

Thus, equation (D.11) clearly demonstrates that the scattered light intensity, $J(\theta)$, is directly proportional to the energy density measured at the film plane, provided that $h(\theta)$ is essentially constant and only small angles are considered†.

The deviation function, $h(\theta)$, and its derivative, $h'(\theta)$, can be determined (see equation (D.7)) for any receiving optics arrangement using ray tracing calculations to assess the differences between the results of equations (D.10) and (D.11). This was accomplished for the receiving lens pair used for this study, with the result being that $h(\theta)$ could be assumed to be a constant over the 0 – 14 degree scattering angle range. This assumption introduced a maximum error of 2% when using equation (D.11) exclusively. Because of this small difference and because the absolute number of particles traversed by the light beam was not needed, this work utilized the measured relative energy density, $E(\theta)$, directly rather than converting to scattered light intensity, $J(\theta)$, for the droplet size distribution inversions.

† – A maximum error of 3% is introduced by using equation (D.11), rather than equation (D.10), at a scattering angle of 14 degrees.

Reference for Appendix D

[D1] - Jenkins, F. A. and White, H. E., Fundamentals of Optics, Fourth Edition, McGraw Hill Book Co., New York, 1976.

U.S.GPO:1978-789-086/4997